Modelling bed-load sediment transport through a granular approach in SPH

Alex Ghaïtanellis

UNIVERSITÉ PARIS-EST

École Doctorale SIE

Laboratoire d'Hydraulique Saint-Venant

Thèse

Présentée pour l'obtention du grade de DOCTEUR
DE L'UNIVERSITE PARIS-EST
par

Alex Ghaïtanellis

Modélisation du charriage sédimentaire par une approche granulaire avec SPH

Spécialité : Mécanique des Fluides

Soutenue le 26 Octobre 2017 devant un jury composé de :

Rapporteur	**Prof. Aronne Armanini**	(University of Trento, Italy)
Rapporteur	**Prof. David Le Touzé**	(Centrale de Nantes, France)
Examinateur	**Prof. Benjamin Dewals**	(Université de Liège, Belgique)
Examinateur	**Prof. Stéphane Abadie**	(Université de Pau, France)
Examinateur	**Dr. Andrea Amicarelli**	(RSE, Italy)
Directeur de thèse	**Dr. Damien Violeau**	(EDF R&D & LHSV, France)
Invité	**Dr. Kamal El Kadi Abderrezzak**	(EDF R&D & LHSV, France)
Invité	**Dr. Pablo Tassi**	(EDF R&D & LHSV, France)

Thèse effectuée au sein du **Laboratoire d'Hydraulique Saint-Venant**

de l'Université Paris-Est

6, quai Watier

BP 49

78401 Chatou cedex

France

Financements : ANR (bourse CIFRE # 2014/0273) et EDF R&D

Résumé

Cette thèse a pour objet le développement d'un modèle de transport sédimentaire avec la méthode SPH (*Smoothed Particle Hydrodynamics*). Si les modèles couramment proposés dans la littérature reposent sur un solveur hydrodynamique couplé à des lois semi-empiriques pour la prise en compte du transport sédimentaire, une approche différente est proposée ici. Le modèle développé dans ce travail inclut la résolution de la dynamique du sédiment. Celui-ci est assimilé à un milieu continu dont la loi de comportement rend compte de la nature granulaire. Pour ce faire, le modèle élastique-viscoplastique d'Ulrich [114] est implémenté dans un code SPH pré-existant programmé en langage Cuda, et amélioré du point de vue physico-numérique. Le comportement mécanique du sédiment dépend alors d'une contrainte de rupture déterminée conformément au critère de Drucker-Prager. Dans les zones du matériau où la rupture n'a pas eu lieu, les contraintes de cisaillement sont calculées selon la loi de Hooke généralisée. Dans les zones où la contrainte de rupture est dépassée, le matériau est assimilé à un fluide rhéofluidifiant. Numériquement, la transition entre les deux états est opérée à l'aide d'une fonction de raccord qui dépend notamment de l'amplitude du taux de déformation et des propriétés granulaires du sédiment. L'eau et le sédiment sont modélisées comme deux phases immiscibles, dans le cadre d'une formulation SPH multiphasique. Pour ce faire, le modèle de Hu et Adams [58] a été adapté aux modèles de conditions limites semi-analytiques [37]. Enfin, un schéma d'intégration implicite des forces visqueuses a été développé dans ce contexte, afin d'améliorer les performances du solveur lors de modélisation d'écoulement à bas Reynolds.

Plusieurs cas tests sont proposés pour valider le modèle multiphasique, le schéma implicite et le modèle élastique-viscoplastique. De manière générale, les résultats sont en bon accord avec les données expérimentales et analytiques. Le modèle permet de représenter des écoulements multiphasiques avec une bonne précision, même en présence d'un grand rapport de densité entre les phases. Il en va de même pour les écoulements de fluide non-newtonien et les écoulements à bas Reynolds, pour lesquels le schéma implicite conduit à des résultats très satisfaisants, et à une amélioration significative des performances du code. Enfin, le modèle élastique-viscoplastique est appliqué à divers cas d'écoulements granulaires, dans le cas d'un matériau sec et saturé, ainsi qu'à des cas d'érosion et d'affouillement. Là encore, les résultats sont globalement en bon accord avec l'expérience.

Mots-clé:

Transport sédimentaire, matériaux granulaires, fluides non-newtoniens, SPH.

Modelling bed-load sediment transport through a granular approach in SPH

Abstract

This thesis presents the development and application of a Smoothed Particle Hydrodynamics (SPH) model to bed-load transport. While state of the art simulation methods commonly rely on a fluid dynamics solver coupled to semi-empirical relationships to model the sediment transport, a completely different approach is investigated in this work. The sediment is treated as a continuum whose behaviour law takes account for its granular nature. Ulrich's [114] elastic-viscoplastic model is thus implemented in an in-house code based on the Cuda language, and improved on physical and numerical aspects. The sediment behaviour depends on a yield stress determined according to Drucker-Prager's criterion. In unyielded regions, the shear stresses are calculated in line with the linear elastic theory. In yielded regions, a shear thinning rheological law is used and the transitions between solid and liquid states are ensured by a blending function driven by the strain rate magnitude and sediment granular properties. Water and sediment are modelled as two immiscible phases in the frame of a multi-phase SPH model with semi-analytical wall boundary conditions [37]. An implicit viscous forces integration scheme is also developed to improve the code performance as for low-Reynolds flows.

The multi-phase model, as well as the implicit viscous forces integration scheme, were validated on analytical test cases and good agreement was obtained. The multi-phase formulation has also proven its capability to handle flows involving high density ratio, while the implicit viscous forces integration scheme was successfully applied to the simulation of a non-Newtonian flow. The elastic-viscoplastic model was tested on dry and submerged granular flow problems. The model was able to correctly capture the liquid and solid states of the granular material, as well as the failure and the regime transitions. It was also applied to bed-load transport problems for which a good agreement with the experiment was generally found.

Keywords:

Sediment transport, granular materials, non-Newtonian fluids, SPH.

Remerciements

Je tiens d'abord à remercier mon directeur de thèse, Damien Violeau, pour la qualité de son encadrement. Si la réussite d'une thèse dépend grandement du sujet, l'encadrement est plus important encore. Avec Damien, j'ai pu travailler de façon autonome, prendre le temps d'étudier des sujets connexes au mien, tout en gardant un cap bien défini. Merci pour ton soutien tout au long de cette aventure, pour ton support scientifique, ta pédagogie, et pour tes relectures attentives dont la rapidité d'exécution te vaudrait sans conteste le titre de *Lucky Luke des relecteurs*.

Merci à Agnès Leroy, Martin Ferrand et Antoine Joly pour leurs idées brillantes (dont, en tant que thésard, je me suis bien sûr approprié le mérite), leur patience et leur aide au quotidien. J'ai pris beaucoup de plaisir à travailler avec vous.

Je remercie Aronne Armanini, David Le Touzé, Benjamin Dewals, Stéphane Abadie et Andrea Amicarelli d'avoir accepté de faire partie de mon jury de thèse. Merci pour l'intérêt que vous avez bien voulu porter à mon travail, et pour vos critiques, remarques et suggestions pertinentes et bienveillantes.

Merci à Kamal El Kadi Abderrezzak de m'avoir aidé sur la partie transport sédimentaire, et d'avoir toujours pris le temps, lors de discussions amicales, de répondre à mes nombreuses questions.

Je tiens aussi à remercier Pablo pour sa gentillesse, son aide continuelle, et sa relecture attentive du manuscrit. Par ailleurs, ce fut une chance de travailler avec quelqu'un avec qui je partage une passion commune. Ces trois années ont commencé par de longues conversations autour des Pink Floyd et autres héros de la musique progressive. Mais finalement, on a vite pris sur nous de surpasser ces amateurs, modeste tâche à laquelle on s'est attelés, assidus, un midi par semaine pendant plus de deux ans et demi ! Une belle rencontre et une aventure qui continue.

Un grand merci à Charles Bodel qui a été un chef de groupe bienveillant et qui m'a vendu ma première guitare !

Mes remerciements vont également aux autres thésards du laboratoire. Je pense particulièrement à ceux qui ont partagé mon bureau : Raffaello (ce fut un plaisir de refaire le monde de 9h à 9h30 pendant un an et demi), Steve et Cécile, puis Adrien (à défaut d'avoir ton doctorat, je suis sûr que tu seras un grand champion de Clash Royal), Jérémie et Sofian (merci pour tes leçons de musique). Ça a été un réel plaisir de passer ces trois années avec vous tous. Je remercie aussi particulièrement Rémi qui m'a beaucoup aidé

pendant ces trois ans. J'ai, par ailleurs, adoré nos longues discussions, qu'elles fussent scientifiques ou simplement geeks !

Je remercie sans pouvoir tous les citer, tous ceux qui m'ont apporté leur aide pendant ces trois ans, notamment Alexis Hérault.

Pour finir, j'aimerais remercier mes proches, et en particulier mes parents qui ont toujours fait tout leur possible pour que je puisse suivre la voie qui me plait. Merci pour votre soutien indéfectible, vous êtes les artisans officieux de ma réussite. Merci à ma merveilleuse compagne Virginie, de m'avoir soutenu au quotidien, de m'avoir rassuré et apaisé dans les moments difficiles. Je crois que si je suis toujours plutôt calme et serein, c'est qu'avec toi la vie est belle quoi qu'il arrive.

Contents

List of Figures

List of Tables

Nomenclature

Acronyms

GPU Graphics Processing Unit

SPH Smoothed Particle Hydrodynamics

USAW Unified semi-analytical wall boundary conditions

WCSPH Weakly Compressible SPH

Greek Symbols

δr Initial interparticle distance ..... m

Δt Time-step ..... s

Δ Chequerboard correction term ..... $\mathrm{N} \cdot \mathrm{m}^{-3}$

$\underline{\underline{\dot{\omega}}}$ Rotation rate tensor ..... s^{-1}

η Dynamic viscosity ..... $\mathrm{Pa} \cdot \mathrm{s}$

η_∞ Plastic viscosity in Bingham's model ..... $\mathrm{Pa} \cdot \mathrm{s}$

$\dot{\gamma}$ Strain rate magnitude ..... s^{-1}

Γ Kernel renormalization factor

κ Bulk viscosity ..... $\mathrm{Pa} \cdot \mathrm{s}$

Λ Chequerboard correction coefficient

λ First Lamé's constant ..... Pa

ν Poisson's coefficient

Ω Computational domain

$\partial\Omega$ Boundary of the computational domain

ϕ	Porosity
ψ	Internal friction angle
ρ	Density ..... $\mathrm{kg} \cdot \mathrm{m}^{-3}$
ρ_0	Reference density in WCSPH ..... $\mathrm{kg} \cdot \mathrm{m}^{-3}$
τ	Shear stress magnitude ..... Pa
$\underline{\underline{\sigma}}$	Cauchy stress tensor ..... Pa
$\underline{\underline{\tau}}$	Deviatoric component of Cauchy stress tensor ..... Pa
$\underline{\underline{\gamma}}$	Deformation tensor
$\underline{\underline{\dot{\gamma}}}$	Strain rate tensor ..... s^{-1}
θ	Angular volume fraction in USAW boundary conditions
Ξ	Micro-mixing correction term ..... $\mathrm{N} \cdot \mathrm{m}^{-3}$
ξ	Isentropic coefficient in Tait's equation of state
ζ	Blending function in the elastic-viscoplastic model

Roman Symbols

d_g	Grain size ..... m
$\mathcal{G}$	Shear modulus ..... Pa
$\mathcal{F}$	Set of free particles
$\mathcal{I}$	Set of free SPH particles at water-granular interface
$\mathcal{M}$	Set of granular phase SPH particles
$\mathcal{S}$	Set of boundary elements (segments in 2D)
$\mathcal{V}$	Set of vertex particles
$\mathcal{W}$	Set of water phase SPH particles
$\overline{E}$	Time-averaged error
$\overline{m}$	Reference mass in USAW ..... kg
$\overline{V}$	Reference volume in USAW ..... $\mathrm{m}^{-\mathrm{d}}$
$\underline{\underline{\dot{J}}}$	Jaumann stress rate tensor ..... $\mathrm{Pa} \cdot \mathrm{s}^{-1}$

$\underline{\underline{f}}$	Force density	$\mathrm{N} \cdot \mathrm{m}^{-3}$
$\underline{\underline{I}}$	Identity matrix	
$\underline{\underline{J}}$	Anti-derivative of the Jaumann stress rate tensor	Pa
$\underline{G}$	SPH gradient operator	
$\underline{g}$	Gravitational acceleration	$\mathrm{m} \cdot \mathrm{s}^{-2}$
$\underline{n}$	Unit normal vector to the boundary	
$\underline{r}$	Position vector	m
$\underline{u}$	Velocity	$\mathrm{m} \cdot \mathrm{s}^{-1}$
$\underline{X}$	Displacement vector	m
Bn	Bingham number	
c	Numerical speed of sound in WCSPH	$\mathrm{m} \cdot \mathrm{s}^{-1}$
D	SPH divergence operator	
d	Space dimension of the computational domain	
E	Young's modulus	Pa
h	Smoothing length	m
I_1	First invariant of the Cauchy Stress	Pa
J_2	Second invariant of the Cauchy Stress deviator tensor	Pa^2
J_3	Third invariant of the Cauchy Stress deviator tensor	Pa^3
L	SPH second order operator	
m	Mass	kg
Ma	Mach number	
p	Pressure	Pa
p^*	Dynamic pressure	Pa
Re	Reynolds number	
t	Time	s
V	Volume	$\mathrm{m}^{-\mathrm{d}}$

w SPH kernel ..... $\mathrm{m}^{-\mathrm{d}}$

De Deborah number

Superscripts

E Español and Revenga's SPH second order operator

H Hu and Admas' second SPH order operator

M Morris*et al.*'s SPH second order operator

bound Boundary term of SPH operator in USAW boundary conditions

l Liquid state of the granular phase

s Solid state of the granular phase

Subscripts

0 Reference quantities in WCSPH

a SPH particle of interest

b SPH neighbouring particle

s Boundary elements (segments in 2D) in USAW boundary conditions

v Vertex particles in USAW boundary conditions

w Wall boundary of the computational domain

eff Effective quantities in the granular phase

eq Equivalent quantities in the granular-water mixture

g Granular phase

th Theoretical solution

w Water phase

y Yield quantities in the granular phase

Other Symbols

$\underline{\nabla}\Gamma$ Gradient of the renormalization factor Γ ..... m^{-1}

$\underline{\nabla}w$ SPH kernel gradient..... $\mathrm{m}^{-\mathrm{d}-1}$

Introduction

L'étude du transport sédimentaire présente des aspects stratégiques majeurs pour de nombreux secteurs industriels. Les enjeux sont à la fois environnementaux, économiques et sécuritaires. Les opérations de gestion des sédiments requises pour l'entretien des retenues en amont des barrages présentent, par exemple, des coûts considérables. Il en va de même des problématiques d'affouillement au pied des ouvrages fluviaux ou côtiers qui nécessitent des stratégies de surveillance et de maintenance à long terme. L'étude du transport sédimentaire a donc pour but de comprendre et de prédire ces phénomènes, afin de mettre en place des solutions adaptées et d'anticiper ou de réduire les coûts qui en résultent. Le transport sédimentaire a été largement étudié expérimentalement et numériquement. Si les modèles numériques couramment proposés dans la littérature reposent sur un solveur hydrodynamique couplé à des lois semi-empiriques pour la prise en compte du transport sédimentaire, une approche différente est proposée ici. Le modèle développé dans ce travail inclut la résolution de la dynamique du sédiment par charriage. Celui-ci est assimilé à un milieu continu dont la loi de comportement rend compte de la nature granulaire. Pour ce faire, le modèle élastique-viscoplastique d'Ulrich [114] est implémenté dans un code pré-existant, et amélioré dans le cadre d'une formulation SPH multiphasique avec conditions aux limites semi-analytiques.

(a) (b)

Figure 1: (a) Silting-up at the Flamanville cooling water intake (Credit: EDF). (b) Bridge scour photography (Credit: Public Domain Images – USGS [4]).

Sediment transport is a major concern for many industrial activities and environmental purposes. On the one hand, hydraulic structures are likely to impact the natural sediment transport, leading to environmental issues. On the other hand, the transported sediment and the corresponding changes of the bed topography can affect the proper functioning of industrial structures. The hydroelectric dam operation is a relevant example. Such a structure traps sediments carried down by the river. The resulting decrease of sediment supply leads to an increase of erosion downstream of the dam, and thus to a modification of biological, chemical and physical properties of the soil. The environmental impact of such a change has to be evaluated and limited in line with the legal standards. Besides that, the trapping results in sediment accumulation in the reservoir that reduces water-storage capacity and decreases the production capacity of the dam. Furthermore sediment transport not only raises environmental and economical issues, it is also a matter of industrial safety. In particular, the silting of nuclear plants headrace canals is a crucial issue for nuclear safety (see Figure 1a). Scouring is also a well known problematical phenomenon that can affect foundation stability of dams, offshore wind turbines and bridges (see Figure 1b). As an example, 60% of bridge failures occurred between 1950 and 1992 in the United States were due to scour around bridge foundations or channel instability such as bank failure [64].

The aim of sediment transport study is then to be able to predict these phenomena, to find suitable solutions and to anticipate the resulting spendings. This subject is thus widely investigated experimentally and numerically. The high cost of experimental investigations makes numerical modelling a useful additional tool to study sediment transport. The state-of-the-art simulation methods commonly rely on a fluid dynamics solver coupled to semi-empirical relationships to model the sediment transport (see *e.g.* [32, 77]). As

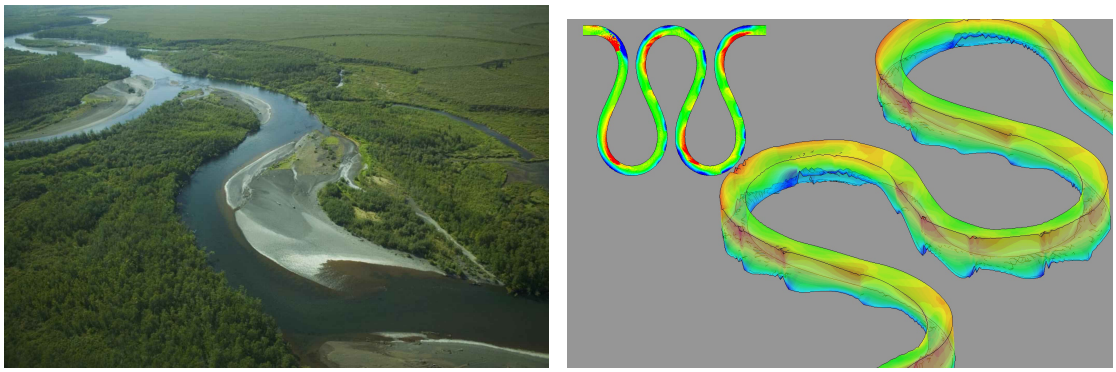

(a) (b)

Figure 2: (a) Meandering river photography (Credit: Public Domain Images – PIXNIO [2]). (b) Meandering simulation carried with TELEMAC-MASCARET modelling system [123].

regards the bed load transport, the bed evolution is usually obtained from Exner's mass balance equation combined to transport formulae involving the empirical Shields erosion criterion. Therefore, the sediment is not explicitly modelled and the bed evolution is taken into account through the evolution of the mesh geometry. Despite that, this approach has proven its efficiency in modelling bed load transport for large scale problems. Such numerical tools have been developed by the EDF National Laboratory for Hydraulics and Environment (LNHE) to model large scale sediment transport phenomena [3]. As an example, Figure 2a shows a photography and a simulation of a meandering river, which is typically a large spatio-temporal scale phenomenon.

With those classical approaches, the sediment dynamics within the bed is not considered. They are thus poorly adapted to phenomena in which the mechanical behaviour of the sediment is significantly important, especially when they involve highly dynamic behaviour. Phenomena like local scour, flow-induced erosion or landslide-induced water waves are, for instance, difficult to model with the classical techniques described above. To represent accurately these phenomena, a proper treatment of the mechanical behaviour of the sediment and of the sediment-water interaction are both necessary. Such flows involve several phases and exhibit highly non-linear deformations. They are common in applied hydrodynamics problems and raise many scientific and technical issues. With this in mind, a completely different approach is thus investigated in this thesis.

The sediment is explicitly represented as a continuous phase having its own macroscopic physical properties. It is treated as a continuum whose constitutive equation takes account for its granular nature. The physics of granular material is thus used to model the sediment. The bed-load transport process then results from the interaction between the water phase and the granular phase. Modelling granular materials is particularly diffi-

cult because they behave with some respect to both liquids and solids depending of the internal stress configuration. As a first approximation, they can suitably be assimilated to viscoplastic materials. Below a critical shear-stress the material behaves like a solid. When the critical shear stress is exceeded, failure occurs, the material starts to flow and exhibits a shear thinning behaviour. Numerically, the solid state is usually approached by a highly viscous state. This kind of pseudo-viscoplastic model has been applied in the frame of finite volumes [85]. However, with such a multi-phase mesh-based method, the presence of a free-surface requires to solve the air-flow and to reconstruct interfaces between the three phases. Moreover, the highly non-linear deformations and the interface fragmentation make these problems difficult to treat with traditional mesh-based Eulerian methods.

On the contrary, Lagrangian approaches are particularly adapted for modelling such phenomena. Pseudo-viscoplastic models have also been successfully applied in the frame of the Smoothed Particle Hydrodynamics method (SPH). SPH is a Lagrangian meshfree numerical method for simulating the dynamics of continuous media. Test cases such as saturation driven embankment failure [114], submarine landslide [19, 126]), scouring and sediment flushing problems [41, 74] have been successfully treated with this method. Since it has proved its ability to perform well in such cases, and considering that LNHE has developed an in-house SPH code for fluids, the development of the present work will be done in the frame of an SPH formulation based on the above-mentioned code. The aim of this thesis is therefore to develop an SPH model able to represent the solid and liquid behaviours of granular materials, to capture the failure process as well as the solid-liquid regime transitions. The model should also be able to handle multi-phase flows[1] and to represent the bed load transport process as a consequence of the water-sediment interaction. The main achievements of this work are:

- The improvement of Hu and Adams's [58] multi-phase SPH formulation, extending it to the semi-analytical wall boundary conditions technique and to free-surface flows;
- The development of an implicit viscous forces integration scheme in the frame of the semi-analytical wall boundary conditions;
- Three main improvements of Ulrich's [114] elastic-viscoplastic model:
  - A liquid-solid transition threshold criterion based on the physical properties of the sediment material;
  - A method to compute accurately the effective pressure that is compulsory to capture the material failure;

[1] In this work the term *multi-phase flows* refers to flows involving several immiscible materials. This designation is preferred to *multi-fluid* because various constitutive equations are used to describe the mechanical behaviour of the granular material. However, the present model is not a mixture model: SPH particles represent a small volume of one of the phases, and no mass transfer occurs between them.

– A numerical technique to improve the accuracy of elastic forces computation.

These developments were implemented in EDF's in-house research SPH code (Sphynx) derived from the open-source software GPUSPH [1], and was written in the Cuda programming language for GPU.

The thesis is divided in five chapters:

- In Chapter 1 the governing equations describing the motion of a weakly compressible continuum are briefly presented.
- Chapter 2 outlines the standard SPH formulation. The continuous and discrete formalisms are introduced and the SPH approximations of the governing equations are derived. The semi-analytical wall boundary conditions technique and the chequerboard correction methods are then described. The implicit viscous forces integration scheme is finally presented.
- Chapter 3 deals with the multi-phase formulation in SPH. A short review of the main existing models is followed by the description of the present model.
- In Chapter 4, the constitutive model for the granular material is presented. The modelling hypothesis are presented in detail. The yield criteria and the elastic-viscoplastic model are then described. The corresponding SPH implementation is then detailed.
- In Chapter 5, the multi-phase model, the implicit viscous forces integration scheme and the elastic-viscoplastic model are tested on various validation test cases.

Chapter 1

Governing equations

L'objectif de ce chapitre est de présenter le système d'équations étudié dans ce travail. Il s'agit donc d'écrire les lois de conservation qui s'appliquent dans le cadre de la mécanique des milieux continus (fluides ou solides) faiblement compressibles. Des exemples classiques de lois de comportement sont également rappelés, ainsi que les conditions aux limites qui seront utilisées dans ce travail.

This chapter aims at presenting the governing equations describing the motion of a weakly compressible continuum.

1.1 Mass conservation equation

The local conservation of mass in a continuum is expressed by the continuity equation. In its Lagrangian form, it reads:

$$\frac{d\rho}{dt} = -\rho \operatorname{div} \underline{u} \tag{1.1}$$

with $\frac{d}{dt}$ the material derivative, ρ the density field of the medium, t the time and $\underline{u}$ the velocity field. If the medium is incompressible, in principle this equation leads to:

$$\operatorname{div} \underline{u} = 0 \tag{1.2}$$

In the subsequent derivations of the governing equations, we will sometimes use (1.2). However, the governing equation (1.1) will be used to allow the density to vary slowly in our dynamic model. This is the so-called *weakly compressible* assumption.

1.2 Momentum conservation equation

The local conservation of linear momentum in a continuum is described by the Cauchy momentum equation. In Lagrangian form, it is written as:

$$\frac{d\underline{u}}{dt} = \frac{1}{\rho} \underline{\operatorname{div}}\, \underline{\underline{\sigma}} + \underline{g} \tag{1.3}$$

with $\underline{g}$ the gravity and $\underline{\underline{\sigma}}$ the Cauchy stress second order tensor field.

1.2.1 The Cauchy stress tensor

Let us write the Cauchy stress tensor $\underline{\underline{\sigma}}$ in three dimensions:

$$\underline{\underline{\sigma}} = \begin{pmatrix} \sigma_{xx} & \sigma_{xy} & \sigma_{xz} \\ \sigma_{yx} & \sigma_{yy} & \sigma_{yz} \\ \sigma_{zx} & \sigma_{zy} & \sigma_{zz} \end{pmatrix} \tag{1.4}$$

From the balance of angular momentum, it can be shown that the Cauchy stress tensor is symmetric, see *e.g.* Violeau [119]. As a square and symmetric matrix, the stress tensor is diagonalizable. In its orthonormal eigenbasis $(\underline{e}_1, \underline{e}_2, \underline{e}_3)$, the shear stress components

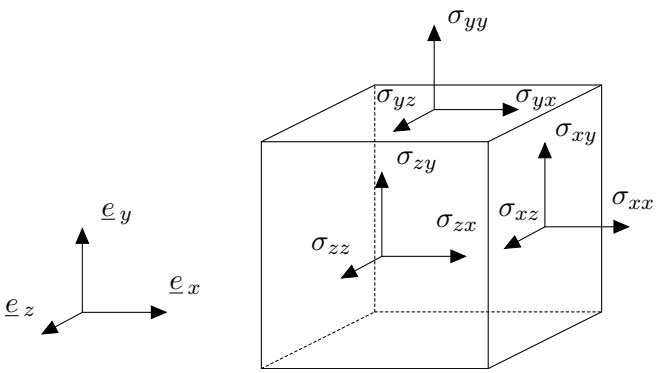

Figure 1.1: Component of the Cauchy stress tensor in three dimensions

become zero so that only three components remain:

$$\underline{\underline{\sigma}} = \begin{pmatrix} \sigma_1 & 0 & 0 \\ 0 & \sigma_2 & 0 \\ 0 & 0 & \sigma_3 \end{pmatrix} \tag{1.5}$$

The components σ_1, σ_2 and σ_3 are defined as the principal stresses and they are independent of any coordinate system. We can choose to reorder the eigen vectors of the basis so that:

$$\sigma_1 \geq \sigma_2 \geq \sigma_3 \tag{1.6}$$

Thus, σ_1, σ_2 and σ_3 are respectively the major, the intermediate and the minor principal stresses. The eigen vectors defines the so-called principal directions. Like every tensor, $\underline{\underline{\sigma}}$ can be decomposed in a an isotropic tensor (*i.e.* proportional to the identity tensor) and a deviatoric tensor (*i.e.* traceless tensor):

$$\underline{\underline{\sigma}} = \left(\underline{\underline{\sigma}} - \frac{1}{3}\,\mathrm{Tr}\left(\underline{\underline{\sigma}}\right)\underline{\underline{I}}\right) + \frac{1}{3}\,\mathrm{Tr}\left(\underline{\underline{\sigma}}\right)\underline{\underline{I}} \tag{1.7}$$

with $\underline{\underline{I}}$ the identity tensor. The isotropic tensor corresponds to the stress acting equally in all the directions from which the pressure p is defined:

$$p = \frac{1}{3}\mathrm{Tr}(\underline{\underline{\sigma}}) \tag{1.8}$$

The deviatoric tensor corresponds to the shear stress tensor $\underline{\underline{\tau}}$ thus defined by:

$$\underline{\underline{\tau}} = \underline{\underline{\sigma}} - p\underline{\underline{I}} \tag{1.9}$$

Let us now define some invariants of the tensors $\underline{\underline{\sigma}}$ and $\underline{\underline{\tau}}$ that will be useful within the

scope of this work. The first invariant of the Cauchy Stress tensor is denoted I_1 and is defined by:

$$I_1 = \mathrm{Tr}\left(\underline{\underline{\sigma}}\right) = \sigma_1 + \sigma_2 + \sigma_3 \tag{1.10}$$

The second invariant of $\underline{\underline{\tau}}$, is denoted J_2 and reads:

$$J_2 = \frac{1}{2}\,\underline{\underline{\tau}} : \underline{\underline{\tau}} \tag{1.11}$$

In terms of principal stresses, it can be written as:

$$J_2 = \frac{1}{6}\left((\sigma_1 - \sigma_2)^2 + (\sigma_1 - \sigma_3)^2 + (\sigma_2 - \sigma_3)^2\right) \tag{1.12}$$

Finally the third invariant J_3 of the deviatoric stress tensor is defined by:

$$J_3 = \det \underline{\underline{\tau}} \tag{1.13}$$

And it can be written in terms of principal stresses as:

$$J_3 = -(\sigma_1 + \sigma_2)(\sigma_1 + \sigma_3)(\sigma 2 + \sigma_3) \tag{1.14}$$

1.2.2 constitutive equations

The Cauchy momentum equation (1.3) applies to any continuum, but one sees that it is not in a closed-form because the pressure (1.8) and shear stress (1.9) are undefined. Thus for every material, a suitable constitutive equation has to be used to relate pressure and shear stress to kinematic quantities. With the weakly compressible approach, the pressure will be evaluated though an equation of state that will be presented in Section 1.3. In this section, we present the constitutive equations that will be used to model the deviatoric part of shear stress tensor.

1.2.2.1 Viscous fluid constitutive equation

For a viscous fluid, $\underline{\underline{\tau}}$ can be expressed using Stokes' stress constitutive equation:

$$\underline{\underline{\tau}} = 2\,\eta\,\underline{\underline{\dot{\gamma}}} + \left(\kappa - \frac{2}{3}\eta\right)\mathrm{div}\,(\underline{u})\;\underline{\underline{I}} \tag{1.15}$$

with $\underline{\underline{I}}$ the identity matrix, η and κ the dynamic and the bulk viscosities respectively, and $\underline{\underline{\dot{\gamma}}}$ the strain rate tensor defined by:

$$\underline{\underline{\dot{\gamma}}} = \frac{1}{2}\left(\underline{\underline{\text{grad}}}\,\underline{u} + \left(\underline{\underline{\text{grad}}}\,\underline{u}\right)^T\right) \tag{1.16}$$

where ^{T} denotes the transpose of a tensor. Substituting the constitutive equation (1.15) into the equation of motion (1.3) leads to the Navier–Stokes' momentum equation. With the assumption of weakly compressible fluid (1.2), the right-hand side in equation (1.15) simplifies to the second equation of the system below:

$$\begin{cases} \dfrac{d\rho}{dt} = -\rho\,\text{div}\,\underline{u} \\ \dfrac{d\underline{u}}{dt} = -\dfrac{1}{\rho}\underline{\underline{\text{grad}}}\,p + \underline{g} + \dfrac{1}{\rho}\underline{\underline{\text{div}}}\left[\eta\left(\underline{\underline{\text{grad}}}\,\underline{u} + \left(\underline{\underline{\text{grad}}}\,\underline{u}\right)^T\right)\right] \\ \underline{u} = \dfrac{d\underline{r}}{dt} \end{cases} \tag{1.17}$$

With the first line (which is the continuity equation (1.1) introduced in section 1.1) and the third line (Lagrangian kinematic displacement, $\underline{r}$ being the position vector), this constitutes the system of equations used in this work for a Newtonian weakly compressible fluid.

1.2.2.2 Isotropic linear elastic constitutive equation

For an isotropic linear elastic material, the three-dimensional generalized Hooke's law relates the strain tensor $\underline{\underline{\gamma}}$ to the Cauchy stress tensor $\underline{\underline{\sigma}}$ as:

$$\underline{\underline{\sigma}} = 2\,\mathcal{G}\,\underline{\underline{\gamma}} + \lambda \text{Tr}(\underline{\underline{\gamma}})\,\underline{\underline{I}} \tag{1.18}$$

where λ and $\mathcal{G}$ are the Lamé's constants and the strain tensor $\underline{\underline{\gamma}}$ can be written as:

$$\underline{\underline{\gamma}} = \frac{1}{2}\left(\underline{\underline{\text{grad}}}\,\underline{X} + \left(\underline{\underline{\text{grad}}}\,\underline{X}\right)^T\right) \tag{1.19}$$

with $\underline{X}$ the displacement vector:

$$\underline{X}(t) = \int_0^t \underline{u}(t')\,dt' = \underline{r}(t) - \underline{r}(0) \tag{1.20}$$

The Lamé's constants can be expressed in terms of Young's modulus E and Poisson's ratio ν as:

$$\lambda = \frac{E\nu}{(1+\nu)(1-2\nu)}, \qquad \mathcal{G} = \frac{E}{2(1+\nu)} \tag{1.21}$$

Young's modulus is a mechanical property of linear elastic solid materials that defines the relationship between normal stress (compression or traction) and strain in a material. Poisson's ratio is the signed ratio of transverse strain to axial strain. It is a measure of how a material tends to expand (or contract) in directions perpendicular to the direction of compression (or stretch). For incompressible materials, Poisson's ratio is equal to 0.5 so λ is undefined. Thus calculating the stress tensor from (1.18) is not possible for incompressible materials. Thus, similarly to many authors in SPH literature [48, 99, 114], Hooke's law will be used to model the deviatoric part of the stress tensor, while an equation of state will be used to compute the pressure (see Section 1.3). Note that Bui et al. [16] proposed an alternative method in which the pressure within the material is derived from the constitutive equations (see also [90] for more details). While promising, this method was not tested here and Hooke's law was only used for the deviatoric stress tensor:

$$\underline{\underline{\tau}} = 2\,\mathcal{G}\,\underline{\underline{\gamma}} \tag{1.22}$$

$$p = p(\rho) \tag{1.23}$$

Only the second Lamé's constant $\mathcal{G}$ remains. It is also referred to as the shear modulus. Thus, the system of equations governing such a material is similar to (1.17) except the right-hand side of the momentum equation:

$$\begin{cases} \dfrac{d\rho}{dt} = -\rho \operatorname{div} \underline{u} \\ \dfrac{d\underline{u}}{dt} = -\dfrac{1}{\rho}\underline{\operatorname{grad}}\, p + \underline{g} + \dfrac{1}{\rho}\underline{\operatorname{div}}\left[\mathcal{G}\left(\underline{\underline{\operatorname{grad}}}\,\underline{X} + \left(\underline{\underline{\operatorname{grad}}}\,\underline{X}\right)^T\right)\right] \\ \underline{u} = \dfrac{d\underline{r}}{dt} \end{cases} \tag{1.24}$$

1.3 System closure: the weakly-compressible approach

In order to close the systems (1.17) and (1.24), an additional equation is necessary to calculate the pressure field of the medium. The considered materials are assumed to be barotropic and weakly-compressible. For isentropic flows of water, the Tait's [108] equation of state is usually chosen:

$$p = \frac{\rho_0 c_0^2}{\xi}\left(\left(\frac{\rho}{\rho_0}\right)^{\xi} - 1\right) \tag{1.25}$$

with ρ_0 the reference density of the fluid, c_0 the reference numerical speed of sound and ξ the isentropic coefficient. It should be highlighted that this model is less physical than numerical. The main idea is to allow the density to vary because of the particle

Lagrangian motion, while maintaining the compressibility as weak as possible thanks to a large enough speed of sound. Such a state equation has also been successfully used to compute the pressure in a linear elastic material in the SPH literature, *e.g.* in [48, 114]. The weakly-compressible assumption is verified when the numerical Mach number is low enough. In practise the following criterion is usually used:

$$Ma = \frac{U_{\max}}{c_0} < 0.1 \tag{1.26}$$

with $U_{\max}$ the maximum velocity expected in the considered simulation. This allows the relative density variations to remain below 1%, since they are order Ma^2 [82]. However, some authors (*e.g.* Violeau [119]) spotted that an additional condition arises for free-surface flows, leading to the following definition of the reference numerical speed of sound:

$$c_0 = 10 \max(U_{\max}, \sqrt{gH_{\max}}) \tag{1.27}$$

where $H_{\max}$ is the maximum vertical elevation of the material, to account for hydrostatic density variations. Finally, the local speed of sound can be derived from the state equation (1.25):

$$c = \sqrt{\frac{\partial p}{\partial \rho}} = c_0 \sqrt{\left(\frac{\rho}{\rho_0}\right)^{\xi - 1}} \tag{1.28}$$

Monaghan [82] recommends $\xi = 7$ for water, but the purely numerical character of the present closure made it possible to use $\xi = 1$ in many publications [6, 48, 75]. In this work, we use $\xi = 7$ for all materials.

1.4 Boundary conditions

The equations of motion (1.17) and (1.24) apply within the continuum domain Ω, but they require additional constraints to be solved: initial and boundary conditions. Some of the most common boundary conditions are recalled here. The domain boundary will be denoted $\partial\Omega$.

1.4.1 Boundary conditions at fluid-wall interfaces

Considering any fluid and an impermeable wall, there is no mass transfer across the boundary. As a consequence the normal component of velocity must be continuous:

$$(\underline{u} \cdot \underline{n})_{\partial\Omega_w} = \underline{u}_w \cdot \underline{n} \tag{1.29}$$

with $\underline{u}_w$ the prescribed local wall velocity, $\partial\Omega_w$ the solid wall boundary and $\underline{n}$ the unit outward vector normal to the wall. Besides, for a viscous fluid, the friction exerted on the wall leads to a no-slip condition:

$$[\underline{u} - (\underline{u} \cdot \underline{n})]|_{\partial\Omega_w} = \underline{u}_w - (\underline{u}_w \cdot \underline{n}) \tag{1.30}$$

Thus for viscous fluids, conditions (1.29) and (1.30) simply result in a Dirichlet condition on the fluid velocity:

$$\underline{u}|_{\partial\Omega_w} = \underline{u}_w \tag{1.31}$$

From (1.31), it is possible to write a condition for the pressure, see *e.g.* [119]. As a first approximation, this is written as:

$$\left.\frac{\partial p^*}{\partial \underline{n}_w}\right|_{\partial\Omega_w} = 0 \tag{1.32}$$

with $\underline{n}_w$ the unit vector normal to the wall and p^* the dynamical pressure defined by:

$$p^* = p - \rho\, \underline{g} \cdot \underline{r} \tag{1.33}$$

1.4.2 Boundary conditions at fluid-fluid interfaces

The law of action-reaction implies that, on an interface $\partial\Omega_I$ of two different media of normal $\underline{n}$, the stress $\underline{\underline{\sigma}} \cdot \underline{n}$ is continuous. This leads to the continuity of pressure and shear stress across the interface:

$$\begin{aligned} [p]_{\partial\Omega_I} &= 0 \\ \left[\underline{\underline{\tau}} \cdot \underline{n}\right]_{\partial\Omega_I} &= \underline{0} \end{aligned} \tag{1.34}$$

where the brackets $[.]_{\partial\Omega_I}$ denotes the discontinuity across the interface. Equations (1.34) correspond to dynamic conditions. For the particular case of the interface with the atmosphere, referred to as a free-surface $\partial\Omega_{\mathrm{FS}}$, the shear stress can be neglected at the interface because of the small air dynamic viscosity. As a consequence, (1.34) reduces to a Dirichlet condition on pressure:

$$p_{|\partial\Omega_{\mathrm{FS}}} = p_{\mathrm{atm}} \tag{1.35}$$

with p_{atm} the atmospheric pressure. Note that in practise, a homogeneous Dirichlet condition can be used since the equations of motion only depends on the pressure gradient.

Considering immiscible viscous fluids, the kinematic condition states that the velocities

should also be continuous across the interface:

$$[\underline{u}]_{\partial\Omega_I} = 0 \tag{1.36}$$

Chapter 2

Fundamentals of Smoothed Particle Hydrodynamics

Ce chapitre donne une présentation générale de la méthode Smoothed Particle Hydrodynamics (SPH). Le formalisme est présenté en deux étapes. Le procédé d'interpolation continue est d'abord explicité. On présente ensuite l'interpolation Lagrangienne continue ainsi que la méthode de construction des opérateurs différentiels approchés. Les propriétés requises de la fonction d'interpolation sont également discutées. Vient ensuite l'étape d'interpolation discrète qui conduit à la construction de l'interpolation SPH et des opérateurs différentiels discrets. Avec ces outils, une formulation SPH classique est dérivée à l'aide d'un principe variationnel Lagrangien dans le cadre d'un domaine infini. Les forces visqueuses sont ensuite introduites pour le traitement des fluides. Les techniques classiques de modélisation des parois solides par SPH sont ensuite rapidement évoquées, avant de détailler le modèle de conditions aux limites semi-analytiques utilisé dans ce travail. Enfin, on présente deux stratégies de traitement des oscillations numériques du champ de pression.

2.1 Context

Smoothed-particle hydrodynamics (SPH) is a Lagrangian meshfree numerical method for simulating the dynamics of continuous media. It was initially developed to provide an alternative to the Finite Difference Method (FDM) in the modelling of non-axisymmetric phenomena in astrophysics [43, 73]. Indeed, FDM required a huge number of grid points in order to deal with such anisotropic problems. Another difficulty was the lack of well defined boundary that is hard to handle with mesh-based methods. Besides being robust and simple to implement, SPH allows a reasonable accuracy for a small number of points, hence it was particularly suitable for this kind of applications. SPH was then extended to the simulation of problems involving large deformations, impacts and fractures in elastic materials [18, 68, 69] and finally to free-surface flows [82].

In SPH the continuum is divided in a set of material points, thereafter referred to as particles, that moves at matter velocity. The SPH particles carry physical quantities (*i.e.* mass, volume, velocity, pressure, etc.) and their motion is governed by discrete equations of motion, obtained from the interpolation of fields and suitable discrete differential operators. These discrete equations mimic the continuous governing equations presented in Chapter 1.

An asset of SPH is that, contrary to Eulerian (mesh-based) methods, the computational domain is not entirely discretized: only the matter region has to be. This leads to a method suitable for the simulation of free-surface flows, in which the computation is only in the water domain leading to a consequent reduction of the computational cost and simplification of the discretization process. Also, the fluid boundaries naturally result from the particle-based nature of SPH, making it ideal for problems involving highly deformed interfaces.

SPH relies on a continuous Lagrangian interpolation of physical fields. It is based on the use of a kernel that weights the contribution of neighbouring points depending on their distance to the point of interest. The discrete Lagrangian interpolation is then built sampling the continuous medium in a set of material points and using suitable mathematical tools.

2.2 SPH continuous formalism

In the following section, we consider a scalar field A in a domain Ω, but the same procedure can be applied to vector or tensor fields. To simplify the notation, the time dependency will be omitted. The position vector is denoted $\underline{r}$ and is defined by:

$$\underline{r} = \sum_{i=1}^{d} r_i \, \underline{e}_i \tag{2.1}$$

with d the space dimension, $(\underline{e}\,)_{i\in\{1,..,d\}}$ a set of basis vectors of $\mathbb{R}^d$ and $(r_i)_{i\in\{1,..,d\}}$ the coordinates is this basis.

2.2.1 Continuous interpolation

Let us start writing the field value at position $\underline{r}$ as the spatial convolution product with the Dirac distribution δ:

$$\begin{aligned} A\,(\underline{r}\,) &= (A * \delta)\,(\underline{r}\,) \\ &= \int_\Omega A\,(\underline{r}\,)\,\delta\,(\underline{r} - \underline{r}\,')\,d\underline{r}\,' \end{aligned} \tag{2.2}$$

with Ω the computational domain. The key idea of SPH is then to substitute the Dirac distribution by a similar but smoother interpolation function w, called herein the kernel. The kernel extends in space over a domain of typical length h, called the smoothing length (a more precise definition will be given later). More details about the kernel can be found in Section 2.2.2. The continuous interpolation reads:

$$[A](\underline{r}\,) = \int_\Omega A(\underline{r}\,')w(\underline{r} - \underline{r}\,')d\underline{r}\,' \tag{2.3}$$

the brackets $[A]$ denotes the continuous interpolation of A. An immediate consequence of substituting δ with w is that the convolution product at position $\underline{r}$ is no more exactly equal to the field value. The accuracy of this approximation mainly depends on the kernel properties to be discussed in Section 2.2.2.

2.2.2 The SPH kernel

A satisfactory kernel must fulfil several criteria in order to be suitable for the numerical simulation of physical problems. First, the kernel has be sufficiently regular (at least $\mathcal{C}^1$) in order to be able to compute the interpolation of fields derivatives (see Section 2.2.3 for more details). Besides that, when the kernel support tends to zero, we want the approximation (2.3) to tend to the exact value of the field. In other words, the kernel must tend to the Dirac distribution when the smoothing length tends to zero:

$$w(\underline{r} - \underline{r}\,') \xrightarrow{h\to 0} \delta(\underline{r} - \underline{r}\,') \tag{2.4}$$

Other necessary properties of the kernel can be deducted investigating the accuracy of the interpolation (2.3). To do so, let us write a second order Taylor expansion of $A\,(\underline{r}\,')$ around $\underline{r}$:

$$A\,(\underline{r}\,') = A\,(\underline{r}\,) - \underline{\nabla}_r A \cdot (\underline{r} - \underline{r}\,') + \mathcal{O}\left(|\underline{r} - \underline{r}\,'|^2\right) \tag{2.5}$$

where the Nabla notation $(\underline{\nabla}_r \cdot)$ stands for the gradient:

$$\underline{\nabla}_r \cdot = \sum_{i=1}^{d} \frac{\partial \cdot}{\partial r_i} \underline{e}_i \tag{2.6}$$

Substituting equation (2.5) into (2.3) yields:

$$[A](\underline{r}) = A(\underline{r}) \int_\Omega w(\underline{r} - \underline{r}')d\underline{r}' - \underline{\nabla}_r A \cdot \int_\Omega w(\underline{r} - \underline{r}')(\underline{r} - \underline{r}')\, d\underline{r} + \mathcal{O}\left(h^2\right) \tag{2.7}$$

Thus, to be first order accurate, the kernel must verify two conditions:

$$\int_\Omega w(\underline{r} - \underline{r}')d\underline{r}' = 1 \tag{2.8}$$

$$\int_\Omega w(\underline{r} - \underline{r}')(\underline{r} - \underline{r}')\, d\underline{r}' = 0 \tag{2.9}$$

The first condition states that, similarly to the Dirac distribution, the kernel integral should be equal to one. Far from the domain boundaries, this can easily be achieved through a normalizing coefficient. The second condition stipulates that the kernel first moment should be equal to zero. This can be satisfied choosing an even kernel with central-symmetrically invariant support. Denoting Ω_0 such a support centred in the domain origin we get:

$$\forall \underline{r} \in \Omega_0 \quad w(\underline{r}) = w(-\underline{r}) \tag{2.10}$$

This property is consistent with the fact that we obviously want the interpolation to have the same behaviour regardless of the direction. As a matter of fact, the kernel is usually radial:

$$\forall \underline{r} \in \Omega_0 \quad w(\underline{r}) = w(|\underline{r}|) = w(r) \tag{2.11}$$

Furthermore, the contribution of neighbouring points to the interpolation function must decrease as the distance to the support center gets larger, so the kernel has to be a decreasing function. It has also be shown that choosing positive kernel is the best physical option, see *e.g.* [119]. On the assumption of a decreasing radial function, the kernel gradient orientation can easily be determined:

$$\underline{\nabla} w(\underline{\widetilde{r}}) = \frac{\partial w(|\underline{\widetilde{r}}|)}{\partial r} \frac{\underline{\widetilde{r}}}{|\underline{\widetilde{r}}|} \tag{2.12}$$

where $\underline{\widetilde{r}} = \underline{r} - \underline{r}'$ is a vector oriented from $\underline{r}'$ to $\underline{r}$. The kernel derivative being negative, the kernel gradient is oriented from $\underline{r}$ to $\underline{r}'$. The anti-symmetry of the kernel gradient can

easily be deducted from (2.12):

$$\begin{aligned} \underline{\nabla} w\left(\underline{\widetilde{r}}\right) &= -\frac{\partial w\left(\left|-\underline{\widetilde{r}}\right|\right)}{\partial r} \frac{-\underline{\widetilde{r}}}{\left|-\underline{\widetilde{r}}\right|} \\ &= -\underline{\nabla} w\left(-\underline{\widetilde{r}}\right) \end{aligned} \tag{2.13}$$

Finally, kernels defined over a compact support are usually preferred for practical reasons. Indeed, using infinite supports implies that each particle interacts with all the particles of the domain which is computationally expensive. As a consequence, all subsequent integrals will be done on Ω_r, a circle (in 2D) or sphere (in 3D) being the kernel support centred on the point of interest $\underline{r}$. Additional conditions may be required - and recommended - for suitable kernels. The most important is that w should be positive definite, *i.e.* that its Fourier transform should be positive in order to satisfy numerical stability conditions [29, 120, 124].

In order to express the kernel in dimensionless form, we make the following change of variable:

$$q = \frac{\widetilde{r}}{h} \tag{2.14}$$

where h is the so-called smoothing length. Equation (2.3) shows that the kernel has the dimension of a length raised to the $(-d)$ power. Thus the kernel can be written with the following general form:

$$w\left(\widetilde{r}\right) = \frac{\alpha_{w,d}}{h^d} f_w(q) \tag{2.15}$$

where $\alpha_{w,d}$ is the constant used to make the kernel w satisfy the condition (2.8) in dimension d, and f_w is a positive function at least once continuously differentiable. With these notations, the kernel gradient reads

$$\underline{\nabla} w\left(\widetilde{r}\right) = \frac{\alpha_{w,d}}{h^{d+1}} f'_w(q) \frac{\underline{\widetilde{r}}}{\left|\underline{\widetilde{r}}\right|} \tag{2.16}$$

Several kernels are used in the SPH literature. In all this work, the 5th-order Wendland polynomial (also called the Wendland C_2 kernel) is used [124]. It is defined by:

$$f_w\left(q\right) = \begin{cases} \left(1 - \frac{q}{2}\right)^4 (1 + 2q) & 0 \leq q \leq 2 \\ 0 & 2 < q \end{cases} \tag{2.17}$$

The corresponding normalization constants in 1D, 2D and 3D are:

$$\alpha_{w,1} = \frac{3}{4}, \quad \alpha_{w,2} = \frac{7}{4\pi}, \quad \alpha_{w,3} = \frac{21}{16\pi} \tag{2.18}$$

The first derivative of the Wendland function (2.17) reads:

$$f'_w(q) = \begin{cases} -5q\left(1-\frac{q}{2}\right)^3 & 0 \le q \le 2 \\ 0 & 2 < q \end{cases} \tag{2.19}$$

Note that the definition of the smoothing length h is here purely arbitrary. As a better typical size of the kernel support, Dehnen and Aly [29] recommended to use the kernel standard deviation, which is proportional to h but has a universal nature, irrespective of the kernel choice (see also Violeau and Leroy [120]). However, the present work will use h as in the majority of SPH publications, since the kernel properties are not our main concern.

2.2.3 First order field derivative

The approximation (2.3) can be applied to the first-order spatial derivative of the field A:

$$[\underline{\nabla}_r A](\underline{r}) = \int_{\Omega_r} \underline{\nabla}_{r'} A(\underline{r}') w(\underline{r} - \underline{r}') d\underline{r}' \tag{2.20}$$

Integrating by part Equation (2.20) yields:

$$[\underline{\nabla}_r A](\underline{r}) = \int_{\Omega_r} \underline{\nabla}_{r'} \left[A(\underline{r}') w(\underline{r} - \underline{r}')\right] d\underline{r}' - \int_{\Omega_r} A(\underline{r}') \underline{\nabla}_{r'} w(\underline{r} - \underline{r}') d\underline{r}' \tag{2.21}$$

Here (and until we mention the SPH boundary conditions) we assume that $\partial\Omega \cup \Omega_r = \emptyset$, that is we consider a point $\underline{r}$ far from the boundary of the domain Ω. Then, applying the Gauss theorem to the Equation (2.21) and writing the compactness of w support we have:

$$\begin{cases} \displaystyle\int_{\Omega_r} \underline{\nabla}_{r'} \left[A(\underline{r}') w(\underline{r} - \underline{r}')\right] d\underline{r}' = -\oint_{\partial\Omega_r} A(\underline{r}') w(\underline{r} - \underline{r}') \underline{n}(\underline{r}') d\Sigma' \\ \forall \underline{r} \in \partial\Omega_r \quad w(\underline{r}) = 0 \end{cases} \tag{2.22}$$

where $d\Sigma'$ is a differential surface element of the boundary $\partial\Omega$ and $\underline{n}(\underline{r}')$ is the inward unit vector normal to $d\Sigma'$. Thus, the fist term in equation (2.21) vanishes. Using the anti-symmetry of the kernel gradient (2.13), we finally obtain:

$$[\underline{\nabla}_r A(\underline{r})] = \int_{\Omega_r} A(\underline{r}') \underline{\nabla}_r w(\underline{r} - \underline{r}') d\underline{r}' \tag{2.23}$$

Therefore, the interpolated gradient is obtained interpolating the field A using the kernel gradient as an interpolation function.

2.3 Discrete interpolation

2.3.1 Particles and SPH interpolation

In SPH the continuum is sampled in a set of interpolation points $\mathcal{F}$ having a constant mass m_a and referred to as *particles*. They are initially distributed homogeneously over the whole domain, representing the total volume V_0 of the continuous medium. Denoting N the number of (identical) particles used to discretize the medium of reference density ρ_0, the fixed mass of a particle a is thus:

$$m_a = \frac{V_0\,\rho_0}{N} \tag{2.24}$$

and its initial volume reads:

$$V_{a,0} = \frac{m_a}{\rho_0} \tag{2.25}$$

if we assume the initial density to be equal to its reference value. In the Weakly Compressible SPH (WCSPH) framework, the density ρ_a of a particle varies slightly through small variations of its volume $V_a = m_a/\rho_a$. However, the particle volume will stay very close to its initial value so we can define the mean diameter of particles from its initial state:

$$\delta r = (V_{a,0})^{1/d} \tag{2.26}$$

with d the dimension of the problem. The length δr is often referred to as the particle size and is also the initial interparticle distance if the particles are initially at the vertices of a Cartesian grid. The ratio between the particle size δr and the smoothing length h plays a key role since it determines the number of neighbouring particles in the kernel support. In this work (similarly to many authors [37, 66]), the following values are usually used:

$$\begin{aligned} \frac{h}{\delta r} &= 2.0 \quad \text{in 2D} \\ \frac{h}{\delta r} &= 1.3 \quad \text{in 3D} \end{aligned} \tag{2.27}$$

In order to get a discrete interpolation of the field A, we now approximate the continuous integral in equation (2.3) through Riemann sum over neighbouring particles:

$$\langle A \rangle_a = \sum_{b \in \mathcal{F}} V_b A_b w_{ab} \tag{2.28}$$

where $w_{ab} = w(|\underline{r}_a - \underline{r}_b|)$ with $\underline{r}_a$ the position of particle a, and A_a the value of the field A at the point $\underline{r}_a$. The angle brackets $\langle A \rangle_a$ denotes the discrete SPH interpolation of the field A computed at $\underline{r}_a$. Note that, unless special corrections are made to (2.28), it

does not exactly coincide with A_a (see *e.g.* Belytschko et al. [9], Bonet and Lok [13], Oger et al. [93], Vila [117]). While equation (2.7) shows that the SPH continuous interpolation leads to an error as $\mathcal{O}(h^2)$ far from the boundaries, the error made in defining the SPH discrete interpolant (2.28) is more complicated to calculate and depends on the particle distribution in space. One of the major parameters in the estimation of this error is $\delta r/h$ (see *e.g.* Quinlan et al. [98] or Violeau et al. [122])

2.3.2 First order SPH derivative operators

Applying the same procedure as in (2.28) to equation (2.23), we obtain a discrete spatial derivative (*i.e.* gradient) of the scalar field A:

$$\langle \underline{\nabla} A \rangle_a = \sum_{b \in \mathcal{F}} V_b A_b \underline{\nabla} w_{ab} \tag{2.29}$$

where $\underline{\nabla} w_{ab} = \underline{\nabla} w(r_{ab})$, r_{ab} being the distance between particles a and b, *i.e.* $r_{ab} = |\underline{r}_{ab}|$ with $\underline{r}_{ab} = \underline{r}_a - \underline{r}_b$. From (2.13) we observe that:

$$\underline{\nabla} w_{ab} = -\underline{\nabla} w_{ba} \tag{2.30}$$

However, this is not the best possible formula to approximate the spatial derivative. Indeed, for all field B and real number k we can write:

$$(\underline{\nabla} A)_k = B^k \underline{\nabla} \left(\frac{A}{B^k} \right) + \frac{A}{B^k} \underline{\nabla} \left(B^k \right) \tag{2.31}$$

Substituting the spatial derivative by the approximation (2.29) in the latter equation leads to:

$$\begin{aligned} \langle \underline{\nabla} A \rangle_{k,a} &= B_a^k \left\langle \underline{\nabla} \left(\frac{A}{B^k} \right) \right\rangle_a + \frac{A_a}{B_a^k} \left\langle \underline{\nabla} \left(B^k \right) \right\rangle_a \\ &= \sum_{b \in \mathcal{F}} V_b \frac{B_b^{2k} A_a + B_a^{2k} A_b}{(B_a B_b)^k} \underline{\nabla} w_{ab} \end{aligned} \tag{2.32}$$

Thus, the operators derived from this formula form an infinite set of discrete derivative operators. We will refer to them as anti-symmetric operators, since $\underline{\nabla} w_{ab}$ is anti-symmetric from (2.30). For $B = \rho$ and $k = 1$ we obtain one of the most common anti-symmetric gradient operator used in the SPH literature for one-fluid simulations:

$$\underline{G}_a \{A_b\} = \rho_a \sum_{b \in \mathcal{F}} m_b \left(\frac{A_a}{\rho_a^2} + \frac{A_b}{\rho_b^2} \right) \underline{\nabla} w_{ab} \tag{2.33}$$

Similarly, we can write for all field B and real number k:

$$(\underline{\nabla} A)_k = \frac{1}{B^k}\underline{\nabla}\left(B^k A\right) + B^k A \underline{\nabla}\left(\frac{1}{B^k}\right) \tag{2.34}$$

This leads to another set of discrete derivative operators, referred to as symmetric operators:

$$\langle \underline{\nabla} A \rangle_{k,a} = -\frac{1}{B_a^{2k}} \sum_{b \in \mathcal{F}} V_b (B_a B_b)^k \left(A_a - A_b\right) \underline{\nabla} w_{ab} \tag{2.35}$$

Applying (2.35) to a vector field $\underline{A}$ with a $B = \rho$ and $k = 1$ we find the classical symmetric divergence operator:

$$D_a \left\{\underline{A}_b\right\} = -\frac{1}{\rho_a} \sum_{b \in \mathcal{F}} m_b \left(\underline{A}_a - \underline{A}_b\right) \cdot \underline{\nabla} w_{ab} \tag{2.36}$$

Although it is possible to define an infinite number of derivative operators, we will see that the choice can be determined by physical arguments. Indeed, Bonet and Lok [13] showed that to build a fully consistent SPH formulation, with good conservation properties, the discrete operators used to compute the density and the momentum equation have to be variationally consistent. This issue will be addressed in Section 2.4.

2.3.3 Second order SPH derivative operators

Equations (1.17) and (1.24) both require an SPH form of second order derivative operators to be proposed. Let us start constructing an SPH Laplacian. As a first attempt, we apply twice the procedure described in Section 2.2.3, and we find:

$$\left\langle \underline{\nabla}^2 A \right\rangle = \sum_{b \in \mathcal{F}} A_b \, \underline{\nabla}^2 w_{ab} \tag{2.37}$$

Nevertheless, Monaghan [81] reported that this formula is very sensitive to the particle disorder because of the second derivative of the kernel. In addition to that, Monaghan [83] pointed out that equation (2.37) does not conserve the quantity A since the flux $A_b \, \underline{\nabla}^2 w_{ab}$ is not anti-symmetric. Therefore, Takeda et al. [109] proposed an anti-symmetric form based on the second order kernel derivative, thus restoring the conservation of A. Gonzalez et al. [47] applied it to the calculation of viscous forces and reported very accurate results for several test cases. Though, the sensitivity to particle disorder remains and Takeda et al.'s [109] second order operator is rarely used.

Another idea consists in defining the SPH Laplacian from the SPH first order operators, writing the continuous relation $\underline{\nabla}^2 = \text{div}\left(\underline{\text{grad}}\right)$:

$$\left(\operatorname{div}\left(\underline{\operatorname{grad}}\, A\right)\right)_a \approx D_a\left\{\underline{G}_b\left\{A_c\right\}\right\} \tag{2.38}$$

where D and G are the SPH divergence and gradient operators as defined, *e.g.* in (2.36) and (2.33), respectively. This method is also rarely used because it involves a twofold sum which is computationally expensive. But in addition to that, it is also numerically questionable as in SPH all the fields and derivatives are evaluated at one position, *i.e.* it relies on a collocated discretization. In mesh-based methods, it is a well known that taking the divergence of the gradient in conjunction with a collocated discretization can lead to spurious results due to the so-called chequerboard effects (see *e.g.* [15, 96, 101]). In WCSPH, this is also responsible for pressure instabilities and this issue will be addressed in Section 2.6. Thus a third approach is usually chosen, as described below.

To be more general, let us write a diffusion term of the vector field $\underline{A}$, having a dynamic diffusion coefficient J_A, using an SPH divergence and a continuous gradient:

$$\left(\underline{\operatorname{div}}\cdot\left(J_A\,\underline{\underline{\operatorname{grad}}}\,\underline{A}\right)\right)_a \approx D_a\left\{J_{A,b}\left(\underline{\underline{\operatorname{grad}}}\,\underline{A}\right)_b\right\} \tag{2.39}$$

Here we want to construct a SPH Laplacian to compute the viscous forces. It must have an anti-symmetric form to ensure the conservation of $\underline{A}$, thus the form (2.32) should be used. Note that we will see in Section 2.4 that the divergence and the gradient derived in Section 2.3.2 are variationally consistent. However, the Laplacian can be derived from other first order operators because the variational principles do not apply in presence of viscous forces. Therefore, the form (2.32) with $k = 0$ is usually preferred:

$$\left(\underline{\operatorname{div}}\cdot\left(J_A\,\underline{\underline{\operatorname{grad}}}\,\underline{A}\right)\right)_a \approx \sum_{b\in\mathcal{F}} V_b\left(J_{A,a}\left(\underline{\underline{\operatorname{grad}}}\,\underline{A}\right)_a + J_{A,b}\left(\underline{\underline{\operatorname{grad}}}\,\underline{A}\right)_b\right)\cdot\underline{\nabla} w_{ab} \tag{2.40}$$

The gradient of A is then evaluated using a Taylor series expansion:

$$\begin{aligned} A_a &= A_b + \left(\underline{\underline{\operatorname{grad}}}\,\underline{A}\right)_b\cdot\underline{r}_{ab} + O\left(r_{ab}^2\right) \quad\Rightarrow\quad \left(\underline{\underline{\operatorname{grad}}}\,\underline{A}\right)_a\cdot\underline{e}_{ab} \approx \frac{\underline{A}_a - \underline{A}_b}{r_{ab}} \\ A_b &= A_a - \left(\underline{\underline{\operatorname{grad}}}\,\underline{A}\right)_a\cdot\underline{r}_{ab} + O\left(r_{ab}^2\right) \quad\Rightarrow\quad \left(\underline{\underline{\operatorname{grad}}}\,\underline{A}\right)_b\cdot\underline{e}_{ab} \approx \frac{\underline{A}_a - \underline{A}_b}{r_{ab}} \end{aligned} \tag{2.41}$$

where $\underline{r}_{ab}$ and $\underline{e}_{ab}$ are two vectors pointing from particle b to particle a and defined as:

$$\begin{aligned} \underline{r}_{ab} &= \underline{r}_a - \underline{r}_b \\ \underline{e}_{ab} &= \frac{\underline{r}_{ab}}{|\underline{r}_{ab}|} \end{aligned} \tag{2.42}$$

Thus, combining (2.40) and (2.41) yields:

$$\left(\underline{\mathrm{div}} \cdot \left(J_A \underline{\underline{\mathrm{grad}}}\, \underline{A}\right)\right)_a \approx \sum_{b\in\mathcal{F}} V_b \left(J_{A,a} + J_{A,b}\right) \frac{\underline{A}_a - \underline{A}_b}{r_{ab}^2} \underline{\nabla} w_{ab} \cdot \underline{r}_{ab} \tag{2.43}$$

Thus we finally get a discrete form of the Laplacian involving neither the second derivative of the kernel nor a twofold sum. Introducing the arithmetic mean of the dynamic diffusion coefficient $\overline{J}_{A,ab} = \left(J_{A,a} + J_{A,b}\right)/2$, we obtain the final form that will be denoted $\underline{L}^M$ referred to as the Morris et al.'s [86] Laplacian:

$$\underline{L}^M \left\{J_{A,b}, \underline{A}_b\right\} = 2 \sum_{b\in\mathcal{F}} V_b \overline{J}_{A,ab} \frac{\underline{A}_a - \underline{A}_b}{r_{ab}^2} \underline{\nabla} w_{ab} \cdot \underline{r}_{ab} \tag{2.44}$$

This operator will be used to compute the viscous forces when modelling incompressible Newtonian fluids. In practise, using the harmonic mean instead of the arithmetic one has proved to improve numerical results in some cases [58]. It is particularly important for flows involving multiple viscosities (*i.e.* involving several fluids or a non-Newtonian rheology) where the shear stress has to be continuous across interfaces (see *e.g.* [58, 86, 118] for more details).

As shown by Espanol and Revenga [33], Monaghan [83] and properly demonstrated for any space dimension d and non-constant diffusion coefficient $J_{A,a}$ by Violeau [118], more general second order operators can be written from the following expression:

$$\left(\left(\underline{\underline{\mathrm{grad}}}\, \left[J_A \underline{\mathrm{grad}}\, A\right]\right)_{ij}\right)_a \approx \sum_{b\in\mathcal{F}} V_b \overline{J}_{A,ab} \frac{A_a - A_b}{r_{ab}^2} \left[(d+2)\, e_{ab,i} e_{ab,j} - \delta_{ij}\right] \underline{\nabla} w_{ab} \cdot \underline{r}_{ab} \tag{2.45}$$

that is the discrete approximation of the ij-th component of the tensor $\left(\underline{\underline{\mathrm{grad}}}\, \left[J_A \underline{\mathrm{grad}}\, A\right]\right)$ calculated at particle a. Here $e_{ab,i}$ denotes the i-th component of the vector $\underline{e}_{ab}$. This general form can be used to write a more general discrete second-order operator referred to as Espanol and Revenga's operator and denoted $\underline{L}^E$. It is defined by:

$$\underline{L}^E \left\{J_{\underline{A},b}, A_b\right\} = \sum_{b\in\mathcal{F}} V_b \frac{\overline{J}_{A,ab}}{r_{ab}^2} \left[(d+2)\left(\left(\underline{A}_a - \underline{A}_b\right) \cdot \underline{e}_{ab}\right) \underline{e}_{ab} + \left(\underline{A}_a - \underline{A}_b\right)\right] \underline{\nabla} w_{ab} \cdot \underline{r}_{ab} \tag{2.46}$$

and it is an approximation of the following expression:

$$\underline{L}^E \left\{J_{A,b}, A_b\right\} \approx \underline{\mathrm{div}}\, J_A \left(\underline{\underline{\mathrm{grad}}}\, \underline{A} + \left(\underline{\underline{\mathrm{grad}}}\, \underline{A}\right)^T\right) \tag{2.47}$$

2.4 A variationally consistent SPH formulation

In this section, density computation strategies are first discussed. Afterwards, a standard one-fluid SPH formulation is derived following a Lagrangian variational approach introduced by Bonet and Lok [13]. It will be shown that the formula chosen to compute the density determines the choice of differential operators when building a conservative formulation.

2.4.1 Density

The classical definition of interpolated density used in SPH results from the discrete SPH interpolation (2.28) of the density field:

$$\rho_a = \sum_{b \in \mathcal{F}} V_b \rho_b w_{ab} \tag{2.48}$$

With $m_b = V_b \rho_b$ we obtain:

$$\rho_a = \sum_{b \in \mathcal{F}} m_b w_{ab} \tag{2.49}$$

This equation can be directly used to compute the density at each time-step. However it is not suitable for free-surface flows. Indeed, the kernel support being incomplete near the free-surface (*i.e.* there is a lack of particle above the free-surface), (2.49) leads to non-physical decrease of the density [36, 117]. Another solution is to solve the continuity equation using a SPH divergence operator:

$$\frac{d\rho_a}{dt} = -\rho_a \, D_a \left\{ \underline{u}_b \right\} \tag{2.50}$$

As a matter of fact, Vila [117] showed that equations (2.50) and (2.49) are tantamount when using the symmetric divergence operator (2.36), and considering time as a continuous variable, as demonstrated in the next section. However, because of interpolation and discretization errors, using the discrete continuity equation (2.50) can lead to inconsistency between the velocity and the density fields, as shown by Ferrand et al. [37]. Equation (2.49) is usually more robust especially regarding discontinuities of density. It is an antiderivative of the differential equation (2.50) and Vila [117] states that using (2.49) can be related to a kind of implicit time discretization. In order to use such a robust implicit discretization even for free-surface flows, Vila [117] proposes a third strategy. Differentiating the density interpolation expression (2.49) yields:

$$d\rho_a = d\left(\sum_{b \in \mathcal{F}} m_b w_{ab} \right) \tag{2.51}$$

Deriving with respect to time, we get:

$$\frac{d\rho_a}{dt} = \frac{d}{dt}\left(\sum_{b\in\mathcal{F}} m_b w_{ab}\right) \tag{2.52}$$

With an explicit time integration scheme, recalling that the particle mass is constant, we finally obtain:

$$\rho_a^{(n+1)} = \rho_a^{(n)} + \sum_{b\in\mathcal{F}} m_b \left(w_{ab}^{(n+1)} - w_{ab}^{(n)}\right) \tag{2.53}$$

where n denoted the current time-step index. With this form the density only depends on the particle positions, similarly to (2.49). It prevents systematic time integration errors and can also be used with free-surface flows. From a computational point of view, this technique may raise some practical issues. Contrary to (2.50), equation (2.53) requires first to compute the velocity and position for the time step $(n+1)$ before updating the density field. Consequently an additional loop over neighbouring particles is necessary. Besided that, it is also necessary to store the previous particle positions in order to evaluate the term $\left(w_{ab}^{n+1} - w_{ab}^{(n)}\right)$. Despite these technical difficulties, this method has proved to give much better results than using (2.50) (see Ferrand et al. [36, 37] for more details). Thus it will be used in all this work.

2.4.2 First order operators

Starting from the density definition (2.49), it is possible to derive the consistent SPH divergence operator (although it will not be used in our SPH computations, as stated above). To do so, let us restart from (2.52). The particle mass being constant, we can write:

$$\begin{aligned} d\rho_a &= \sum_{b\in\mathcal{F}} m_b\, dw\,(\underline{r}_a - \underline{r}_b) \\ &= \sum_{b\in\mathcal{F}} m_b\,(d\underline{r}_a - d\underline{r}_b)\cdot\underline{\nabla} w_{ab} \end{aligned} \tag{2.54}$$

Now, we can easily calculate the derivative of the density with respect to time in order to get the continuity equation.

$$\begin{aligned} \frac{d\rho_a}{dt} &= \sum_{b\in\mathcal{F}} m_b \left(\frac{d\underline{r}_a}{dt} - \frac{d\underline{r}_b}{dt}\right)\cdot\underline{\nabla} w_{ab} \\ &= \sum_{b\in\mathcal{F}} m_b\,(\underline{u}_a - \underline{u}_b)\cdot\underline{\nabla} w_{ab} \\ &= -\rho_a\left(-\frac{1}{\rho_a}\sum_{b\in\mathcal{F}} m_b(\underline{u}_a - \underline{u}_b)\cdot\underline{\nabla} w_{ab}\right) \end{aligned} \tag{2.55}$$

Then comparing equation (2.55) with the continuous form of the continuity equation (1.1) we can deduce the SPH divergence operator D consistent with the chosen SPH definition of density:

$$D_a\{\underline{u}_b\} = -\frac{1}{\rho_a}\sum_{b\in\mathcal{F}} m_b(\underline{u}_a - \underline{u}_b)\cdot\underline{\nabla} w_{ab} \tag{2.56}$$

which is (2.36) applied to the velocity field. Then, the variational principle of virtual work can be used to derive the gradient operator. For a particle system, the total variation of the internal energy Π reads:

$$d\Pi = \sum_{a\in\mathcal{F}} m_a\, d\pi_a \tag{2.57}$$

with $d\pi_a$ the variation of specific internal energy of particle a. For an isentropic flow, it can be written as [119]:

$$d\pi_a = \frac{p_a}{\rho_a^2}\, d\rho_a \tag{2.58}$$

This leads to:

$$d\Pi = \sum_{a\in\mathcal{F}} m_a \frac{p_a}{\rho_a^2}\, d\rho_a \tag{2.59}$$

Then the principle of virtual work states that, for an isolated system with no viscous forces, the variation of total internal energy $d\Pi$ due to the virtual displacement $d\underline{l}$ is compensated by the work of internal forces (*i.e.* the pressure forces):

$$d\Pi = \sum_{a\in\mathcal{F}} V_a \underline{G}_a\{p_b\}\cdot d\underline{l}_a \tag{2.60}$$

where $\underline{G}_a\{p_b\}$ denotes the SPH gradient operator consistent with the definition of density and the SPH divergence operator D. Combining Equation (2.54), (2.59) and (2.60) yields:

$$\sum_{a\in(\mathcal{F}\cup\mathcal{V})} V_a \underline{G}_a\{p_b\}\cdot d\underline{l}_a = \sum_{a\in\mathcal{F}} m_a \frac{p_a}{\rho_a^2}\sum_{b\in\mathcal{F}} m_b\,(d\underline{l}_a - d\underline{l}_b)\cdot\underline{\nabla} w_{ab} \tag{2.61}$$

Rearranging dummy subscripts we finally get the following gradient operator $\underline{G}$:

$$\underline{G}_a\{p_b\} = \rho_a \sum_{b\in\mathcal{F}} m_b \left(\frac{p_a}{\rho_a^2} + \frac{p_b}{\rho_b^2}\right)\underline{\nabla} w_{ab} \tag{2.62}$$

which is (2.33) applied to the pressure field. It is interesting to note that deriving a variationally consistent formulation from the particular definition of density (2.49) leads to a symmetric divergence operator and an anti-symmetric gradient operator, respectively based on equations (2.35) and (2.32) with $B = \rho$ and $k = 1$. In conclusion we found that a given definition of density leads to consistent divergence and gradient operators. In turn, this property stems from the fact that D and G are skew-adjoint operators, as pointed out by many authors, *e.g.* Violeau [119]. Thus the whole formulation is variationally consistent and guarantees conservation of energy, linear and angular momentum in the

absence of external forces. More details can be found in [13, 49].

2.4.3 Dissipative forces

In the scope of standard SPH formulations, only central forces between pairs of particles are considered, and force moments cannot be transmitted between them. The rotational degree of freedom of individual particles is indeed never considered. Violeau [118] showed that, consequently the dissipative forces must be collinear with the position vector $\underline{r}_{ab}$ to satisfy the angular momentum conservation. Therefore, Morris et al.'s [86] as well as Espanol and Revenga's [33] viscous terms do not conserve the angular momentum. In the case of Monaghan and Gingold's [84] viscous term, dissipative forces are collinear with $\underline{r}_{ab}$ and does conserve angular momentum. In addition, Colagrossi et al. [23] recently showed from a variational principle, that Monaghan and Gingold's [84] formula implicitly takes account of the bulk viscosity term in the Stokes's stress constitutive equation (1.15), with values of the bulk viscosity similar to those found for common fluids, such as water. On the contrary, the lack of conservation of the angular momentum in Morris et al.'s [86] formula makes it impossible to take the bulk viscosity into account. To restore the conservation of angular momentum in this case, the particles would have to admit a larger number of degrees of freedom, *e.g.* considering the intrinsic rotation of the particles.

2.5 Wall boundary conditions in SPH

We restrict our study to wall boundary treatment since WCSPH does require any free-surface boundary treatment. As for the open boundaries, the reader is referred to the recent literature, *i.e.* Leroy [65] or Ferrand et al. [38].

2.5.1 Classical treatment of the wall boundary conditions

One major issue in modelling fluid dynamics with SPH is that most problems involve solid walls whose treatment is not straightforward with Lagrangian methods. There are several wall boundary models for SPH in the literature [26, 37, 69, 82]. They can be grouped into four categories: the ghost particle approach, the repulsive force boundary conditions, the dynamic boundary conditions and the semi-analytical boundary conditions. The main principles of the first three approaches are briefly presented here while the last will be more detailed in Section 2.5.2.

The ghost particle approach was first introduced by Libersky et al. [69]. In this case, fictitious particles are added beyond the wall, symmetrically to the real particles, in a thin layer along the wall boundaries. To enforce a homogeneous Neumann boundary condition on a field A, the ghost particles must have the same value of A as their real twins. To

enforce a Dirichlet boundary condition, the ghost particle value of A is obtained through a linear extrapolation. For example, to enforce the no penetration condition at a motionless wall (1.29), the normal component of velocity of ghost particles must have the same magnitude as real particles and a reversed sign. This method provides a solid framework to implement boundary conditions but it can hardly be adapted for complex boundary shapes, especially in 3D. Moreover, it leads to a significant increase of the number of particles to be taken into account in the discrete summations.

In 1994, Monaghan [82] proposed the repulsive force boundary conditions model in which radial forces exerts between fluid and boundary particles. At each time-step, the forces must be calculated analytically after the Lennard-Jones potential used in molecular dynamics. This method is simple to implement, it has a low computational cost and can easily handle complex boundary shapes. As a disadvantage, with this method it is not possible to enforce explicitly Neumann or Dirichlet conditions, and provides irregular particle distribution and pressure profiles near solid walls.

A third model, so-called the dynamic boundary conditions, was introduced in 2001 by Dalrymple and Knio [26], while other authors used it after the name *fictitious particles*, see *e.g.* Ferrand et al. [37]. Rows of stationary particles are used to mimic the walls. Their velocity is imposed to the wall velocity although their position remains unchanged during the simulation. The density and pressure are calculated with the continuity and state equations, similarly to the fluid particles. This technique is also simple to implement even for relatively complex boundary shapes. But in this case too, it is not possible to enforce neither Dirichlet nor Neumann boundary conditions, and the particle number can grow significantly in 3D.

Summarizing, none of these methods is able to enforce proper boundary conditions for arbitrary boundary geometries. Thus in this work, a fourth approach, called the semi-analytical wall boundary conditions, is used and will be presented in the next section. This model has proved its efficiency in modelling laminar and turbulent flows involving complex boundary geometries within both Incompressible SPH and Weakly Compressible SPH frameworks [37, 42, 65, 67].

2.5.2 The Unified Semi-Analytical Wall boundary conditions

2.5.2.1 Continuous framework

The unified semi-analytical wall (USAW) boundary conditions model is based on a pioneering work by Kulasegaram et al. [63], then analyzed by several authors like Feldman and Bonet [35] or De Leffe et al. [27], and developed to the form used in this work by Ferrand et al. [37]. Considering a point close to the boundary $\partial\Omega$ of the domain Ω, the kernel support Ω_r intersects the domain boundary $\partial\Omega$ so the kernel average (2.8) is no

more equal to one. To compensate for the incomplete support, the kernel average is used for renormalizing the field interpolation (2.3). Thus we define a new field Γ as:

$$\Gamma(\underline{r}) = \int_{\Omega \cap \Omega_r} w(\underline{r} - \underline{r}')d\underline{r}' \tag{2.63}$$

Its spatial derivative reads:

$$\underline{\nabla}\Gamma(\underline{r}) = \oint_{\partial\Omega \cap \Omega_r} w(\underline{r} - \underline{r}')\underline{n}(\underline{r}')d\Sigma' \tag{2.64}$$

Using Γ to renormalize the continuous interpolation of the field A yields:

$$[A](\underline{r}) = \frac{1}{\Gamma(\underline{r})} \int_{\Omega_r} A(\underline{r}')w(\underline{r} - \underline{r}')d\underline{r}' \tag{2.65}$$

Far from the boundary, Γ is equal to one so the corrected interpolation (2.65) is identical to equation (2.3). Similarly to the analysis done in Section 2.2.2, we can see from equations (2.41) and (2.65) that renormalizing the interpolation restores the zeroth-order accuracy of the approximation near the wall. However, this correction does no longer make the kernel first moment be zero (*i.e.* the condition (2.9) is no longer verified) so the interpolation cannot be first-order accurate.

Furthermore, near the wall the first term in equation (2.21) does not vanish any more since it equals the right-hand side of (2.22). Indeed, the kernel support intersects the boundary of the domain so the boundary term is supposed to remain. Following Ferrand et al. [37], we will derive a set of discrete equations that lead to the variationally consistent formulation presented in Section 2.4 far from the boundary, and that take the renormalization correction into account near the walls.

We saw in Section 2.4 that the consistent gradient corresponds to the anti-symmetric operator (2.32) with $B = \rho$ and $k = 1$. Thus it derives from the following continuous expression:

$$\underline{\nabla}A = \rho\underline{\nabla}\left(\frac{A}{\rho}\right) + \frac{A}{\rho}\underline{\nabla}(\rho) \tag{2.66}$$

Substituting the spatial derivative of the right term by their continuous approximation (2.23) in the latter equation yields:

$$[\underline{\nabla}A](\underline{r}) = \rho\left[\underline{\nabla}\left(\frac{A}{\rho}\right)\right] + \frac{A}{\rho}[\underline{\nabla}(\rho)] \tag{2.67}$$

Using the first equation in (2.22) and rearranging we obtain:

$$[\underline{\nabla} A](\underline{r}) = \frac{1}{\Gamma}\int_{\Omega_r\cap\Omega}\left[\rho(\underline{r})\frac{A}{\rho}(\underline{r}\,') + \frac{A}{\rho}(\underline{r})\rho(\underline{r}\,')\right]\underline{\nabla}_r\, w(\underline{r}-\underline{r}\,')d\underline{r}\,' \\ -\frac{1}{\Gamma}\oint_{\Omega_r\cap\partial\Omega}\left[\rho(\underline{r})\frac{A}{\rho}(\underline{r}\,') + \frac{A}{\rho}(\underline{r})\rho(\underline{r}\,')\right] w(\underline{r}-\underline{r}\,')\underline{n}(\underline{r}\,')\Sigma' \quad (2.68)$$

where $d\Sigma'$ is a differential surface element of the boundary $\partial\Omega$ and $\underline{n}(\underline{r}\,')$ is the inward unit vector normal to $d\Sigma$. It is therefore necessary to derive the discrete approximation of Equation (2.68) so as to obtain the wall-renormalized SPH gradient operator. To do so, surface integrals have to be calculated so we first need to discretize the domain boundary.

2.5.2.2 Discrete framework

With the USAW boundary conditions, surface integrals over the domain boundary have to be evaluated in order to compute the boundary terms of the differential operator (2.68) and the gradient of Γ defined in equation (2.64). Thus the domain boundary has to be discretized. To do so, solid walls are meshed using a set of boundary elements ($\mathcal{S}$) being segments in two dimensions and triangles in three dimensions (see Figure 2.2a). Vertex SPH particles ($\mathcal{V}$) are placed at the vertices of the mesh. They are a part of the fluid but they move at wall velocity. As illustrated in Figure 2.2b, their mass m is calculated as a fraction θ of a reference mass denoted $\overline{m}_a$, *i.e.* $m = \theta\overline{m}_a$. In two dimensions, θ is defined as the angle between two connected segments, divided by 2π. Thus, for vertex particles we have $\theta_b \in]0;1[$. In order to have a general formulation, we also define $\theta_a = 1$ for free particles of fluid ($\mathcal{F}$) and $\theta_s = 1/2$ for boundary elements. In three dimensions, θ is calculated in a similar way using solid angles. For boundary elements and vertex particles, the density is obtained from a Shepard interpolation [103] of the density over the fluid particles, in order to compensate the incomplete kernel support near the walls [37]:

$$\forall a \in (\mathcal{V}\cup\mathcal{S}) \quad \rho_a = \frac{\sum\limits_{b\in\mathcal{F}} m_b w_{ab}}{\sum\limits_{b\in\mathcal{F}} V_b w_{ab}} \quad (2.69)$$

The gradient of Γ can be written as:

$$\underline{\nabla}\Gamma_a = \sum_{s\in\mathcal{S}}\left(\int w(\underline{r}-\underline{r}\,')d\Sigma'\underline{n}(\underline{r}\,')\right) = \sum_{s\in\mathcal{S}}\underline{\nabla}\Gamma_{as} \quad (2.70)$$

where $d\Sigma'$ is a differential surface element of the boundary $\partial\Omega$, $\underline{n}(\underline{r}\,')$ is the inward unit vector normal to $d\Sigma'$. $\underline{\nabla}\Gamma_{as}$ is the contribution of the segment s in the value of $\underline{\nabla}\Gamma_a$. It

is defined and approximated as follows:

$$\underline{\nabla}\Gamma_{as} = \int w(\underline{r} - \underline{r}')d\Sigma'\underline{n}(\underline{r}') \approx w_{as}\underline{n}_s\Sigma_s \tag{2.71}$$

with Σ_s the size (the length in 2D, the area in 3D) of the boundary element s. Ferrand et al. [37] also gives an analytical expression to calculate the gradient of Γ accurately for the Wendland kernel in 2D:

$$\begin{aligned}\underline{\nabla}\Gamma_{as} = &\frac{q_2\cos\alpha_2}{\pi}P(q_2) - \frac{q_1\cos\alpha_1}{\pi}P(q_1) + \frac{q_0^4}{\pi}\left(\frac{105}{64} + \frac{35}{512}q_0^2\right)\\ &\left[\text{sign}(q_2\cos\alpha_2)\ln\left(\frac{q_2 + |q_2\cos\alpha_2|}{|q_0|}\right) - \text{sign}(q_1\cos\alpha_1)\ln\left(\frac{q_1 + |q_1\cos\alpha_1|}{|q_0|}\right)\right]\end{aligned} \tag{2.72}$$

where

$$\begin{aligned}P(q) = &\frac{7}{129}q^5 - \frac{21}{64}q^4 + \frac{35}{32}q^3 - \frac{35}{24}q^2 + \frac{7}{4} +\\ &q_0^2\left(\frac{35}{768}q^3 - \frac{7}{16}q^2 + \frac{105}{64}q - \frac{35}{12}\right) + q_0^4\left(\frac{35}{512}q - \frac{7}{8}\right)\end{aligned} \tag{2.73}$$

with q_0 the normal dimensionless distance of particle a to the boundary element s, $(q_i)_{i\in\{1,2\}}$ the dimensionless distances between particle a and the two vertex (v_1, v_2) delimiting s, $(\alpha_i)_{i\in\{1,2\}}$ the angles between q_0 and q_i measured anti-clockwise. This geometrical parameters are illustrated in Figure 2.1.

Once the gradient of Γ is calculated, Ferrand et al. [37] showed that Γ can be calculated using the following governing equation:

$$\frac{d\Gamma_a}{dt} = \underline{\nabla}\Gamma_a \cdot (\underline{u}_a - \underline{u}_w) \tag{2.74}$$

with $\underline{u}_w$ the wall velocity. With this approach, Γ is obtained from a time-integration procedure so the gradient of Γ has to be calculated accurately in order to avoid the accumulation of numerical errors, hence the necessity of the analytical formula (2.72). Note that Leroy et al. [66] showed how to calculate Γ analytically without any governing equation in 2D. Mayrhofer et al. [76] then proposed a method to compute analytically the gradient of Γ in 3D, thus extending Ferrand et al.'s [37] method to three-dimensional geometries. Finally, Violeau et al. [121] provided an algorithm to compute both $\underline{\nabla}\Gamma$ and Γ analytically in 3D, but leading to cumbersome formulae, sometimes containing singularities. Recently, Chiron [21] proposed an alternative quadrature approach.

It now possible to discretize expression (2.68) to get the wall-renormalized SPH gradient

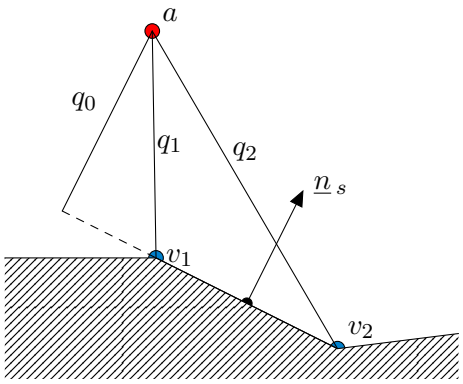

Figure 2.1: Illustration of geometrical parameters used to computed the gradient of Γ.

operator:

$$\underline{G}_a\{A_b\} = \frac{\rho_a}{\Gamma_a}\sum_{b\in(\mathcal{F}\cup\mathcal{V})} m_b\left(\frac{A_a}{\rho_a^2}+\frac{A_b}{\rho_b^2}\right)\underline{\nabla} w_{ab} - \frac{\rho_a}{\Gamma_a}\sum_{s\in\mathcal{S}}\left(\frac{A_a}{\rho_a^2}+\frac{A_s}{\rho_s^2}\right)\underline{\nabla}\Gamma_{as} \tag{2.75}$$

Similarly, the renormalized symmetric divergence operator is given by:

$$D_a\{\underline{A}_b\} = -\frac{1}{\rho_a\Gamma_a}\sum_{b\in(\mathcal{F}\cup\mathcal{V})} m_b\left(\underline{A}_a-\underline{A}_b\right)\cdot\underline{\nabla} w_{ab} - \frac{1}{\rho_a\Gamma_a}\sum_{s\in\mathcal{S}}\left(\underline{A}_a-\underline{A}_b\right)\cdot\underline{\nabla}\Gamma_{as} \tag{2.76}$$

Ferrand et al. [37] also extended the Morris et al.'s [86] second-order operator to this framework:

$$\underline{L}_a^M\{J_{A,b},\underline{A}_b\} = \frac{2}{\Gamma_a}\sum_{b\in(\mathcal{F}\cup\mathcal{V})} V_b\overline{J}_{A,ab}\frac{\underline{A}_a-\underline{A}_b}{r_{ab}^2}\underline{\nabla} w_{ab}\cdot\underline{r}_{ab} - \frac{1}{\Gamma_a}\sum_{s\in\mathcal{S}}\left(J_{A,a}\underline{\underline{\nabla}}\underline{A}_a + J_{A,s}\underline{\underline{\nabla}}\underline{A}_s\right)\cdot\underline{\nabla}\Gamma_{as} \tag{2.77}$$

We observe that the three above wall-modified SPH operators coincide with the original forms (2.33), (2.36) and (2.44) when the particle a is far away from any wall, *i.e.* $\Gamma_a = 1$ and no wall segments are connected with a. Note that with (2.77), ensuring a Neumann boundary condition is straightforward. Indeed, we see from (2.70) that the term $\underline{\nabla}\Gamma_{as}$ is oriented along the boundary normal vector. Thus $J_{A,s}\underline{\nabla}\underline{A}_s\cdot\underline{n}_s$ is the normal diffusive flux of A entering the domain. The boundary term in the Laplacian can then be used to extend Espanol and Revenga's [33] operator to USAW boundary conditions in a heuristic

way:

$$\underline{L}_a^E \{J_{A,b}, A_b\} = \frac{1}{\Gamma_a} \sum_{b \in \mathcal{F}} V_b \frac{\overline{J}_{A,ab}}{r_{ab}^2} \left[(d+2) \left((A_a - A_b) \cdot \underline{e}_{ab} \right) \underline{e}_{ab} + (\underline{A}_a - \underline{A}_b) \right] \nabla w_{ab} \cdot \underline{r}_{ab} - \frac{1}{\Gamma_a} \sum_{s \in \mathcal{S}} \left(J_{A,a} \underline{\underline{\nabla}} \underline{A}_a + J_{A,s} \underline{\underline{\nabla}} \underline{A}_s \right) \cdot \nabla \Gamma_{as} \quad (2.78)$$

Finally, the renormalization has also to be taken into account in the density computation. The density definition now reads:

$$\rho_a = \frac{1}{\Gamma_a} \sum_{b \in (\mathcal{F} \cup \mathcal{V})} m_b w_{ab} \quad (2.79)$$

Note that the sum extends to the fluid and vertex particles, contrary to (2.69). In order to use the implicit approach presented in Section 2.4.1, we can write in place of (2.51):

$$d\left(\Gamma_a \rho_a\right) = d\left(\sum_{b \in (\mathcal{F} \cup \mathcal{V})} m_b w_{ab} \right) \quad (2.80)$$

An explicit time-integration scheme finally yields:

$$\rho_a^{(n+1)} = \frac{1}{\Gamma_a^{(n+1)}} \left[\Gamma_a^{(n)} \rho_a^{(n)} + \sum_{b \in (\mathcal{F} \cup \mathcal{V})} m_b \left(w_{ab}^{(n+1)} - w_{ab}^{(n)} \right) \right] \quad (2.81)$$

generalizing (2.53).

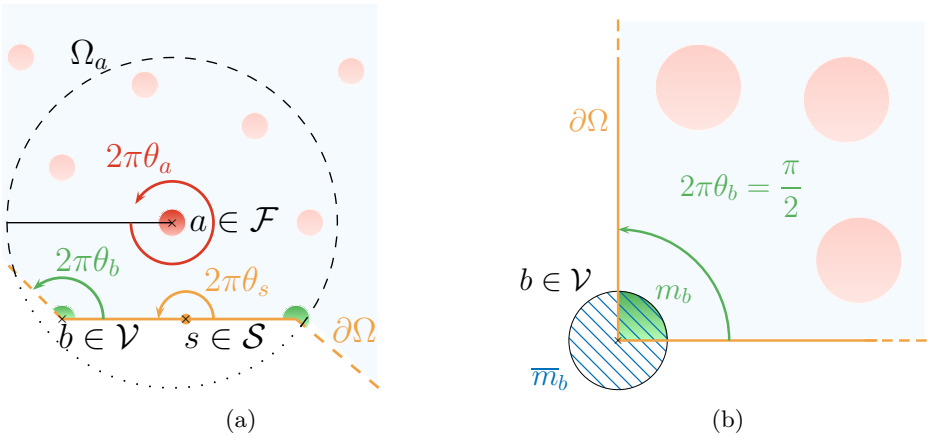

Figure 2.2: (a) Sketch of a boundary with: a vertex particle $b \in \mathcal{V}$, θ_v depends on the local shape of the boundary; a segment $s \in \mathcal{S}$ ($\theta_s = 1/2$); a fluid particle $a \in \mathcal{F}$ ($\theta_a = 1$). (b) Sketch of a vertex particle in a right-angled corner in 2-D, illustrating the relation between volume V_b, the dimensionless angle θ_b and the reference volume $\overline{V}_b$.

2.5.2.3 Enforcing wall boundary condition for fluids

Here we concentrate on fluids. Boundary conditions for elastic solids will be treated in Chapter 4.

Wall boundary condition on the velocity The condition on velocity (1.31) must now to be enforced in this framework. For laminar flows, this is done imposing the vertex velocity to the wall velocity (which may vary if the wall is that of a rigid body moving in the fluid):

$$\forall b \in \mathcal{V} \qquad \underline{u}_b = \underline{u}_w \tag{2.82}$$

and through the boundary part of the viscous term modelled with (2.77) or (2.78):

$$\underline{L}_a^{\text{bound}}\{\eta, \underline{u}_b\} = -\frac{1}{\Gamma_a}\sum_{s\in\mathcal{S}}\left(\left(\eta\,\underline{\underline{\nabla}}\,\underline{u}\right)_a + \left(\eta\,\underline{\underline{\nabla}}\,\underline{u}\right)_s\right)\cdot\underline{\nabla}\Gamma_{as} \tag{2.83}$$

Recalling that $\underline{\nabla}\Gamma_{as}$ is oriented along the inward normal vector $\underline{n}_s$ of the boundary element s, we can write:

$$\underline{L}_a^{\text{bound}}\{\eta, \underline{u}_b\} = -\frac{1}{\Gamma_a}\sum_{s\in\mathcal{S}}\left[\eta_a\left(\frac{\partial \underline{u}}{\partial \underline{n}}\right)_a + \eta_s\left(\frac{\partial \underline{u}}{\partial \underline{n}}\right)_s\right]|\underline{\nabla}\Gamma_{as}| \tag{2.84}$$

We now define a fictitious point a' such as:

$$\underline{r}_{a'} = \frac{\underline{r}_a + \underline{r}_s}{2} \tag{2.85}$$

and we make the following approximation:

$$\underline{L}_a^{\text{bound}}\{\eta, \underline{u}_b\} \approx -\frac{2}{\Gamma_a}\sum_{s\in\mathcal{S}}\eta_{a'}\left(\frac{\partial \underline{u}}{\partial \underline{n}}\right)_{a'}|\underline{\nabla}\Gamma_{as}| \tag{2.86}$$

Following Ferrand et al. [37], we use the fact that near a wall, the velocity is expected to be linear and tangential. Thus we can write:

$$\left(\frac{\partial \underline{u}}{\partial \underline{n}}\right)_{a'} \approx \frac{(\underline{u}_a - \underline{u}_s)\cdot\underline{t}_{as}}{\delta r_{as}}\,\underline{t}_{as} \tag{2.87}$$

with $\underline{t}_{as}$ the wall tangential vector:

$$\underline{t}_{as} = \frac{(\underline{u}_a - \underline{u}_s) - [(\underline{u}_a - \underline{u}_s)\cdot\underline{n}_s]\,\underline{n}_s}{|\,(\underline{u}_a - \underline{u}_s) - [(\underline{u}_a - \underline{u}_s)\cdot\underline{n}_s]\,\underline{n}_s|} \tag{2.88}$$

and:

$$\delta r_{as} = \max\left[(\underline{r}_a - \underline{r}_s)\cdot\underline{n}_s, \delta r\right] \tag{2.89}$$

where δr is the initial interparticle spacing. The above technique to impose a friction at the wall was tested successfully by Leroy [65], in the framework of Incompressible SPH, but proved valid for WCSPH by Ferrand et al. [37].

Wall boundary condition on the pressure As presented in Section 1.4.1, the dynamic condition on pressure can be approximated as:

$$\left.\frac{\partial p^*}{\partial \underline{n}_w}\right|_w = 0 \tag{2.90}$$

with p^* the dynamical pressure. Following Ferrand et al. [37], this condition is enforced calculating the pressure of vertex particles and boundary elements through a Shepard-like interpolation of the dynamic pressure field:

$$\forall a \in (\mathcal{V} \cup \mathcal{S}) \qquad p_a = \frac{\sum\limits_{b\in\mathcal{F}} V_b \left[p_b + (\underline{r}_a - \underline{r}_b)\cdot \underline{g}\right] w_{ab}}{\sum\limits_{b\in\mathcal{F}} V_b w_{ab}} \tag{2.91}$$

2.6 Chequerboard effects in WCSPH

A major drawback of the weakly compressible SPH method is that it suffers from spurious oscillations of the pressure and density fields. This question has been widely addressed in the SPH literature and several methods have been developed to circumvent this issue. In 2009, Ferrari et al. [39] proposed to add a diffusion term based on the Riemann invariants in the continuity equation. In 2010, Antuono et al. [6] presented the δ-SPH formulation. This model is based on a Euler solver with artificial viscosity, and a diffusive term in the continuity equations. In 2011, Fatehi and Manzari [34] identified the pressure oscillations to the chequerboard problem which is a well known issue in grid-based method. The authors state that the observed oscillatory state is a numerical, but not physical, solution of the discrete equations solved in SPH (zero-energy modes). This is due to the fact that in SPH all the field variables are stored at the particle positions: it is a collocated method. In grid-based methods, collocated approaches also suffer from the chequerboard problem. Though, different strategies can be adopted when having a mesh. For example, it can be decided to store the velocity at the center of the mesh cells, and to store the pressure at the vertices of the mesh. These techniques are referred to as non-collocated methods and they get rid of the chequerboard effect. For collocated grids, several methods have been developed and are now widely used in mesh-based numerical codes. Two of them were adapted to SPH and used in this work; they are presented below.

2.6.1 Brezzi and Pitkäranta's correction

In order to stabilize the numerical solution of the steady incompressible Navier-Stokes equations with collocated finite-elements methods, Brezzi and Pitkäranta [15] proposed to add a diffusive term in the continuity equation during the correction step of a projection method. It is interesting to note that Ferrari et al.'s [39] approach for SPH can be related to some kind of Brezzi and Pitkäranta's [15] correction, adapted to the weakly-compressible approach. Considering the time as a continuous variable, we saw in Section 2.4 that the discrete equation of continuity can be written as:

$$\frac{d\rho_a}{dt} = -\rho_a D_a\{\underline{u}_b\} \tag{2.92}$$

The pseudo-implicit scheme presented in Section 2.4.1 being used and neglecting viscous term, we can write:

$$\begin{aligned}
\frac{\rho_a^{(n+1)} - \rho_a^{(n)}}{\Delta t} &= -\rho_a^{(n)} D_a\left\{\underline{u}_b^{(n+1)}\right\} \\
&= -\rho_a^{(n)} D_a\left\{\underline{u}_b^{(n)} - \frac{\Delta t}{\rho_b^{(n)}}\underline{G}_b\left\{p_c^{(n)}\right\} + \Delta t\,\underline{g}\right\} \\
&= -\rho_a^{(n)}\left(D_a\left\{\underline{u}_b^{(n)}\right\} + \Delta t D_a\left\{\underline{G}_b\{p_c^{(n)}\}\right\} + \Delta t D_a\left\{\underline{G}_b\{\underline{g}\cdot\underline{r}_b^{(n)}\}\right\}\right)
\end{aligned} \tag{2.93}$$

where Δt is the time-step. From equation 2.93, we introduce a diffusion term Δ_{BP} defined as follows:

$$\Delta_{\mathrm{BP}}^{(n)} = -\rho_a^{(n)}\left(L_a^M\left\{\frac{\Delta t}{\rho_b^{(n)}}, p_b^{(n)}\right\} + L_a^M\left\{\Delta t, \underline{g}\cdot\underline{r}_b^{(n)}\right\}\right) \tag{2.94}$$

with L^M Morris' wall-renormalized Laplacian operator (2.77):

$$L_a^M\{J_{A,b}, A_b\} = \frac{2}{\Gamma_a}\sum_{b\in\mathcal{F}} V_b \overline{J}_{A,ab}\frac{A_a - A_b}{r_{ab}^2}\underline{\nabla} w_{ab}\cdot\underline{r}_{ab} \tag{2.95}$$

Note that the diffusion only occurs between fluid particles so there is no boundary term in the Laplacian and the sum only extends to the fluid particles. The additional term Δ_{BP} is similar but not exactly equal to the second term of Equation (2.93) since with the SPH operators, the Laplacian is not tantamount to the divergence of a gradient. Besides, equation (2.94) clearly shows that it vanishes when $\Delta t \to 0$.

2.6.2 Rhie and Chow correction

Equation (2.93) shows that the approximate Laplacian of pressure $D_a\{\underline{G_a}\{p_b^{(n)}\}\}$ is implicitly contained into the equation of continuity. Fatehi and Manzari [34], and more

recently Hashemi et al. [54], stated that substituting this discrete form of the Laplacian by another one can significantly reduce the pressure oscillation. This technique was first introduce for finite volumes by Rhie and Chow [101]. Thus, we will substitute two different discrete approximations of the Laplacian. The smoothing term is therefore supposed to tend to zero as the particle spacing δr decreases. Again, the diffusion only occurs between the fluid particles so the discrete operators do not have boundary terms and do not take the vertex particles into account. Several combinations of discrete Laplacian operators have been tested and finally we chose the following smoothing term:

$$\Delta_{\mathrm{RC}}^{(n)} = \rho_a^{(n)} \Delta t \left[L_a^M \left\{ \frac{1}{\rho_b^{(n)}},\, p_b^{(n)} \right\} - D_a^+ \left\{ \underline{G}_b^- \left\{ \frac{p_c^{(n)}}{\rho_b^{(n)}} \right\} \right\} \right] \tag{2.96}$$

with L^M the Morris et al.'s [86] operator (2.95), $\underline{G}^-$ the symmetric gradient derived from (2.36):

$$\underline{G}_a^- \{A_b\} = -\frac{1}{\rho_a} \sum_{b \in \mathcal{F}} m_b \left(A_a - A_b\right) \nabla w_{ab} \tag{2.97}$$

and D^+ the anti-symmetric divergence derived from (2.33):

$$D_a^+ \{\underline{A}_b\} = \rho_a \sum_{b \in \mathcal{F}} m_b \left(\frac{\underline{A}_a}{\rho_a^2} + \frac{\underline{A}_b}{\rho_b^2} \right) \cdot \nabla w_{ab} \tag{2.98}$$

The last two SPH operators have inverse symmetry properties with respect to the original ones used above. Note that, this particular combination was not chosen on a theoretical basis but after numerical tests.

2.6.3 Continuity equation correction

For both presented approaches, the continuity equation (2.81) is corrected as follows:

$$\rho_a^{(n+1)} = \frac{1}{\Gamma^{(n+1)}} \left[\Gamma^{(n)} \rho_a^{(n)} + \sum_{b \in (\mathcal{F} \cup \mathcal{V})} m_b \left(w_{ab}^{(n+1)} - w_{ab}^{(n)} \right) \right] + \Lambda \Delta^{(n)} \tag{2.99}$$

where Λ is a weighting coefficient and (Λ, Δ) can be either $(\Lambda_{\mathrm{BP}}, \Delta_{\mathrm{BP}})$ or $(\Lambda_{\mathrm{RC}}, \Delta_{\mathrm{RC}})$. From numerical experiments, the values

$$\Lambda_{\mathrm{BP}} = 0.1 \tag{2.100}$$

$$\Lambda_{\mathrm{RC}} = 1 \tag{2.101}$$

give satisfactory results.

2.7 Time integration

2.7.1 Explicit integration scheme

In this work, time integration is usually done with the full explicit symplectic method used by Ferrand et al. [36] that leads to the following scheme:

$$\begin{cases} \underline{u}_a^{(n+1)} = \underline{u}_a^{(n)} - \dfrac{\Delta t}{\rho_a^{(n)}} \underline{G}_a \left\{ p_b^{(n)} \right\} + \Delta t\, \underline{g} + \dfrac{\Delta t}{\rho_a^{(n)}} \underline{L}_a^M \{\eta_b, \underline{u}_b\} \\ \underline{r}_a^{(n+1)} = \underline{r}_a^{(n)} + \Delta t\, \underline{u}_a^{(n+1)} \\ \Gamma_a^{(n+1)} = \Gamma_a^{(n)} + \Delta t \left[(\underline{\nabla} \Gamma_a)^{(n+1)} \cdot \left(\underline{u}_a^{(n+1)} - \underline{u}_w^{(n+1)} \right) \right] \\ \rho_a^{(n+1)} = \Gamma^{(n+1)} \left[\Gamma^{(n)} \rho_a^{(n)} + \sum\limits_{b \in (\mathcal{F} \cup \mathcal{V})} m_b \left(w_{ab}^{(n+1)} - w_{ab}^{(n)} \right) \right] + \Lambda \Delta^{(n)} \end{cases} \tag{2.102}$$

Three restrictions on the time step must be enforced to ensure the numerical stability of this integration scheme. The first one relies the classical Courant-Friedrichs-Levy (CFL) number. The CFL number compares the time-step to the time for the information to travel the characteristic distance of the simulation (*i.e.* the discretization scale h) at the characteristic velocity of the problem. In WCSPH the CFL number is defined as:

$$C_{\text{CFL}} = \frac{c_0 \Delta t}{h} \tag{2.103}$$

For the viscous forces, an additional condition must be enforce through the following dimensionless number:

$$C_{\text{visc}} = \frac{\eta \Delta t}{\rho h^2} \tag{2.104}$$

This number expresses the fact that, the higher the viscosity, the faster the information propagate along the successive layers of the fluid. The governing equation of Γ requires an additional constraint. Indeed the time-step should decrease when a particle approaches the wall with a large velocity. Ferrand et al. [37] provide a criterion that takes this restriction into account:

$$C_\Gamma = \Delta t \max_{a \in \mathcal{F}} \left(\underline{\nabla} \Gamma_a \cdot (\underline{u}_a - \underline{u}_w) \right) \tag{2.105}$$

In conclusion, the numerical stability is ensured for:

$$\Delta t \leq \min \left(\frac{C_{\text{CFL}}\, h}{c_0}, \frac{C_{\text{visc}}\, \rho_0 h^2}{\eta}, \frac{C_\Gamma}{\max_{a \in \mathcal{F}} \left(\underline{\nabla} \Gamma_a \cdot (\underline{u}_a - \underline{u}_w) \right)} \right) \tag{2.106}$$

with the following empirical values:

$$\begin{aligned} C_{\text{CFL}} &= 0.4 \\ C_{\text{visc}} &= 0.125 \\ C_{\Gamma} &= 0.005 \end{aligned} \tag{2.107}$$

More details about the numerical stability of WCSPH can be found in Violeau and Leroy [120] and Hashemi et al. [54] (the latter for the effect of density smoothing).

2.7.2 Implicit viscous forces integration scheme

For cases in which viscosity is very large, the time-step restriction (2.104) can lead to unreasonably small time-step. To circumvent this issue, an implicit integration of the viscous term has been done in this work. Considering only viscous forces, we can write:

$$\frac{\underline{u}_a^{n+1} - \underline{u}_a^{n}}{dt} = \frac{1}{\rho_a} \underline{L}_a\{\eta_b, \underline{u}_b^{n+1}\} \tag{2.108}$$

We consider the Morris et al.'s [86] second order operator (2.77) that we denote $\underline{L}$ (instead of $\underline{L}^M$) for the sake of simplicity. Developing $\underline{L}_a\{\eta_b, \underline{u}_b^{n+1}\}$ in three sums over the free particles $\mathcal{F}$, the vertex particles $\mathcal{V}$ and the boundary elements $\mathcal{S}$ yields:

$$\begin{aligned} \underline{L}_a\{\eta_b, \underline{u}_b^{n+1}\} = &\frac{2}{\Gamma_a} \sum_{b \in \mathcal{F}} V_b \, \overline{\eta}_{ab} \, \frac{\underline{u}_a^{n+1} - \underline{u}_b^{n+1}}{r_{ab}^2} \underline{\nabla} w_{ab} \cdot \underline{r}_{ab} \\ &+ \frac{2}{\Gamma_a} \sum_{b \in \mathcal{V}} V_b \, \eta_a \, \frac{\underline{u}_a^{n+1} - \underline{u}_w}{r_{ab}^2} \underline{\nabla} w_{ab} \cdot \underline{r}_{ab} \\ &- \frac{1}{\Gamma_a} \sum_{s \in \mathcal{S}} \eta_a (\underline{\nabla} \underline{u}_a^{n} - \underline{\nabla} \underline{u}_w) \cdot \underline{\nabla} \Gamma_{as} \end{aligned} \tag{2.109}$$

where $\underline{u}_w$ is the imposed wall velocity. In equations (2.108) and (2.109), as well as later on in this sub-section, all the terms without time superscripts (like η_b, vr_{ab} and u_w) are considered at time n. Note that, to enforce the wall boundary condition according to the method presented in Section 2.5.2.3, *i.e* using equation (2.86), we choose to treat explicitly the boundary term $(\underline{\nabla} \underline{u}_a^{n} - \underline{\nabla} \underline{u}_w)$. Then we combine (2.108) and (2.109), moving the explicit terms to the right hand side:

$$\left[\underline{u}_a^{n+1} - \frac{2\Delta t}{\rho_a \Gamma_a} \sum_{b\in\mathcal{F}} V_b\, \overline{\eta}_{ab}\, \frac{\underline{u}_a^{n+1} - \underline{u}_b^{n+1}}{r_{ab}^2} \underline{\nabla} w_{ab} \cdot \underline{r}_{ab} - \frac{2\Delta t}{\rho_a \Gamma_a} \sum_{b\in\mathcal{V}} V_b\, \eta_a\, \frac{\underline{u}_a^{n+1}}{r_{ab}^2} \underline{\nabla} w_{ab} \cdot \underline{r}_{ab}\right] = \left[\underline{u}_a^{n} - \frac{2\Delta t}{\rho_a \Gamma_a} \sum_{b\in\mathcal{V}} V_b\, \eta_a\, \frac{\underline{u}_w}{r_{ab}^2} \underline{\nabla} w_{ab} \cdot \underline{r}_{ab} - \frac{\Delta t}{\rho_a \Gamma_a} \sum_{s\in\mathcal{S}} \eta_a (\underline{\nabla}\underline{u}_a^{n} - \underline{\nabla}\underline{u}_w) \cdot \underline{\nabla}\Gamma_{as}\right] \quad (2.110)$$

Thus, we obtain three linear systems. Denoting $\underline{U}_x$, $\underline{U}_y$ and $\underline{U}_z$ the vector containing respectively the x, y and z components of the velocity for all fluid particles at time $n+1$, we can write:

$$\begin{cases} \underline{\underline{M}}\,\underline{U}_x = \underline{B} \\ \underline{\underline{M}}\,\underline{U}_y = \underline{B} \\ \underline{\underline{M}}\,\underline{U}_z = \underline{B} \end{cases} \quad (2.111)$$

where $\underline{\underline{M}}$ is a sparse matrix of size $N \times N$ (N being the number of free-particles) with the following components (all terms being computed at time n, as explained above):

$$\begin{cases} M_{aa} = 1 - \dfrac{2\,\Delta t}{\rho_a \Gamma_a} \sum\limits_{b\in\mathcal{F}} V_b\, \overline{\eta}_{ab}\, \dfrac{\underline{\nabla} w_{ab} \cdot \underline{r}_{ab}}{r_{ab}^2} - \dfrac{2\,\Delta t}{\rho_a \Gamma_a} \sum\limits_{b\in\mathcal{V}} V_b\, \eta_a\, \dfrac{\underline{\nabla} w_{ab} \cdot \underline{r}_{ab}}{r_{ab}^2} \\ M_{ab} = \dfrac{2\,\Delta t}{\rho_a \Gamma_a} \sum\limits_{b\in\mathcal{F}} V_b\, \overline{\eta}_{ab}\, \dfrac{\underline{\nabla} w_{ab} \cdot \underline{r}_{ab}}{r_{ab}^2} \end{cases} \quad (2.112)$$

The components of the right-hand side $\underline{B}$ reads:

$$B_a = \underline{u}_a^{n} - \frac{\Delta t}{\rho_a \Gamma_a} \sum_{b\in\mathcal{V}} V_b\, 2\, \eta_a\, \frac{\underline{u}_w}{r_{ab}^2} \underline{\nabla} w_{ab} \cdot \underline{r}_{ab} - \frac{\Delta t}{\rho_a \Gamma_a} \sum_{s\in\mathcal{S}} \eta_a (\underline{\nabla}\underline{u}_a^{n} - \underline{\nabla}\underline{u}_w) \cdot \underline{\nabla}\Gamma_{as} \quad (2.113)$$

The system (2.111) is then solved using a non-preconditioned Bi-CGSTAB algorithm [115]. More detail about this solver can also be found in Leroy's [65] thesis. Note that implicit viscous forces has already been developped in SPH (without USAW boundary conditions though) by Peer et al. [95], and more recently by Zago et al. [127] in GPUSPH [1] for the simulation of lava flow, in the frame of dynamic boundary conditions [26].

Chapter 3

Multi-phase modelling with SPH

Ce chapitre a pour objet la modélisation des écoulements multiphasiques avec SPH. Une courte revue des modèles multiphasiques existant dans la littérature SPH est d'abord effectuée. Les modèles de Colagrossi et Landrini [22], Hu et Adams [58] et Grenier et al. [49] sont analysés et comparés. Le modèle de Hu and Adams [58] est finalement choisi pour ses bonnes propriétés, malgré son incapacité apparente à traiter les écoulements à surface libre. Deux améliorations du modèle sont alors proposées. Premièrement, une modification simple de l'équation de continuité rend possible l'utilisation du modèle dans le cas des écoulements à surface libre. Puis le modèle est adapté aux conditions aux limites semi-analytiques.

3.1 Existing SPH multi-phase models

As a reminder, in this work the term *multi-phase flows* refers to flows involving several immiscible materials. This designation is preferred to *multi-fluid* because various materials constitutive equations are used to describe the mechanical behaviour of the granular material. However, the present model is not a mixture model: SPH particles represent a small volume of one of the phases, and no mass transfer occurs between them.

The main difficulty in simulating multi-phase flows remains in the treatment of discontinuities across fluid interfaces. With SPH the density discontinuity raises particular issues [22, 49, 58]. Indeed, the classical SPH differential operators highly depend on the density of neighbouring particles. Consequently, numerical instabilities can occur near the interface for quite large density ratios. Moreover, computing the density through the classical SPH interpolation (2.49) leads to a numerical smoothing of the interface. This question has been widely addressed in the SPH literature and several strategies were proposed. In what follows, three different approaches are briefly presented and discussed.

3.1.1 Colagrossi and Landrini's formulation

Colagrossi and Landrini [22] recall that the gradient operator (2.62) usually used to compute the pressure gradient (*e.g.* [19, 65, 81]) can be derived from Equation (2.31) with $B = \rho$ and $k = 1$:

$$\underline{\nabla} p = \rho \underline{\nabla}\left(\frac{p}{\rho}\right) + \frac{p}{\rho}\underline{\nabla}\rho \tag{3.1}$$

Thus, the SPH gradient of pressure (2.62) implicitly involves a gradient of density. Then, at the interface of two fluids, this formula computes the derivative of a discontinuous field leading to severe numerical instabilities. To circumvent this issue, they suggest a formulation also based on the combination of a symmetric divergence and an anti-symmetric gradient operators, but they choose to take $k = 0$ in Equations (2.35) and (2.32). Thus the anti-symmetric gradient now derives from:

$$\underline{\nabla} p = \underline{\nabla} p + p\underline{\nabla}(1) \tag{3.2}$$

Here, no derivative of the density field is involved any more. With this approach they get the following SPH gradient of pressure:

$$\underline{G}_a\{p_b\} = \sum_{b\in\mathcal{F}} V_b(p_a + p_b)\underline{\nabla} w_{ab} \tag{3.3}$$

and the following continuity equation:

$$\frac{d\rho_a}{dt} = -\rho_a D_a\{\underline{u}_b\} \tag{3.4}$$

where D_a derives from the symmetric operator derived from (2.35):

$$D_a\{\underline{u}_b\} = -\sum_{b\in\mathcal{F}} V_b\,(\underline{u}_a - \underline{u}_b)\cdot\underline{\nabla} w_{ab} \tag{3.5}$$

This formulation is also variationally consistent, it preserves linear and angular momentum [13] and it has proved to prevent the numerical instabilities due to density discontinuities [22]. The computation of density is based on the divergence of velocity (2.50) so this model is able to handle free-surface flows. Nevertheless, as discussed in Section 2.4.1, the density field obtained integrating Equation 3.4 at each time-step leads to the accumulation of systematic integration errors [36]. Therefore, the density and velocity fields can become inconsistent. To circumvent this issue, we could try to obtain an implicit integrated form of the continuity equation. To do so, we write equation (3.4) substituting the divergence D_a by its expression:

$$\begin{aligned}\frac{d\rho_a}{dt} &= \rho_a \sum_{b\in\mathcal{F}} V_b(\underline{u}_a - \underline{u}_b)\cdot\underline{\nabla} w_{ab}\\ &= \frac{m_a}{V_a}\sum_{b\in\mathcal{F}} V_b(\frac{d\underline{r}_a}{dt} - \frac{d\underline{r}_b}{dt})\cdot\underline{\nabla} w(\underline{r}_a - \underline{r}_b)\\ &= \sum_{b\in\mathcal{F}} \frac{V_b}{V_a}\frac{d}{dt}\Big(m_a w_{ab}\Big)\end{aligned} \tag{3.6}$$

As the volume of particles is not constant, it is not possible to exactly integrate this equation similarly as Equation (2.53) so the pseudo-implicit approach presented in Section 2.4.1 cannot be adapted to this formulation. As a consequence, it requires a high order time-integration scheme in order to guarantee the consistency of the velocity and density fields.

3.1.2 Hu and Adams' model

Hu and Adams [58] noticed that using the classical density definition (2.49) in the vicinity of the interface between two fluids of different densities, leads to a numerical smoothing of the interface. This loss of information is a substantial drawback but it can be avoided since it is purely numerical. To circumvent this issue, they proposed a formulation based

on the interpolation of the inverse volume instead of density:

$$\left\langle \frac{1}{V} \right\rangle_a = \sum_{b \in \mathcal{F}} w_{ab} \tag{3.7}$$

In order to simplify notation, we will now refer to the particle volume as V_a defined by:

$$V_a = \left[\left\langle \frac{1}{V} \right\rangle_a \right]^{-1} \tag{3.8}$$

Thus the definition of density becomes:

$$\rho_a = \frac{m_a}{V_a} = m_a \sum_{b \in \mathcal{F}} w_{ab} \tag{3.9}$$

to be compared to (2.49). Therefore, within a given considered fluid, the mass m_a of a particle is constant and the variation of density is only due to the evolution of the spatial organisation of neighbouring particles. Thus, the interface smoothing is avoided.

Hu and Adams [58] then proposed a pressure gradient that can be derived from their density definition (3.9) and the Lagrangian variational principle of Virtual Work, as shown by Grenier et al. [49]:

$$\underline{G}_a \{p_b\} = \frac{1}{V_a} \sum_{b \in \mathcal{F}} \left(p_a V_a^2 + p_b V_b^2 \right) \underline{\nabla} w_{ab} \tag{3.10}$$

Note that the pressure gradient does not depend on density any more, and is consequently stable near the interface. It is interesting to notice that this operator could have been derived following Colagrossi and Landrini's [22] idea: given that the one-fluid gradient of pressure (2.62) instability is due to the gradient of density implicitly computed (see section 3.1.1), we could choose to derive the pressure gradient from Equation (2.32) with $B = 1/V$ and $k = 1$ since the volume is smooth across the interface:

$$\underline{\nabla} p = \frac{1}{V} \underline{\nabla} \left(pV \right) + pV \underline{\nabla} \left(\frac{1}{V} \right) \tag{3.11}$$

One can easily see that Hu and Adams' [58] gradient (3.9) derives from the latter equation. Finally, Hu and Adams [58] also proposed a modified viscous term so as to deal with multiple viscosities, ensuring the continuity of velocity and shear stress across the interface:

$$\underline{L}_a \{\eta_b, \underline{u}_b\} = n_a \sum_{b \in \mathcal{F}} \frac{2\eta_a \eta_b}{\eta_a + \eta_b} \left(V_a^2 + V_b^2 \right) \frac{\underline{u}_a - \underline{u}_b}{r_{ab}^2} \underline{\nabla} w_{ab} \cdot \underline{r}_{ab} \tag{3.12}$$

which has a similar structure as Morris et al.'s [86] second order operator with an additional term $(V_a^2 + V_b^2)$. Moreover, Hu and Adams [58] showed that choosing the harmonic mean

ensures the continuity of shear-stress across the interface.

As Equation (3.9) is used to compute the density, Hu and Adams' original formulation cannot be used with free-surface flows. However, the time-integrated form can easily be obtained thus making this formulation suitable for free-surface flows:

$$\rho_a^{(n+1)} = \rho_a^{(n)} + m_a \sum_{b\in\mathcal{F}} \left(w_{ab}^{(n+1)} - w_{ab}^{(n)}\right) \tag{3.13}$$

3.1.3 Grenier *et al*'s model

In Grenier et al.'s [49] model, the density is computed using a modified Shepard kernel denoted $w^{s,\chi}$ that reads:

$$w_{ab}^{s,\chi} = \frac{w_{ab}}{c_a} \quad \text{with} \quad c_a = \sum_{b\in\chi} V_b w_{ab} \tag{3.14}$$

where the sum is extended to particles b that belong to the same fluid as a denoted χ. The density is then defined as:

$$\rho_a = \sum_{b\in\chi} m_b w_{ab}^{s,\chi} \tag{3.15}$$

Note that the sum is again restricted to neighbours that belong to the same fluid as a. In this way, discontinuities of density at interface are naturally treated. It is interesting to note that the computation of the Shepard kernel $w_{ab}^{s,\chi}$ requires the volume of neighbours. These are obtained through their time evolution using a continuity equation. Contrary to (3.15), the classical Shepard kernel w_{ab}^{s} is used here:

$$w_{ab}^{s} = \frac{w_{ab}}{d_{ab}} \quad \text{with} \quad d_a = \sum_{b\in\mathcal{F}} V_b w_{ab} \tag{3.16}$$

The sums are now extended to all neighbouring particles, irrespective of the fluid they belong to. Then the continuity equation reads:

$$\frac{d\log(V/V^0)}{dt} = -\frac{1}{d_a} \sum_{b\in\mathcal{F}} \left(\underline{u}_a - \underline{u}_b\right) \underline{\nabla} w_{ab} \tag{3.17}$$

where V^0 is the initial volume of particles. This form of the continuity equation can be obtained using the symmetric divergence operator (Equation (2.35)) with $k = 0$ and the classical Shepard kernel (3.16). The variationally consistent gradient of pressure is then deduced with a similar method as presented in Section 2.4:

$$\underline{G}_a \{p_b\} = \sum_{b\in\mathcal{F}} V_b \left(\frac{p_b}{d_b} + \frac{p_a}{d_a}\right) \underline{\nabla} w_{ab} \tag{3.18}$$

Note that, from their definition (3.16), d_a and d_b are very close to 1. Following Hu and Adams [58], Grenier et al. [49] also proposed a new viscous term:

$$L_a\{\eta_b, \underline{u}_b\} = \frac{1}{V_a}\sum_{b\in\mathcal{F}} V_b \frac{2\eta_a\eta_b}{\eta_a+\eta_b}\Big(\frac{1}{d_a}+\frac{1}{d_b}\Big)\frac{\underline{A}_a - \underline{A}_b}{r_{ab}^2}\nabla w_{ab}\cdot\underline{r}_{ab} \tag{3.19}$$

Summarizing, the modified Shepard kernel and the density ρ_a are first evaluated using Equations (3.14) and (3.15). Afterwards, the particle volume V_a and the velocity are updated integrating the continuity equation (3.17) and the momentum equation written with Grenier et al.'s [49] operators (3.18) and (3.19).

It is important to remark that, contrary to the standard one-fluid SPH simulation and to Hu and Adams multi-phase formulation, it is not possible to derive the divergence operator from the density definition. Indeed, trying to differentiate Equation (3.15) we obtain:

$$d\rho_a = \sum_{b\in\mathcal{F}} m_b\, d\Big(\frac{w_{ab}}{\sum\limits_{b\in\mathcal{F}} V_b w_{ab}}\Big) \tag{3.20}$$

This definitely does not lead to Equation (3.17). Moreover, similarly to Colagrossi and Landrini [22], the density and the velocity fields can become inconsistent because of numerical errors resulting from computation of the divergence of velocity. Thus, this formulation also requires a high-order time-integration scheme (see *e.g.* Szewc [107]).

3.2 Present multi-phase formulation

3.2.1 Adaptation of USAW boundary conditions to multi-phase framework

In the present work, Hu and Adams' [58] multi-phase formulation has been chosen because it is a straightforward, robust and variationally consistent multi-phase model. Nevertheless, the main drawback of the original model was its inability to handle free-surface flows, but Equation (3.13) shows that this issue can be circumvented. However, a rigorous treatment of boundary conditions is necessary to make it capable of simulating flows presenting complex boundary geometries. Thus, we are now going to adapt this model to the USAW boundary conditions introduced in Section 2.5.

In the frame of multi-phase WCSPH, the particle density is determined by two factors. On the one hand, the particle mass depends on the fluid the particle belonging to χ and it remains constant during the whole simulation. On the other hand, the particle volume varies because of the weakly compressible assumption. In Hu and Adams' [58] model, these variations only depends on the neighbouring particle positions so the volume is a geometrical quantity that has nothing to do with the fluid the particle belongs to. It has

been seen in Section 2.5.2, that the mass and the density of vertex particles and boundary elements appear in the renormalized operators. Given that the boundary cannot belong to a particular fluid, it is thus necessary to redefine the USAW framework in terms of volumes.

For boundary elements and vertex particles, we introduce a reference volume $\overline{V}$ calculated from a Shepard interpolation of the inverse volume over fluid particles:

$$\forall a \in (\mathcal{V} \cup \mathcal{S}) \quad \overline{V}_a = \left[\frac{\sum\limits_{b \in \mathcal{F}} w_{ab}}{\sum\limits_{b \in \mathcal{F}} V_b w_{ab}} \right]^{-1} \tag{3.21}$$

The actual volume is then defined as a fraction θ of the reference volume. The volume fraction θ is defined as in Section 2.5.2. For fluid particles, the volume is equal to the reference volume ($\theta = 1$) and is obtained adapting (3.7) and (3.8) to the USAW framework:

$$\forall a \in \mathcal{F} \quad \overline{V}_a = \left[\frac{1}{\Gamma_a} \sum_{b \in (\mathcal{F} \cup \mathcal{V})} \theta_b w_{ab} \right]^{-1} \tag{3.22}$$

Thus, from (3.21) and (3.22), we see that the reference volume is not constant but only depends on the geometrical configuration of neighbouring particles around the point of interest, which in turn depends on the boundary shape. Vertex particles and boundary elements do not need to have a mass nor a density, but according to (3.21) they both have a volume.

3.2.2 Renormalization of Hu and Adams' formulation

Using the framework defined above, the density of fluid particles can be obtained from the definition $\rho = m/V$:

$$\forall a \in \mathcal{F} \quad \rho_a = \frac{m_a}{\Gamma_a} \sum_{b \in (\mathcal{F} \cup \mathcal{V})} \theta_b w_{ab} \tag{3.23}$$

However, (3.23) is not directly used to compute the density because it leads to non-physical decrease of density near the free-surface. Instead, following Vila's idea [117] we use:

$$\forall a \in \mathcal{F} \quad \frac{d\left(\Gamma_a \rho_a\right)}{dt} = \frac{d}{dt} \left(m_a \sum_{b \in (\mathcal{F} \cup \mathcal{V})} \theta_b w_{ab} \right) \tag{3.24}$$

Then, adapting the variationally consistent pressure gradient to USAW boundary condi-

tions, we get a new approximation of the pressure gradient:

$$\underline{G}_a\{p_b\} = \frac{1}{\Gamma_a \overline{V}_a} \sum_{b\in(\mathcal{F}\cup\mathcal{V})} \theta_b \left(p_a \overline{V}_a^2 + p_b \overline{V}_b^2\right) \underline{\nabla} w_{ab} - \frac{1}{\Gamma_a \overline{V}_a} \sum_{s\in\mathcal{S}} \frac{1}{\overline{V}_s} \left(p_a \overline{V}_a^2 + p_s \overline{V}_s^2\right) \underline{\nabla}\Gamma_{as} \quad (3.25)$$

Note that, in the absence of boundaries, (3.25) gives back Hu and Adams' original formula (3.10). Similarly, we define the consistent divergence operator for a vector field $\underline{A}$:

$$D_a\{\underline{A}_b\} = -\frac{\overline{V}_a}{\Gamma_a} \sum_{b\in(\mathcal{F}\cup\mathcal{V})} \theta_b \left(\underline{A}_a - \underline{A}_b\right)\cdot \underline{\nabla} w_{ab} + \frac{\overline{V}_a}{\Gamma_a} \sum_{s\in\mathcal{S}} \frac{1}{\overline{V}_s} \left(\underline{A}_a - \underline{A}_s\right)\cdot \underline{\nabla}\Gamma_{as} \quad (3.26)$$

Now we proceed the same way for the viscous term, paying particular attention to the viscosity of segments and vertex particles. Since we do not want to assign a type of fluid to boundaries, we take $\eta_b = \eta_a$ when $b \in (\mathcal{V}\cup\mathcal{S})$. First we adapt Hu and Adams' viscous term (3.12) to USAW boundary conditions:

$$\underline{L}_a^H\{\eta_b, \underline{u}_b\} = \frac{2}{\Gamma_a} \sum_{b\in(\mathcal{F}\cup\mathcal{V})} \theta_b \frac{\overline{V}_a^2 + \overline{V}_b^2}{\overline{V}_a} \frac{\eta_a\eta_b}{\eta_a+\eta_b} \frac{\underline{u}_a - \underline{u}_b}{r_{ab}^2} \underline{\nabla} w_{ab}\cdot \underline{r}_{ab} - \frac{1}{\Gamma_a} \sum_{s\in\mathcal{S}} \frac{\overline{V}_a^2 + \overline{V}_s^2}{\overline{V}_a \overline{V}_s} \left(\eta_a \underline{\underline{\nabla}}\,\underline{u}_a + \eta_s \underline{\underline{\nabla}}\,\underline{u}_s\right)\cdot \underline{\nabla}\Gamma_{as} \quad (3.27)$$

From now on, we will refer to it as *Hu and Adams' viscous term*. However, Morris et al.'s [86] viscous term adapted to USAW by Ferrand et al. [37] is also suitable for multi-phase. Indeed, in Section 2.3.3 it has been shown that this second order operator derives from Equation (2.32) with $k = 0$, which is the form chosen by Colagrossi and Landrini [22] to derive a multi-phase gradient:

$$\underline{\nabla} A = \underline{\nabla} A + A \underline{\nabla}(1) \quad (3.28)$$

This formula does not involve any density gradient so it can handle density discontinuities without exhibiting instabilities. Therefore, the USAW Morris et al.'s [86] viscous term (2.77) is already adapted to multi-phase flows. Expressing it in terms of reference volumes yields:

$$\underline{L}_a^M\{\eta_b, \underline{u}_b\} = \frac{2}{\Gamma_a} \sum_{b\in(\mathcal{F}\cup\mathcal{V})} \theta_b \overline{V}_b\, \overline{\eta}_{ab} \frac{\underline{u}_a - \underline{u}_b}{r_{ab}^2} \underline{\nabla} w_{ab}\cdot \underline{r}_{ab} - \frac{1}{\Gamma_a} \sum_{s\in\mathcal{S}} \left(\eta_a \underline{\underline{\nabla}}\,\underline{u}_a + \eta_s \underline{\underline{\nabla}}\,\underline{u}_s\right)\cdot \underline{\nabla}\Gamma_{as} \quad (3.29)$$

From now on, the above equation is referred to as *Morris' viscous term*. Note that, this viscous term also ensures continuity of velocity and shear stress across the interface if the harmonic viscosity mean is chosen:

$$\overline{\eta}_{ab} = \frac{2\eta_a\eta_b}{\eta_a + \eta_b} \tag{3.30}$$

With this choice, (3.27) and (3.29) differ only by the way the volumes are accounted for. Finally, Espanol and Revenga's [33] operator can also be written in terms of reference volumes. For any vector field $\underline{A}$ and any non-constant diffusion coefficient $J_{A,a}$, it reads:

$$\underline{L}_a^E \{J_{A,b}, \underline{A}_b\} = \frac{1}{\Gamma_a} \sum_{b\in\mathcal{F}} \theta_b \overline{V}_b \frac{\overline{J}_{A,ab}}{r_{ab}^2} \left[(d+2)\left((\underline{A}_a - \underline{A}_b)\cdot \underline{e}_{ab}\right)\underline{e}_{ab} + (\underline{A}_a - \underline{A}_b)\right] \underline{\nabla} w_{ab} \cdot \underline{r}_{ab} \\ - \frac{1}{\Gamma_a} \sum_{s\in\mathcal{S}} \left(J_{A,a}\, \underline{\underline{\nabla}}\, \underline{A}_a + J_{A,s}\, \underline{\underline{\nabla}}\, \underline{A}_s\right) \cdot \underline{\nabla} \Gamma_{as} \tag{3.31}$$

We can see that the volumes are accounted for in very similar way to (3.29). Furthermore, Espanol and Revenga's [33] operator does not depend on neighbour mass and density. As a consequence, it can also be used for multi-phase modelling.

3.2.3 Micro-mixing phenomenon

Contrary to mesh methods, due to its Lagrangian nature SPH naturally avoids diffusion of the interface. However, there is no mechanism that prevents the two fluids from mixing. To avoid micro-mixing, an additional term can be added in the Navier-Stokes momentum equation. Its role is to introduce a small repulsive force between phases, like an artificial surface tension force. Grenier et al. [49] proposed a formulation with explicit pressure dependency. On the other hand, Szewc [107] proposed another approach using Hu & Adams' [58] formulation that does not depends on pressure. Being inspired by the two previous approaches, we propose a formulation that uses Hu & Adams' formulation with explicit pressure dependency:

$$\Xi_a \{p_b\} = \frac{\epsilon}{V_a} \sum_{b\notin\chi(a)} \left(\mid p_a \mid V_a^2 + \mid p_b \mid V_b^2\right) \underline{\nabla} w_{ab}, \tag{3.32}$$

where ϵ is a dimensionless parameter used to tune the magnitude of this numerical force and $\chi(a)$ represents the phase the particle a belongs to. Thus, the sum is extended to particles that do not belong to $\chi(a)$ and this repulsive force increases approaching the interface. From numerical experiments, $\epsilon \in [0.005; 0.015]$ gives satisfactory results.

3.2.4 Time-integration scheme

Time integration is done with a fully explicit symplectic method [37] that leads to the following time-integration scheme:

$$\begin{cases} \underline{u}_a^{(n+1)} = \underline{u}_a^{(n)} - \dfrac{\Delta t}{\rho_a^{(n)}} \underline{G}_a \left\{ p_b^{(n)} \right\} + \Delta t\, \underline{g} + \dfrac{\Delta t}{\rho_a^{(n)}} \underline{L}_a \{ \eta_b, \underline{u}_b \} + \dfrac{\Delta t}{\rho_a^{(n)}} \Xi_a \left\{ p_b^{(n)} \right\} \\ \underline{r}_a^{(n+1)} = \underline{r}_a^{(n)} + \Delta t\, \underline{u}_a^{(n+1)} \\ \Gamma_a^{(n+1)} = \Gamma_a^{(n)} + \Delta t \left[(\underline{\nabla} \Gamma_a)^{(n+1)} \cdot \left(\underline{u}_a^{(n+1)} - \underline{u}_w^{(n+1)} \right) \right] \\ \rho_a^{(n+1)} = \Gamma^{(n+1)} \left[\Gamma^{(n)} \rho_a^{(n)} + \sum\limits_{b \in (\mathcal{F} \cup \mathcal{V})} m_b \left(w_{ab}^{(n+1)} - w_{ab}^{(n)} \right) \right] + \Lambda \Delta^{(n)} \end{cases} \tag{3.33}$$

where the pressure gradient $\underline{G}_a \{p_b\}$ is computed using (3.25):

$$\underline{G}_a \{p_b\} = \frac{1}{\Gamma_a \overline{V}_a} \sum_{b \in (\mathcal{F} \cup \mathcal{V})} \theta_b \left(p_a \overline{V}_a^2 + p_b \overline{V}_b^2 \right) \underline{\nabla} w_{ab} - \frac{1}{\Gamma_a \overline{V}_a} \sum_{s \in \mathcal{S}} \frac{1}{\overline{V}_s} \left(p_a \overline{V}_a^2 + p_s \overline{V}_s^2 \right) \underline{\nabla} \Gamma_{as} \tag{3.34}$$

and the viscous term is usually computed using Morris' viscous term (3.29) for the modelling of Newtonian fluids:

$$\underline{L}_a^M \{ \eta_b, \underline{u}_b \} = \frac{2}{\Gamma_a} \sum_{b \in (\mathcal{F} \cup \mathcal{V})} \theta_b \overline{V}_b \overline{\eta}_{ab} \frac{\underline{u}_a - \underline{u}_b}{r_{ab}^2} \underline{\nabla} w_{ab} \cdot \underline{r}_{ab} - \frac{1}{\Gamma_a} \sum_{s \in \mathcal{S}} \left(\eta_a \underline{\underline{\nabla}} \underline{u}_a + \eta_s \underline{\underline{\nabla}} \underline{u}_s \right) \cdot \underline{\nabla} \Gamma_{as} \tag{3.35}$$

The term $\Xi_a \{p_b\}$ refers to the additional force used to avoid micro-mixing (3.32) presented in Section 3.2.3. Finally, the term $\Lambda\Delta$ in the last equation corresponds to the chequerboard effect correction presented in Section 2.6.

Chapter 4

Granular flow modelling

Dans ce chapitre, les différents régimes de déformation des matériaux granulaires sont présentés. Les hypothèses dans le cadre desquelles ce travail s'inscrit sont également détaillées, et les limites du modèle développé dans ce contexte sont identifiées a priori. *Dans ce travail, le matériau granulaire est traité comme un milieu continu. Les milieux granulaires sont particulièrement complexes à modéliser car ils exhibent des comportements qui peuvent être assimilés à des états liquide, solide et même gazeux lorsque les conditions cinématiques et dynamiques évoluent. Avec une telle approche, la difficulté principale est donc de trouver une loi de comportement qui permette de reproduire le comportement physique des différents régimes de déformation et de capter correctement les transitions de régime. Une loi de comportemement est présentée pour chacun des deux régimes qu'on cherche à modéliser dans le cadre de cette thèse (solide et liquide rhéofluidifiant), et on propose un modèle de transition entre les deux régimes, fondé sur les propriétés physiques des matériaux granulaires.*

This chapter describes the constitutive equations used to model the granular material, as well as the boundary conditions at solid walls and interfaces with water. After presenting the governing equations, we present the corresponding SPH implementations.

4.1 Context

The behaviour of discrete particle assembly can depend on a number of different physical phenomenon. In order to avoid any confusion with the SPH particles, these discrete objects will be referred to as *grains* hereafter. In this work, we will focus on dry, or saturated, cohesionless granular materials. Thus we assume that the grain size is large enough so that the van der Waals forces, the electrostatic forces and the capillary forces can be neglected. Moreover the surrounding fluid viscosity is assumed to be low enough so that the viscous effects are also insignificant at the macroscopic scale. Therefore, the mechanical behaviour of the material is only controlled by the friction and the collisions between the grains.

Granular media are composed of grains whose statistical shape, size and spatial distribution affect the macroscopic behaviour of the assembly. Interactions between contiguous grains depend on their micromechanical properties but also on their arrangement, on the grain concentration and on the kinematic regime. When slow deformations occur within the medium, the quasi-static shear behaviour is described by non-linear, hysteretic, stress-strain curves that depend on stress level and on the way the shear stress changes when the normal stress varies, *i.e.* the stress path [113, 125]. In this regime, the medium is usually modelled as a solid using the plasticity theory [16, 17, 89, 102]. On the other hand, when the medium is so agitated that the grains interact by nearly instantaneous collisions, the granular material can be treated as a dissipative gas using specific kinetic theories [17, 44–46]. In between these two regimes, the time of free motion is of the order of magnitude of the contact time, thus the collisions can no longer be assumed instantaneous and the kinetic theories do not apply anymore. Instead, the granular medium can be described as a non-Newtonian liquid [17, 78, 97]. This regime is referred to as the dense granular flow regime. As a consequence, granular media exhibit a very complex response to mechanical loading, that can include all these behaviour at the same time in different locations [7, 60]. Within the scope of this thesis, we will only focus on the slow deformation and the dense granular flow regimes.

4.2 Modelling hypotheses

Theoretically, a granular flow is a multi-phase process: the material is composed of a collection of grains surrounded by a fluid (air or water). The fluid-solid interactions as well as the collisions and deformation processes can be modelled directly using the discrete

element method [25, 105, 112, 116]. This kind of approach may be very helpful to examine these processes and to improve the understanding of the macroscopic behaviour of the assembly. However, such an approach can only be considered at relatively small spatio-temporal scales and in no case can be applied to industrial problems. An alternative to this approach is the continuum hypothesis: the granular material is assumed to be a continuous medium. Thus we do not consider neither forces between the grains nor their individual displacement, but the stress field and the strain field within the continuous material. It should be noted that this approximation leads to a loss of degrees of freedom. Indeed, the rotation of individual grains, that can have a significant role in the mechanical behaviour of assemblies of spherical grains [91], can no longer be taken into account since force moments cannot be transmitted between surfaces within the continuum [125]. Nevertheless, this is a mandatory simplification in the scope of industrial applications.

Under the continuum assumption, the continuous medium represents a mixture of grains and air, or grains and water. Therefore, we need to define equivalent properties of the continuous material from the physical properties of the granular material component. Let us first define the local fluid volume fraction ϕ in a small control volume V_{mix} within the mixture, centred in $\underline{r}$:

$$\phi(\underline{r}\,,t) = \frac{1}{V_{\text{mix}}(\underline{r}\,)} \int_{V_{\text{mix}}(\underline{r}\,)} \mathbb{1}_w(\underline{r}\,',t) d\underline{r}\,' \tag{4.1}$$

where $\mathbb{1}_w(\underline{r}\,,t)$ is the fluid indicator function:

$$\mathbb{1}_w(\underline{r}\,,t) = \begin{cases} 1 & \text{if} \quad \underline{r} \in \text{fluid} \\ 0 & \text{if} \quad \underline{r} \notin \text{fluid} \end{cases} \tag{4.2}$$

The quantity ϕ also corresponds to the porosity of the material, while $(1-\phi)$ is usually referred to as the grain concentration. Then, we can define the equivalent density ρ_{eq} from the grain density ρ_{g} and the fluid density ρ_{f}:

$$\rho_{\text{eq}}(\underline{r}\,,t) = \left[1-\phi\left(\underline{r}\,,t\right)\right] \rho_{\text{g}}\left(\underline{r}\,,t\right) + \phi\left(\underline{r}\,,t\right) \rho_{\text{f}}\left(\underline{r}\,,t\right) \tag{4.3}$$

However the continuum hypothesis presents a major difficulty within the framework of the SPH formulations presented in Chapter 2 and 3. Physically, the evolution of grain concentration results from differences of velocity between the solid phase and the liquid phase. When the mixture is assumed to be continuous, the concentration evolution must be taken into account through the transport of a concentration field. However, this is not straightforward in the framework of SPH because this implies mass transfers between SPH particles. The particle masses being no longer constant, the SPH formulations presented in Chapters 2 and 3 are not valid anymore and a whole new SPH formulation would be necessary. Such a model is beyond the scope of this thesis. Thus, although it has

be shown that the grain concentration is an important parameter for the description of dense granular flows [7, 78], the grain concentration will be assumed to be constant and homogeneous within the mixture domain. Therefore, in practise, ϕ is simply the porosity of the granular material at initial time.

In addition, the fluid surrounding the grains will be assumed to be at rest with respect to the granular material skeleton. Indeed solving the fluid flow through the porous medium raises many practical issues, in particular at water-mixture interfaces. For example, let us consider an outgoing water flow from the mixture phase to the water phase. Then the mixture SPH particles should give some water mass up to the water SPH particles in order to ensure the mass conservation. Again, this would require variable SPH particle mass. Ulrich [114] proposed a simplified model of partly saturated soil, solving the flow in the porous material and transporting a concentration field. However, with this model, the mass of water is not conserved. Consequently, in his work the water flow through the porous medium is also neglected and the interstitial water is assumed to move at the mixture velocity. This simplification implies several disadvantages. First, the seepage cannot be taken into account while it can have a significant effect when a stable structure of dry granular material becomes partially saturated [70]. Thus in this work, we will only consider cases in which the material is initially totally dry (denoted by $^{\text{dry}}$) or fully saturated (denoted by $^{\text{sat}}$), and remains that way. For the dry case, the mass of air in the pore is neglected so the equivalent density (4.3) finally simplifies as:

$$\begin{cases} \rho_{\text{eq}}^{\text{dry}}(\underline{r}\,,t) &= (1-\phi)\ \rho_{\text{g}}(\underline{r}\,,t) \\ \rho_{\text{eq}}^{\text{sat}}(\underline{r}\,,t) &= (1-\phi)\ \rho_{\text{g}} + \phi\,\rho_{\text{w}}(\underline{r}\,,t) \end{cases} \tag{4.4}$$

with ρ_{w} the density of water. Secondly, neglecting the flow through the porous material also implies that the pore water pressure field is unknown. Therefore, another approximation is necessary and the pore water pressure will be assumed to be hydrostatic.

To summarize, the following assumptions are made in this work:

1. The granular material is assumed to be a continuous medium
2. The grain concentration is constant in space and time, thus the granular material porosity is constant
3. The fluid surrounding the grains is at rest with respect to the granular material skeleton. More precisely:
   (a) there is no fluid flow through the porous medium and thus no seepage
   (b) the granular material is either dry or fully saturated with water
   (c) the pore water pressure is hydrostatic

4.3 Modelling strategies

4.3.1 The viscoplastic approach

As mentioned in Section 4.1, this work is focused on the states of granular materials ranging from the solid state to liquid state. When a granular medium exhibits its solid state, the stability of the assembly is ensured by the friction between individual grains. Thus the strength of the system is limited by the loads that the frictional bounds can sustain. Once this strength is exceeded, the system fails. The solid particles form blocks of many particles, that move relative to one another in shear bands. If the deformations remain slow, the frictional contact time is large compared to the free time: this is the quasi-static regime. On the other hand, if deformations do not remain slow, the grains receive enough energy to leave their block and move individually. The slip regions propagate until the whole material flows: this is the dense granular flow regime [17, 45, 78, 113].

For problems in which these materials can behave either as elastic solids or as fluids, a rheological approach is often adopted. In particular, granular materials are usually treated as viscoplastic fluids. Viscoplasticity is characterized by a yield stress τ_y under which no deformation occurs. When the yield stress is exceeded, the material starts to flow. In such a model, the yield stress has to be compared to an invariant measure of the stress configuration denoted τ (see Section 4.4 for a detailed presentation of the yield criteria). A full review of viscoplastic models can be found in [8, 79]. Viscoplastic models include Herschel-Bulkley's and Casson's ones, but the most common and best-known model was proposed by Bingham [11] and reads:

$$\begin{cases} \underline{\underline{\dot{\gamma}}} = \underline{\underline{0}} & \text{if} \quad \tau \leq \tau_y \\ \underline{\underline{\dot{\gamma}}} = \left[2\left(\eta_\infty + \dfrac{\tau_y}{\dot{\gamma}}\right)\right]^{-1} \underline{\underline{\tau}} & \text{if} \quad \tau > \tau_y \end{cases} \tag{4.5}$$

where η_∞ is the plastic dynamic viscosity, $\underline{\underline{\dot{\gamma}}}$ the strain rate tensor (defined in Section 1.2.2.1) and $\dot{\gamma}$ the strain rate magnitude defined from the second invariant of $\underline{\underline{\dot{\gamma}}}$ as:

$$\dot{\gamma} = \sqrt{2\,\underline{\underline{\dot{\gamma}}} : \underline{\underline{\dot{\gamma}}}} \tag{4.6}$$

In this model, the yield criterion is based on the second invariant (1.11) of the shear-stress tensor $\underline{\underline{\tau}}$, according to the von Mises criterion of plasticity theory [8]:

$$\tau = \sqrt{J_2} = \sqrt{\frac{1}{2}\,\underline{\underline{\tau}} : \underline{\underline{\tau}}} \tag{4.7}$$

The ideal Bingham model (4.5) describes a material that behaves as a rigid body at low stresses and flows as a fluid when the yield stress is exceeded. Unfortunately, ideal Bing-

ham's model, as well as Herschel-Bulkley's and Casson's ones, all involve discontinuous constitutive equation that corresponds to the liquid-solid phase change. They are thus poorly adapted to numerical simulation because they require additional numerical procedures to track down yielded/unyielded regions. Indeed, it can be easily verified that the transitions between liquid and solid states are not included in the model. To do so, let us calculate τ applying (4.7) to the second equation in (4.5), which corresponds to the liquid state:

$$\tau = \eta_\infty \dot{\gamma} + \tau_y \quad \xrightarrow{\dot{\gamma}\to 0} \tau_y \tag{4.8}$$

We can see that when the strain rate vanishes, the deviatoric stress decreases and tends to τ_y but never goes below. Consequently, it is necessary to identify beforehand the rigid cores within the material, detecting the zero shear rate regions. But because of numerical noise, some shear rate may be artificially produced, which would make such a detection quite difficult [92]. Moreover, Bingham's model does not provide any expression to calculate the stresses in the rigid regions. To circumvent this issue, these models can be approximated assuming that the viscoplastic material is a fluid that exhibits infinitely high viscosity when the strain rate vanishes. Thus the material is always liquid but mimics the ideal models behaviour for all rates of deformation. Numerically, this is achieved using shear thinning rheological law and limiting the viscosity to a huge but finite maximum value. Such an approach was first introduced by Tanner and Milthorpe [110] who proposed a bi-viscosity model that regularized the ideal Bingham model:

$$\underline{\underline{\tau}} = 2\,\eta_{\text{eff}}\,\underline{\underline{\dot{\gamma}}} \quad \text{with} \quad \eta_{\text{eff}} = \begin{cases} \eta_0 & \text{if} \quad \dot{\gamma} \le \dot{\gamma}_y \\ \eta_\infty + \dfrac{\tau_y}{\dot{\gamma}} & \text{if} \quad \dot{\gamma} > \dot{\gamma}_y \end{cases} \tag{4.9}$$

where η_0 is the dynamic viscosity in unyielded regions, $\dot{\gamma}_y$ is the yield strain rate for which failure occurs and $\dot{\gamma}$ is the mean scalar rate of strain defined in (4.6). With such a model, the yield criterion is not based on a dynamic condition anymore ($\tau > \tau_y$), but on a kinematic condition ($\dot{\gamma} > \dot{\gamma}_y$). Calculating the second invariant of the deviatoric stress tensor from (4.9) yields:

$$\tau = \eta_{\text{eff}}\,\dot{\gamma} \tag{4.10}$$

Hence the relation relating the yield strain rate to the yield stress:

$$\tau_y = \tau(\dot{\gamma}_y) \quad \Rightarrow \quad \dot{\gamma}_y = \frac{\tau_y}{\eta_0} \tag{4.11}$$

Note that, contrary to the plastic viscosity η_∞ which is a physical parameter that can be determined experimentally, the dynamic viscosity η_0 is a numerical parameter that has to be smartly chosen. On the one hand, η_0 has to be large enough to guarantee that no significant motion occurs in unyielded regions. On the other hand, a too large value

can raise numerical stability issues. The main advantage of Tanner and Milthorpe's [110] bi-viscosity model is that it is smoother than the ideal Bingham model, even though it is not continuous:

$$\begin{cases} \eta_{\text{eff}}(\dot{\gamma}_{\text{y}}) & = \eta_0 \\ \lim\limits_{\substack{\dot{\gamma}\to\dot{\gamma}_{\text{y}} \\ \dot{\gamma}>\dot{\gamma}_{\text{y}}}} \eta_{\text{eff}} & = \eta_\infty + \eta_0 \end{cases} \quad \Rightarrow \quad \lim_{\substack{\dot{\gamma}\to\dot{\gamma}_{\text{y}} \\ \dot{\gamma}>\dot{\gamma}_{\text{y}}}} \eta_{\text{eff}} \neq \eta_{\text{eff}}(\dot{\gamma}_{\text{y}}) \tag{4.12}$$

An alternative to the bi-viscosity model is Papanastasiou's [94] exponential regularization of the ideal Bingham model (4.5):

$$\eta_{\text{eff}} = \eta_\infty + \frac{\tau_{\text{y}}}{\dot{\gamma}} \left(1 - \exp\left(-m^{\text{p}}\dot{\gamma}\right)\right) \tag{4.13}$$

where m^{p} is a numerical parameter that controls the growth of stress. It has to be large enough so that (4.13) mimics the ideal Bingham model in yielded regions:

$$\lim_{m^{\text{p}}\to+\infty} \eta_{\text{eff}} = \eta_\infty + \frac{\tau_{\text{y}}}{\dot{\gamma}} \tag{4.14}$$

However, m also determines the maximum viscosity in unyielded regions:

$$\lim_{\dot{\gamma}\to 0} \eta_{\text{eff}} = \eta_\infty + \tau_{\text{y}} m^{\text{p}} \tag{4.15}$$

There are alternatives to the viscoplastic models presented above. Jop et al. [62] proposed a viscoplastic model dedicated to the granular flow modelling. It is based on a frictional rheological law, *i.e.* the effective viscosity is related to the solid friction between the grains constituting the material. This model is referred to as $\mu(I)$ rheology, and was successfully applied to the modelling of intense bed load transport regime by Revil-Baudard and Chauchat [100]. The parameter μ is a friction coefficient that depends on the dimensionless inertial number I, defined as the ratio of a deformation time scale t_d and an inertial time scale t_i:

$$I = \frac{t_{\text{d}}}{t_{\text{i}}} \tag{4.16}$$

where the deformation time scale t_{d} is defined by:

$$t_{\text{d}} = \frac{1}{\dot{\gamma}} \tag{4.17}$$

The inertial time scale is the time where a grain of sediment will fall over its own diameter d_{g} when it is submitted to a given pressure p. For free fall, viscous and turbulent regimes,

the authors define three respective inertial time scales:

$$t_{\mathrm{i}}^{\mathrm{ff}} = d_{\mathrm{g}}\sqrt{\frac{\rho_{\mathrm{g}}}{p}}, \qquad t_{\mathrm{i}}^{\mathrm{v}} = \frac{\eta_{\mathrm{w}}}{p}, \qquad t_{\mathrm{i}}^{\mathrm{t}} = d_{\mathrm{g}}\sqrt{\frac{\rho_{\mathrm{w}} C_{\mathrm{D}}}{p}} \tag{4.18}$$

with ρ_{w} and η_{w} the density and dynamic viscosity of water, C_{D} the drag coefficient of the grains and d_{g} the grain diameter. The inertial number I is calculated from (4.16) using the largest inertial time scale:

$$t_{\mathrm{i}} = \max\left(t_{\mathrm{i}}^{\mathrm{ff}},\, t_{\mathrm{i}}^{\mathrm{v}},\, t_{\mathrm{i}}^{\mathrm{t}}\right) \tag{4.19}$$

The friction coefficient μ is then defined by:

$$\mu(I) = \mu_1 + \frac{\mu_2 - \mu_1}{\dfrac{I_0}{I} + 1} \tag{4.20}$$

where I_0 is an empirical constant of the model, while μ_1 and μ_2 represent two dynamic friction coefficients that must be determined experimentally for every material. In the granular material, the viscous fluid constitutive equation (1.15) presented in Section 1.2.2.1 is used, so the shear stress tensor reads:

$$\underline{\underline{\tau}} = 2\,\eta_{\mathrm{eff}}\,\underline{\underline{\dot{\gamma}}}, \qquad \text{with} \quad \eta_{\mathrm{eff}}^{\mu(I)} = \frac{\mu(I)\,p}{\dot{\gamma}} \tag{4.21}$$

Note that the numerator in the effective viscosity expression $\mu(I)\,p$ can be related to the Coulomb friction law that will presented in Section 4.4.1, which is why this model is referred to as a frictional rheology. It should be noted that the effective viscosity diverges when the strain rate vanishes, hence the regularization proposed by Chauchat and Médale [20]:

$$\eta_{\mathrm{eff}}^{\mu(I)} = \frac{\mu(I)\,p}{\dot{\gamma} + m^{\mu(I)}} \tag{4.22}$$

where $m^{\mu(I)}$ is the regularization parameter that determines the maximum viscosity in unyielded regions:

$$\lim_{\dot{\gamma}\to 0} \eta_{\mathrm{eff}} = \frac{\mu(I)\,p}{m^{\mu(I)}} \tag{4.23}$$

Therefore, similarly to Tanner and Milthorpe's [110] bi-viscosity model, the Papanastasiou's [94] model and $\mu(I)$ rheology also depend on a numerical parameter that affects both the solid-liquid transition, and the solid-like behaviour. However, using regularized viscoplastic models is straightforward and this method has been widely applied to the simulation of sediment transport with the Finite Volumes [85], Moving Particle Semi-implicit [87] and Smoothed Particle Hydrodynamics [19] methods.

To summarize, regarding sediment transport modelling, the viscoplastic approach is well

adapted for highly dynamic scenarios but may exhibit severe drawbacks regarding small strain-rates and deformations. Indeed, according to Beverly and Tanner [10], "if stresses are everywhere very low compared to τ_y, then misleading velocity fields can result from the biviscosity model". In other words, in low stresses regions, the regularized viscoplastic models only mimics the rigid body behaviour. The residual velocity fields (*i.e.* appart from the rigid body velocity) resulting from this model have no physical signification, and they should tend to zero as the maximum viscosity (η_0 for the bi-viscosity model) increases. As regards erosion and scour development, a proper treatment of motionless regions is essential to correctly estimate the bed evolution. Thus, it is necessary to ensure that results do not depend on the chosen maximum viscosity. But in practice, the maximum value of viscosity is actually limited for explicit time integration schemes, because of computational cost.

4.3.2 Present approach

In order to circumvent the issues raised by the viscoplastic approach, a different approach is proposed. Ulrich's [114] elastic-viscoplastic model is implemented and improved in order to model the solid, quasi-static and granular flow regimes. Thus, an elastic solid model is used to model the solid state and a shear-thinning fluid model is used to model the dense granular flow regime. The quasi-static regime then corresponds to solid blocs sliding on each other by means of fluidized layers of granular material. Similarly to the regularized viscoplastic model, Ulrich's [114] failure condition is based on a kinematic condition ($\dot{\gamma} > \dot{\gamma}_y$) and the yield shear rate $\dot{\gamma}_y$ is related to the yield stress τ_y through a numerical viscosity parameter. However, in this work we propose to build a yield viscosity η_y from the physical properties of the granular material so that the solid-liquid transition does not depend on a free numerical parameter anymore. A continuous transition between the two states is ensured by a blending function driven by the strain rate magnitude. The yield stress is obtained according to the Drucker-Prager yield criterion that is presented in the next section.

4.4 Yield criterion

As discussed in the previous section, material failure plays a key role in the modelling of granular flows because it largely affects the regime transitions. In the continuum, the failure is determined by the local stress conditions. Besides determining the regime transition, most of the rheological laws used to model the dense granular flow regime, also depend on the yield criterion, as explained above. There are many yield criteria that are adapted to the different kinds of materials. To give a general formulation of yield criteria, we can assume that the failure occurs when a particular combination of the stress

components reaches a critical value denoted K:

$$F(\sigma_{xx}, \sigma_{xy}, \sigma_{xz}, \sigma_{yy}, \sigma_{yz}, \sigma_{zz}) = K \tag{4.24}$$

Considering isotropic material, this function only depends on the principal stresses[1]:

$$F(\sigma_1, \sigma_2, \sigma_3) = K \tag{4.25}$$

A convenient alternative is to express the yield criterion in terms of stress invariants I_1, J_2 and J_3 defined in Section 1.2.1:

$$F(I_1, J_2, J_3) = K \tag{4.26}$$

In soil mechanics, Mohr-Coulomb's and Drucker-Prager's yield criteria are the most commonly used and will be presented in the following sections.

4.4.1 Mohr-Coulomb

Mohr-Coulomb's yield criterion is based on the 2D Couloumb's [24] friction equation, that gives the shear stress critical magnitude, where the failure occurs for a given compressive (normal) stress $\underline{\sigma}_N$ acting on a plane of normal $\underline{n}$. The critical shear stress can be achieved in any tangential directions of the plane, thus denoting σ_S the shear stress, the failure occurs when:

$$|\sigma_S| = -\sigma_N \tan\psi + c \tag{4.27}$$

where ψ is the internal friction angle, c is the cohesion and $\underline{\sigma}_N = \sigma_N \underline{n}$. Mohr-Coulomb's failure criterion states that the larger the compressive stress, the more shear the material can sustain. Note that, here again, the classical continuum mechanics sign convention is adopted so outward normals are used. Consequently, for a compressive stress, σ_N is negative, hence the minus sign in the right-hand side of the latter equation.

To extend Mohr-Coulomb's criterion (4.27) to a 3D continuum, we need to evaluate the normal stress and the shear stress acting on any surface within the continuum. Let us take some surface of normal $\underline{n} = \sum_{i\in\{1..3\}} n_i \underline{e}_i$ where $(\underline{e}_i)_{i\in\{1..3\}}$ are the unit vectors in the principal directions. We can first calculate the traction vector $\underline{t}_n$ acting on the surface of normal $\underline{n}$ from the Cauchy stress tensor $\underline{\underline{\sigma}}$:

$$\underline{t}_n = \underline{\underline{\sigma}} \cdot \underline{n} \tag{4.28}$$

[1] For anisotropic material, the failure also depends on the principal directions $(\underline{e}_1, \underline{e}_2, \underline{e}_3)$ defined in Section 1.2.1:

$$F(\sigma_1, \sigma_2, \sigma_3, \underline{e}_1, \underline{e}_2, \underline{e}_3) = K$$

.

The stress acting normal to the surface σ_N is then the projection of the traction vector $\underline{t}_n$ on the vector $\underline{n}$:

$$\begin{aligned}\sigma_N &= \underline{n} \cdot \underline{t}_n \\ &= \sigma_1 n_1^2 + \sigma_2 n_2^2 + \sigma_3 n_3^2\end{aligned} \tag{4.29}$$

where $(\sigma_i)_{i\in\{1..3\}}$ are the principal stresses defined in Section 1.2.1. The magnitude of the shear stress acting on the surface can then be deducted from (4.28) and (4.29):

$$\begin{aligned}|\sigma_S| &= \sqrt{|\underline{t}_n|^2 - \sigma_N^2} \\ &= \sqrt{(\sigma_1^2 n_1^2 + \sigma_2^2 n_2^2 + \sigma_3^2 n_3^2) - (\sigma_1 n_1^2 + \sigma_2 n_2^2 + \sigma_3 n_3^2)^2}\end{aligned} \tag{4.30}$$

Then for a particular stress configuration, defined independently of any coordinate system by the principal stresses $(\sigma_1, \sigma_2, \sigma_3)$, there is an infinity of (σ_N, σ_S) pairs possible, depending on the orientation of the surface the stress is acting on. This surface is completely defined by its normal vector $\underline{n} = (n_1, n_2, n_3)$. In order to give a two dimensional representation of the admissible stress configuration, we can use the Mohr's circles. From equations (4.29), (4.30) and the surface normal vector definition, we can write the following system:

$$\begin{cases} \sigma_1 n_1^2 + \sigma_2 n_1^2 + \sigma_3 n_1^2 &= \sigma_N \\ \sigma_1^2 n_1^2 + \sigma_2^2 n_1^2 + \sigma_3^2 n_1^2 &= \sigma_N^2 + \sigma_S^2 \\ n_1^2 + n_2^2 + n_3^2 &= 1 \end{cases} \tag{4.31}$$

Solving these equations for n_1, n_2 and n_3, we can find the surface orientation that corresponds to a particular (σ_N, σ_S) pair:

$$\begin{cases} n_1^2 = \dfrac{(\sigma_N - \sigma_2)(\sigma_N - \sigma_3) + \sigma_S^2}{(\sigma_1 - \sigma_2)(\sigma_1 - \sigma_3)} \\ n_2^2 = \dfrac{(\sigma_N - \sigma_3)(\sigma_N - \sigma_1) + \sigma_S^2}{(\sigma_2 - \sigma_3)(\sigma_2 - \sigma_1)} \\ n_3^2 = \dfrac{(\sigma_N - \sigma_1)(\sigma_N - \sigma_2) + \sigma_S^2}{(\sigma_3 - \sigma_1)(\sigma_3 - \sigma_2)} \end{cases} \tag{4.32}$$

Using that the squares of the normal components must be positive and that $\sigma_1 \geq \sigma_2 \geq \sigma_3$ we obtain three inequalities that can be interpreted as circle equations in the (σ_N, σ_S)

stress space:

$$\begin{cases} \sigma_S^2 + \left[\sigma_N - \frac{1}{2}(\sigma_2 + \sigma_3)\right]^2 \geq \left[\frac{1}{2}(\sigma_2 - \sigma_3)\right]^2 \\ \sigma_S^2 + \left[\sigma_N - \frac{1}{2}(\sigma_1 + \sigma_3)\right]^2 \leq \left[\frac{1}{2}(\sigma_1 - \sigma_3)\right]^2 \\ \sigma_S^2 + \left[\sigma_N - \frac{1}{2}(\sigma_1 + \sigma_2)\right]^2 \geq \left[\frac{1}{2}(\sigma_1 - \sigma_2)\right]^2 \end{cases} \tag{4.33}$$

Each point (σ_N, σ_S) represents the stress at the position of interest, within the material, on a particular plane. The system of equations (4.33) delimits the possible (σ_N, σ_S) pairs that are represented by the grey regions in Figure 4.1. We see that when the normal stress tends to one of the principal stresses, then the shear stress vanishes, in agreement with the definition of principal stresses. This occurs when the chosen plane normal gets aligned with one of the principal directions.

In the (σ_N, σ_S) stress space, the Coulomb friction equation (4.27) defines two lines (the failure lines) that can be superimposed to the Mohr's circles. As soon as the largest circle touches the failure lines, there is a particular plane for which the shear stress $|\sigma_S|$ reaches the yield stress. This situation is illustrated in Figure 4.2 from which we can deduce the expressions of σ_N and σ_S with respect to the principal stresses:

$$\begin{aligned} |\sigma_S| &= \frac{\sigma_1 - \sigma_3}{2}\cos\psi \\ \sigma_N &= \frac{\sigma_1 + \sigma_3}{2} - \frac{\sigma_1 - \sigma_3}{2}\sin\psi \end{aligned} \tag{4.34}$$

And finally we can write the Mohr-Coulomb criterion in the form of (4.25), combining (4.27) and (4.34). Thus the failure occurs when the following criterion is satisfied:

$$F_{MC}(\sigma_1, \sigma_2, \sigma_3) \doteqdot (\sigma_1 - \sigma_3) + (\sigma_1 + \sigma_3)\sin\psi = 2c\cos\psi \tag{4.35}$$

In the three dimensional principal stress space, this equation defines a surface referred to as the yield surface. However, it should be noted that, to obtain equation (4.35), we chose to order the principal stress in such a way that $\sigma_1 > \sigma_2 > \sigma_3$. Obviously, this condition is not necessarily respected for all the points in the principal stress space. To take this into account, we re-write (4.35) as:

$$F_{MC}(\sigma_1, \sigma_2, \sigma_3) \doteqdot (\max_{i\in\{1..3\}} \sigma_i - \min_{i\in\{1..3\}} \sigma_i) + (\max_{i\in\{1..3\}} \sigma_i + \min_{i\in\{1..3\}} \sigma_i)\sin\psi = 2c\cos\psi \tag{4.36}$$

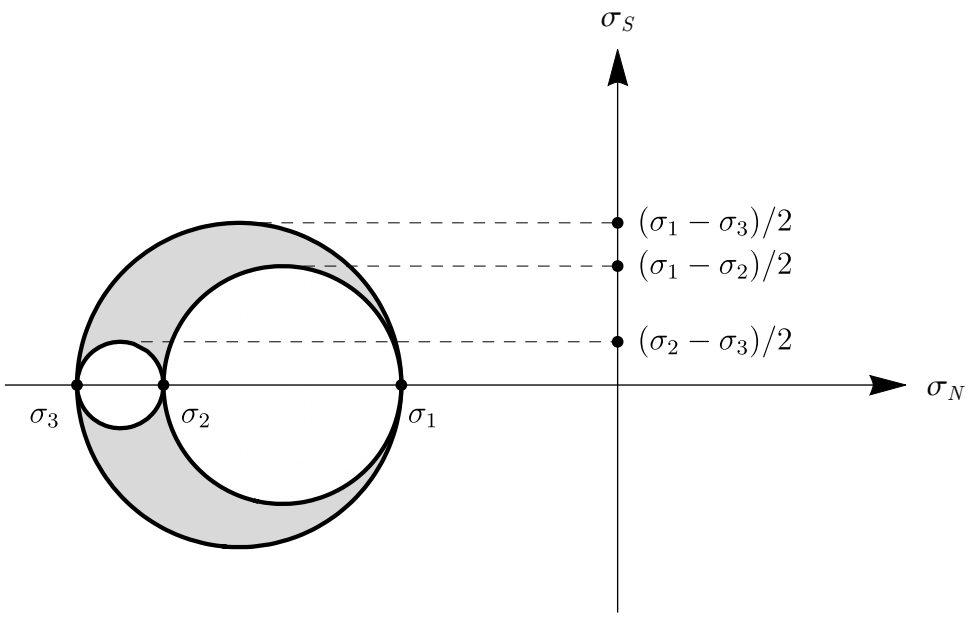

Figure 4.1: Mohr's circles – The grey region represents the admissible (σ_N, σ_S) pairs for a particular stress configuration defined by the principal stresses $(\sigma_1, \sigma_2, \sigma_3)$ independently of any coordinate system.

Figure 4.3a shows the surface defined by (4.36) in the 2D $(-\sigma_1, -\sigma_2)$ plane, while Figure 4.3b shows a view from the principal stress space diagonal defined by the vector $(1, 1, 1)$ and pointing the origin. The Mohr-Coulomb yield surface is thus an irregular hexagonal pyramid whose base is normal to the space diagonal.

Although (4.35) gives an invariant formulation of the Mohr-Coulomb criterion, it may raise practical issues. Indeed, this formulation requires to diagonalize the Cauchy Stress tensor in order to compute the principal stresses. A better option would be to use a formulation based on the invariants (I_1, J_2, J_3) defined in Section 1.2.1, to express the failure criterion in the form (4.26). Such a formula can be found in the literature [61]:

$$F_{MC}(I_1, J_2, J_3) \doteq \frac{1}{3} I_1 \sin\psi + \sqrt{J_2}\left(\cos\theta_L - \frac{1}{\sqrt{3}} \sin\theta_L \sin\psi\right) = c\cos\psi \tag{4.37}$$

where θ_L is the Lode's angle defined by:

$$\sin(3\theta_L) = \frac{3\sqrt{3} J_3}{2(J_2)^{3/2}} \tag{4.38}$$

However, the implementation of the Mohr-Coulomb criterion in a simulation code presents numerical difficulties due to the six sharp corners and the tips of the hexagonal pyramid [5, 61]. As a consequence, more regular yield criteria are usually preferred and the Drucker-Prager criterion is a good alternative.

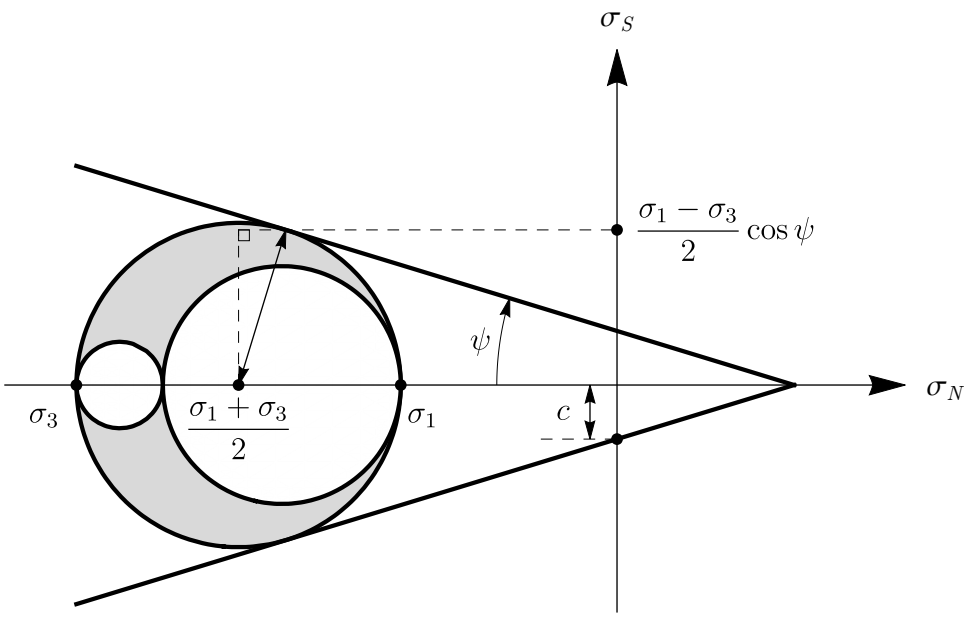

Figure 4.2: Mohr-Coulomb yield criterion.

(a) (b)

Figure 4.3: Mohr-Coulomb yield surface (a) in the $(-\sigma_1, -\sigma_2)$ plane, (b) from the principal stress space diagonal.

4.4.2 Drucker-Prager

The Drucker-Prager yield criterion is generally defined in the form (4.26) by:

$$F_{DP}(I_1, J_2) \doteqdot \alpha I_1 + \sqrt{J_2} = K \tag{4.39}$$

where α and K are material properties to be determined experimentally. Using (1.10) and (1.11), the latter expression can be written in terms of principal stresses :

$$F_{DP}(I_1, J_2, J_3) \doteqdot \alpha(\sigma_1 + \sigma_2 + \sigma_3) + \sqrt{\frac{1}{6}\left((\sigma_1 - \sigma_2)^2 + (\sigma_1 - \sigma_3)^2 + (\sigma_2 - \sigma_3)^2\right)} = K \tag{4.40}$$

In the three-dimensional stress space, the latter equation describes a conic yield surface whose base is normal to the stress space diagonal. Thus the parameters α and K can be related to the internal friction angle ψ and the cohesion c to match the Mohr-Coulomb hexagonal pyramid. They can be chosen in such a way that the Drucker-Prager yield surface circumscribes or inscribes the Mohr-Coulomb yield surface. Following the work of Fourtakas and Rogers [40], we choose α and K so that Drucker-Prager cone circumscribes the Mohr-Coulomb pyramid:

$$\alpha = \frac{2\sin\psi}{\sqrt{3}(3-\sin\psi)}, \quad K = \frac{6c\cos\psi}{\sqrt{3}(3-\sin\psi)} \tag{4.41}$$

With these values of α and K, the Drucker-Prager yield criterion reads:

$$F_{DP}(I_1, J_2, J_3) \doteqdot 2\sin\psi I_1 + \sqrt{3}(3-\sin\psi)\sqrt{J_2} = 6c\cos\psi \tag{4.42}$$

The yield surface is superimposed to the Mohr-Coulomb one in Figure 4.4.

(a) (b)

Figure 4.4: Drucker-Prager conic yield surface circumscribing the Mohr-Coulomb pyramidal yield surface (a) in the $(-\sigma_1, -\sigma_2)$ plane, (b) from the principal stress space diagonal.

4.4.3 Effective stress

Note that, the latter two yield criteria were described using the Cauchy stress tensor (1.8), thus they are defined within the continuum mechanics theory. Nevertheless, for soils and sediments, the two-phase nature of granular flows has a significant effect on the yield criterion, particularly for saturated material. This effect was first formalized by Terzaghi's [111] principle of effective stress, which states that "all measurable effects of a change of stress, such as compression, distortion, and a change of shearing resistance of a soil are exclusively due to changes in effective stress". As a consequence, "every investigation of the stability of a saturated body [...] requires the knowledge of both the total and the neutral stresses". The neutral stress refers to the pressure in the pore water while the effective

stress refers to the average inter-granular force per unit area. This principle traduces the fact that a variation of pore water pressure does not affect the inter-granular forces, because it acts equally all around the soil grains. Thus, it is implicitly assumed that the effective area of contact between the soil grains is negligible. The validity of Terzaghi's [111] principle has been widely investigated and verified [12, 56, 57]. A major consequence of this principle is that, for a saturated granular material, the height of water above the saturated material interface has no effect on the dynamics of the material.

To evaluate properly the implications of Terzaghi's [111] principle on the yield criteria, we can decompose the Cauchy stress tensor $\underline{\underline{\sigma}}$ into an effective stress $\underline{\underline{\sigma}}_{\text{eff}}$ and a neutral stress $\underline{\underline{\sigma}}_{\text{neutral}}$:

$$\underline{\underline{\sigma}} = \underline{\underline{\sigma}}_{\text{eff}} + \underline{\underline{\sigma}}_{\text{neutral}} \tag{4.43}$$

Recalling that the pore water pressure exerts stresses equally in all directions, the neutral stress is necessarily related to the isotropic part of the stress tensor:

$$\underline{\underline{\sigma}} = \underline{\underline{\sigma}}_{\text{eff}} - p_{\text{pw}}\underline{\underline{I}} \tag{4.44}$$

with p_{pw} the pore water pressure. From the latter equation and (1.5), we can write $\underline{\underline{\sigma}}_{\text{eff}}$ in terms of principal stresses as:

$$\underline{\underline{\sigma}}_{\text{eff}} = \begin{pmatrix} \sigma_1 + p_{\text{pw}} & 0 & 0 \\ 0 & \sigma_2 + p_{\text{pw}} & 0 \\ 0 & 0 & \sigma_3 + p_{\text{pw}} \end{pmatrix} \tag{4.45}$$

With these definitions, we can now evaluate the effect of Terzaghi's [111] principle on the two yield criteria[2].

Effect on Mohr-Coulomb's yield criterion

Taking (4.45) into account, (4.34) is modified as:

$$\begin{aligned} |\sigma_{S,\text{eff}}| &= \frac{\sigma_1 - \sigma_3}{2}\cos\psi = |\sigma_S| \\ \sigma_{N,\text{eff}} &= \frac{\sigma_1 + \sigma_3}{2} - \frac{\sigma_1 - \sigma_3}{2}\sin\psi + p_{\text{pw}} = \sigma_N + p_{\text{pw}} \end{aligned} \tag{4.46}$$

The latter equation shows that only the normal stress σ_N is affected by the pore water pressure. Relating (4.46) to the Mohr-Coulomb criterion, Figure 4.2 shows that the pore

[2] Although Mohr-Coulomb yield criterion will not be used in this work.

water pressure does not affects the circles diameters, *e.g.* $(\sigma_1 - \sigma_3)/2$, while it involves a translations of the circles centres. As a consequence, for a given normal stress σ_N, the shear the material can sustain according to the Mohr-Coulomb criterion is smaller when the pore water pressure is taken into account. The critical shear stress magnitude is now given by:

$$|\sigma_S| = (-\sigma_N - p_{\text{pw}}) \tan\psi + c \tag{4.47}$$

Regarding the Mohr-Coulomb criterion formulated in terms of invariants (4.37), we must evaluate the effective stress tensor (4.45) invariants $I_{1,\text{eff}}$, $J_{2,\text{eff}}$ and $J_{3,\text{eff}}$ from the definitions (1.10), (1.12) and (1.14):

$$I_{1,\text{eff}} = \sigma_1 + \sigma_2 + \sigma_3 - 3\,p_{\text{pw}} = I_1 + 3\,p_{\text{pw}} \tag{4.48}$$

$$J_{2,\text{eff}} = \frac{1}{6}\left((\sigma_1 - \sigma_2)^2 + (\sigma_1 - \sigma_3)^2 + (\sigma_2 - \sigma_3)^2\right) = J_2 \tag{4.49}$$

$$J_{3,\text{eff}} = \sum_{i\in\{1..3\}} \left(\sigma_i + p_{\text{pw}} - \frac{1}{3}\left(\sigma_1 + \sigma_2 + \sigma_3 + 3\,p_{\text{pw}}\right)\right) = J_3 \tag{4.50}$$

As expected, J_2 and J_3 are not modified when taking into account Terzaghi's [111] principle since they are related to the deviatoric part of the stress tensor $\underline{\underline{\sigma}}$ while the neutral stress is related to the isotropic part by of $\underline{\underline{\sigma}}$. The Mohr-Coulomb criterion now reads:

$$F_{MC}(I_1, J_2, J_3) \doteqdot \left(\frac{1}{3}I_1 + p_{\text{pw}}\right)\sin\psi + \sqrt{J_2}\left(\cos\theta_L - \frac{1}{\sqrt{3}}\sin\theta_L \sin\psi\right) = c\cos\psi \tag{4.51}$$

Effect on Drucker-Prager's yield criterion

Regarding the Drucker-Prager criterion, we use (4.48) and (4.49) to modify (4.42) according to Terzaghi's [111] principle. The Drucker-Prager criterion now reads:

$$F_{DP}(I_1, J_2) \doteqdot 2\sin\psi(I_1 + 3p_{\text{pw}}) + \sqrt{3}(3 - \sin\psi)\sqrt{J_2} = 6c\cos\psi \tag{4.52}$$

In the scope of this thesis, we only consider non-cohesive sediments, *i.e.* $c = 0$. Finally, using (1.8) to write Drucker-Prager's yield criterion in term of pressure, we finally have:

$$F_{DP}(p_{\text{eff}}, J_2) \doteqdot 2\sqrt{3}\sin\psi\,(-p + p_{\text{pw}}) + (3 - \sin\psi)\sqrt{J_2} = 0 \tag{4.53}$$

The Drucker-Prager's yield criterion is thus a pressure-dependent model and the failure occurs when the shear stress second invariant square root $\sqrt{J_2}$ reaches the following yield

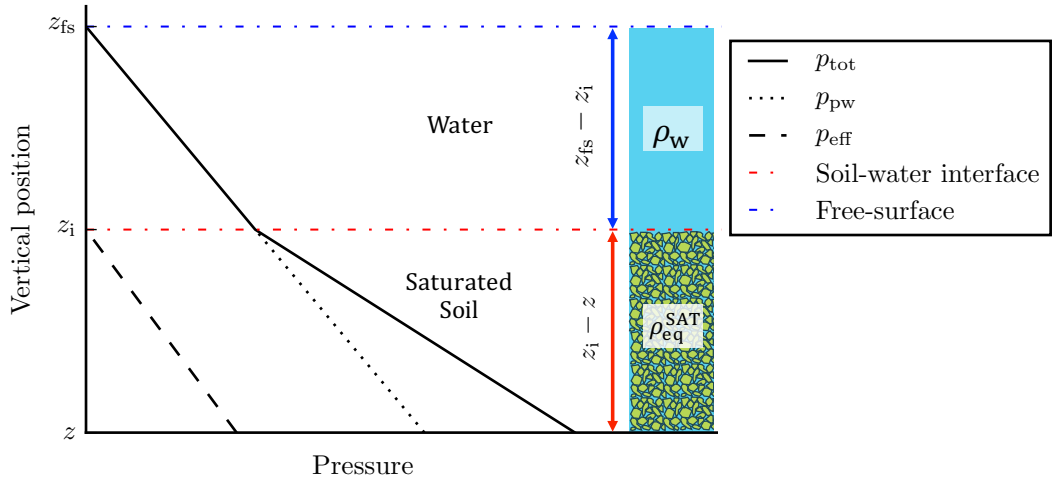

Figure 4.5: Characteristic pressures in a submerged bed of soil saturated with water.

stress τ_y:

$$\tau_y = \frac{2\sqrt{3}\sin\psi}{(3-\sin\psi)} p_{eff} \tag{4.54}$$

where the effective pressure p_{eff} is defined as:

$$p_{eff} = p - p_{pw} \tag{4.55}$$

4.4.4 Effective pressure

Here we consider the case of a saturated and submerged material, as illustration in Figure 4.5. Having an accurate evaluation of the yield stress is mandatory to predict the material failure and thus the transitions between the solid state and the granular flow regime. In this work, Drucker-Prager's yield criterion (4.54) is used so we need to properly evaluate the effective pressure (4.55). Considering a situation where the stress configuration is close to the failure, almost no motion occurs within the material. Therefore, the isotropic stress (*i.e.* the pressure p) is solely due to pressure derived from the weight of the column of material and interstitial fluid above a specified level, *i.e.* the lithostatic pressure p_{lit}. For any material, the lithostatic pressure at a position $\underline{r} = (x, y, z)$ is given by :

$$p_{lit}(\underline{r}) = p_0 + g \int_z^{z_0} \rho(\underline{r}\,') \, dz' \tag{4.56}$$

with $\underline{g} = -g\,\underline{e}_z$ the gravity, and p_0 the pressure at position $\underline{r}_0 = (x, y, z_0)$. Thus, close to the failure, the effective pressure can be written in term of pore water and lithostatic

pressures:

$$p_{\text{eff}}(\underline{r}) = p_{\text{lit}}(\underline{r}) - p_{\text{pw}}(\underline{r}) \tag{4.57}$$

With (4.4) the lithostatic pressure (4.56) simplifies as:

$$p_{\text{lit}}(\underline{r}) = \rho_{\text{w}} g \left[z_{\text{fs}}(\underline{r}) - z_{\text{i}}(\underline{r})\right] + \rho_{\text{eq}}^{\text{sat}} g \left[z_{\text{i}}(\underline{r}) - z\right] \tag{4.58}$$

with z_{i} the elevation of the mixture-water interface, and z_{fs} the elevation of the free surface above the point $\underline{r}$ (see Figure 4.5). From Equation (4.57), it is apparently necessary to solve the porous flow inside the soil to compute the effective pressure properly. However, as detailed in Section 4.2, the internal porous flow is neglected and the pore water pressure is assumed to be hydrostatic:

$$p_{\text{pw}}(\underline{r}) = \rho_{\text{w}} g \left[z_{\text{fs}}(\underline{r}) - z\right] \tag{4.59}$$

Finally, the effective pressure can be obtained using (4.57):

$$p_{\text{eff}}(\underline{r}) = g \left[z_{\text{i}}(\underline{r}) - z\right] \left[\rho_{\text{eq}}^{\text{sat}} - \rho_{\text{w}}\right] \tag{4.60}$$

Here we see that assuming a lithostatic isotropic stress and a hydrostatic pore water pressure is consistent with Terzaghi's [111] principle (presented in Section 4.4.3) since (4.60) does not depend on the free-surface position above the sediment bed. Nevertheless, getting p_{eff} from (4.60) requires to detect mixture-water interface z_{i} beforehand. Such a detection has been numerically tested by Manenti et al. [74] but it seems to us that it can lead to inaccurate result when the interface is highly deformed. In order to get effective pressure without interface tracking, Fourtakas et al. [41] proposed to use a modified state equation. However, we found that this method leads to a large overestimation of p_{eff} when the soil is submerged, while according to Terzaghi's [111] principle, the effective pressure should not depend on the height of water above the granular material interface. Furthermore, with such an approach, the pressure oscillations due to the chequerboard effect in WCSPH (see Section 2.6) also impact the yield stress.

Therefore, we propose here another simple and reliable solution. Although a weakly-compressible formulation is used in this work, we aim at modelling incompressible materials. The equation of state (1.25) is a numerical way of closing the systems (1.17) and (1.24), but the compressible effects are not supposed to play any role in the behaviour of the granular material. Thus, we assume here that ρ_{w} and $\rho_{\text{eq}}^{\text{sat}}$ are constant. In addition, z_{i} is the function that gives the mixture-water interface above the point $\underline{r}$, so it does not depend on the vertical coordinate:

$$z_{\text{i}}(\underline{r}) = z_{\text{i}}(x, y) \tag{4.61}$$

As long as the water-mixture interface is not too much deformed, we can assume that the interface varies linearly with x and y in the vicinity of the point of interest (this is the strongest assumption done in this reasoning). Thus, taking the Laplacian of (4.60) yields:

$$\nabla^2 p_{\text{eff}} = 0 \tag{4.62}$$

Therefore, the effective pressure can be obtained solving the latter equation with suitable boundary conditions. At the mixture-water interface, the effective pressure must be zero so we use a simple Dirichlet condition. At solid walls, a Neumann condition similar to the dynamic condition (1.32) can be used. We finally get the following system:

$$\begin{cases} \nabla^2 p_{\text{eff}}(\underline{r}) = 0 & \text{for} \quad \underline{r} \in \Omega \\ p_{\text{eff}}(\underline{r}) = 0 & \text{for} \quad \underline{r} \in \mathcal{I} \\ \dfrac{\partial p_{\text{eff}}}{\partial \underline{n}}(\underline{r}) = \left[\rho_{\text{eq}}^{\text{sat}} - \rho_{\text{w}}\right] \underline{g} \cdot \underline{n} & \text{for} \quad \underline{r} \in \mathcal{S} \end{cases} \tag{4.63}$$

with Ω the simulation domain, $\mathcal{S}$ the solid boundaries, $\underline{n}$ the inward boundary normal and $\mathcal{I}$ the boundary corresponding to soil free-surface and soil-water interface (see Figure 4.5). Finally, it should be noted that (4.63) can easily be adapted for dry materials. Indeed, the effect of interstitial air being neglected, the pore pressure vanishes and $\rho_{\text{eq}}^{\text{dry}}$ be used instead of $\rho_{\text{eq}}^{\text{sat}}$. Everything else remains unchanged and we can write a system for dry and saturated materials:

$$\begin{cases} \nabla^2 p_{\text{eff}}(\underline{r}) = 0 & \text{for} \quad \underline{r} \in \Omega \\ p_{\text{eff}}(\underline{r}) = 0 & \text{for} \quad \underline{r} \in \mathcal{I} \\ \dfrac{\partial p_{\text{eff}}}{\partial \underline{n}}(\underline{r}) = \Delta\rho_{\text{eq}}\, \underline{g} \cdot \underline{n} & \text{for} \quad \underline{r} \in \mathcal{S} \end{cases} \tag{4.64}$$

with:

$$\Delta\rho_{\text{eq}} = \begin{cases} \rho_{\text{eq}}^{\text{sat}} - \rho_{\text{w}} & \text{for saturated material} \\ \rho_{\text{eq}}^{\text{dry}} & \text{for dry material} \end{cases} \tag{4.65}$$

4.5 Shear stresses

4.5.1 Elastic solid state

As explained in Section 4.3.2, the solid state of the granular material is evaluated in line with linear elastic theory. Thus, the set of equations (1.24) presented in Section 1.2.2.2 is used. The shear stress tensor in the solid regions can be obtained from the following rate of stress equation:

$$\dot{\underline{\underline{\tau}}}^{\,\mathrm{s}}_{\mathrm{g}} = 2\,\mathcal{G}\,\dot{\underline{\underline{\gamma}}} \tag{4.66}$$

where $\mathcal{G}$ is the shear modulus (1.21), the dot $\dot{}$ denotes the time derivative, the subscript $_{\mathrm{g}}$ refers to the granular material, and the superscripts $^{\mathrm{s}}$ refers to the elastic-solid model, *i.e.* the solid state. Here we differentiated the solid state constitutive equation (1.22) for the following reason. It can be shown that the rate of stress (4.66) is not objective, *i.e.* it is not independent on the frame of reference. In particular, it is not invariant with respect to rigid-body rotation. Though, the material constitutive equations should be frame indifferent since the mechanical response of a material must not depend on the observer. Thus the dynamic quantities, such as the Cauchy stress tensor, are frame invariant [30, 52]. Considering a mapping from a frame of reference $\mathcal{R}$ to another one $\mathcal{R}^*$, characterized by an orthogonal time-dependent second order tensor $\underline{\underline{Q}}$ describing a solid-body rotation, we have:

$$\underline{\underline{\sigma}}^{\,*} = \underline{\underline{Q}}\,(t)\,\underline{\underline{\sigma}}\,\underline{\underline{Q}}^{\,T}(t) \tag{4.67}$$

which is the objectivity required condition for a second order tensor [52]. Taking the time derivative of the previous equation yields:

$$\begin{aligned}\dot{\underline{\underline{\sigma}}}^{\,*} &= \dot{\underline{\underline{Q}}}\,\underline{\underline{\sigma}}\,\underline{\underline{Q}}^{\,T} + \underline{\underline{Q}}\,\dot{\underline{\underline{\sigma}}}\,\underline{\underline{Q}}^{\,T} + \underline{\underline{Q}}\,\underline{\underline{\sigma}}\,\dot{\underline{\underline{Q}}}^{\,T} \\ &\neq \underline{\underline{Q}}\,\dot{\underline{\underline{\sigma}}}\,\underline{\underline{Q}}^{\,T}\end{aligned} \tag{4.68}$$

thus demonstrating that (4.66) is not invariant with respect to time-dependent rigid-body rotation, and is consequently not suitable for large deformations. This demonstrates that the material time derivative of an objective tensor is not objective. To circumvent this issue, objective material time derivatives must be used. The most commonly used in computational mechanics is the Jaumann time derivative, denoted with a triangle $^{\vartriangle}$ and defined by:

$$\overset{\vartriangle}{\underline{\underline{\sigma}}} = \dot{\underline{\underline{\sigma}}} + \underline{\underline{\sigma}}\,\dot{\underline{\underline{\omega}}} - \dot{\underline{\underline{\omega}}}\,\underline{\underline{\sigma}} \tag{4.69}$$

where $\dot{\underline{\underline{\omega}}}$ is the rotation rate tensor that is directly related to the rate of rigid-body rotation

within a material:

$$\underline{\underline{\dot{\omega}}} = \frac{1}{2}\left(\underline{\underline{\text{grad}}}\ \underline{u} - \left(\underline{\underline{\text{grad}}}\ \underline{u}\right)^T\right) \tag{4.70}$$

Note that, when no rigid-body rotation occurs within the material, the Jaumann material derivative (4.69) is tantamount to the standard material time derivative. Applying (4.69) to the deviatoric stress tensor $\underline{\underline{\tau}}$ yields:

$$\overset{\Delta}{\underline{\underline{\tau}}}{}^{\mathrm{s}}_{\mathrm{g}} = 2\,\mathcal{G}\,\underline{\underline{\dot{\gamma}}} + \underline{\underline{\dot{J}}} \tag{4.71}$$

denoting $\underline{\underline{\dot{J}}}$ the Jaumann rate tensor defined by:

$$\underline{\underline{\dot{J}}} = \underline{\underline{\tau}}^{\mathrm{s}}_{\mathrm{g}}\,\underline{\underline{\dot{\omega}}} - \underline{\underline{\dot{\omega}}}\,\underline{\underline{\tau}}^{\mathrm{s}}_{\mathrm{g}} \tag{4.72}$$

The shear stress tensor finally reads:

$$\underline{\underline{\tau}}^{\mathrm{s}}_{\mathrm{g}} = 2\,\mathcal{G}\,\underline{\underline{\gamma}} + \underline{\underline{J}} \tag{4.73}$$

which is more relevant than the initial attempt (1.22). Furthermore, the material is supposed to yield when the stress magnitude reaches the yield stress. Thus, the solid deviatoric stress tensor should be rescaled so that its invariant never exceeds the yield stress:

$$\begin{cases} \underline{\underline{\tau}}^{\mathrm{ss}}_{\mathrm{g}} = \underline{\underline{\tau}}^{\mathrm{s}}_{\mathrm{g}} & \text{if} \quad \tau^{\mathrm{s}}_{\mathrm{g}} \leq \tau_{\mathrm{y}} \\ \underline{\underline{\tau}}^{\mathrm{ss}}_{\mathrm{g}} = \dfrac{\tau_{\mathrm{y}}}{\tau}\underline{\underline{\tau}}^{\mathrm{s}}_{\mathrm{g}} & \text{if} \quad \tau^{\mathrm{s}}_{\mathrm{g}} > \tau_{\mathrm{y}} \end{cases} \tag{4.74}$$

where $\underline{\underline{\tau}}^{\mathrm{ss}}_{\mathrm{g}}$ denotes the rescaled deviatoric stress tensor.

4.5.2 Viscoplastic fluid state

In yielded regions, the material is modelled as a shear thinning liquid. Thus the viscous fluid constitutive equation presented in Section 1.2.2.1 is used to model the shear stress:

$$\underline{\underline{\tau}}^{\mathrm{l}}_{\mathrm{g}} = 2\,\eta_{\mathrm{eff}}\underline{\underline{\dot{\gamma}}} \tag{4.75}$$

where the superscript l refers to the viscoplastic model, *i.e.* the liquid state. In Ulrich's [114] original model, the effective viscosity η_{eff} was calculated according to a rheological law similar to the $\mu(I)$ rheology [62] presented in Section 4.3.1. Here, we propose a different law in order to be consistent with the Drucker-Prager yield criterion. The effective viscosity is thus defined by:

$$\eta_{\mathrm{eff}} = \frac{\tau_{\mathrm{y}}}{\dot{\gamma}} \tag{4.76}$$

where τ_y is the yield stress calculated according to (4.54). Therefore, similarly to the $\mu(I)$ rheology [62, 100], the effective viscosity is related to the friction within the granular material. However, here the friction coefficient is constant in time since the internal friction ψ is a constant parameter in our model. It should be noted that (4.76) ensures the continuity of the shear stress magnitude in the liquid-solid transition since we have:

$$\tau_g^l = \sqrt{\frac{1}{2}\underline{\underline{\tau}}_g^l : \underline{\underline{\tau}}_g^l} = \eta_{\text{eff}}\,\dot{\gamma} = \tau_y \tag{4.77}$$

4.5.3 Solid-fluid transition

A numerical continuous transition between solid and liquid state is ensured by a blending function ζ driven by the magnitude of strain rate. Since the physical threshold delimiting yielded and unyielded regions is expressed is terms of stress (i.e the yield stress τ_y), we need to build a new one expressed in terms of strain rate, hereafter denoted by $\dot{\gamma}_y$:

$$\dot{\gamma}_y = \frac{\tau_y}{\eta_y} \tag{4.78}$$

where η_y is a dynamic viscosity referred to as yield viscosity. Thus, (4.78) points out that the solid-fluid transition depends on an additional parameter η_y. Moreover, the yield viscosity not only determines the threshold strain rate but also the maximum possible viscosity for the material in fluid state.

In Ulrich [114], the value of η_y is chosen in a trial and error approach, increasing incrementally its value until obtaining satisfying result. Here we propose to find a value based on the physical properties of the material. To do so, we first consider the Deborah number De which characterizes the fluidity of a material under the flow conditions of a specific experiment:

$$De = \frac{t_R}{t_C} \tag{4.79}$$

where t_C is the characteristic time scale of the experiment, and t_R the stress relaxation time. For a granular material, Sun and Wang [106] proposed to use the characteristic time of Rayleigh waves propagating along a grain surface:

$$t_R^G = \frac{\pi d_g}{0.162\nu + 0.887}\sqrt{\frac{\rho_g}{\mathcal{G}}} \tag{4.80}$$

with d_g the grain diameter. On the other hand, during the transition, the soil can be seen as a viscoelastic material. In that case, the Deborah number is calculated with a relaxation time defined as:

$$t_R^{VE} = \frac{\eta_y}{\mathcal{G}} \tag{4.81}$$

For a given material, the two relaxation time definitions should match. Therefore, combining (4.80) and (4.81) gives a definition of the yield viscosity:

$$\eta_y = \frac{\pi d_g \sqrt{\mathcal{G}\rho_g}}{0.163\nu + 0.877} \tag{4.82}$$

We can now use the blending function proposed by Ulrich [114]:

$$\zeta(\dot{\gamma}) = \begin{cases} (q+1)\left(\frac{\dot{\gamma}}{\dot{\gamma}_y}\right)^q - q\left(\frac{\dot{\gamma}}{\dot{\gamma}_y}\right)^{q+1} & \text{if} \quad \dot{\gamma} < \dot{\gamma}_y \\ 1 & \text{if} \quad \dot{\gamma} \geq \dot{\gamma}_y \end{cases} \tag{4.83}$$

with q a positive integer. The solid-liquid transition sharpness can be adjusted varying q. Similarly to Ulrich [114], we use $q = 2$. Finally, the fluid-solid deviatoric stress tensor is given by:

$$\underline{\underline{\tau}} = \zeta\, \underline{\underline{\tau}}_g^{\,l} + (1-\zeta)\, \underline{\underline{\tau}}_g^{\,ss} \tag{4.84}$$

It is important to note that the solid stresses in the soil should vanish when the fluid state is reached. Thus, the strain tensor must be reinitialized when $\zeta \to 1$.

Finally, in this model the mechanical behaviour of the soil only depends on elastic (E, ν) and granular (d_g, ρ_g, ϕ, ψ) properties of the material, especially through (4.54) and (4.82) that drive the liquid-solid transition.

4.6 SPH implementation

In SPH the continuum is sampled in a set of interpolation points $\mathcal{F}$ having a constant mass m_a and referred to as *particles*. An SPH particle used to discretize a granular material continuum represents a small volume that contains a mixture of solid grains and surrounding fluid. The equivalent density of the continuum is calculated from (4.4). The present granular material model is implemented within the scope of the multi-phase SPH formulation presented in Section 3.2. First, let us define (or recall) the following sets of SPH particles:

- $\mathcal{V}$ is the set of vertex particles (see USAW framework in Section 2.5.2.2)
- $\mathcal{S}$ is the set of boundary elements (see USAW framework in Section 2.5.2.2)

- $\mathcal{M}$ is the set of free particles of granular material (mixture of grains and surrounding fluid)

- $\mathcal{W}$ is the set of free particles of water

- $\mathcal{F}$ is the set of free particles of matter: $\mathcal{F} = \mathcal{M} \cup \mathcal{W}$

- $\mathcal{I}$ is the set of free particles of matter at the water-mixture interface: $\mathcal{I} \subset \mathcal{F}$

4.6.1 Effective pressure

To compute the effective pressure p_{eff}, we need to solve the Laplace equation (4.64). Thus we use Morris' Laplacian (2.77) to write the corresponding discrete equation:

$$\forall a \in (\mathcal{M} \backslash \mathcal{I}) \quad L_a^M \{1, p_{\text{eff},b}\} = 0 \tag{4.85}$$

where $(\mathcal{M} \backslash \mathcal{I})$ refers to the set of SPH particles of mixture that are not located at the interface. At the wall, the Neumann boundary conditions (4.64) must be satisfied. Following Ferrand et al. [37], we use a Shepard-like interpolation of the effective pressure field similarly to (2.91):

$$\forall a \in (\mathcal{V} \cup \mathcal{S}) \quad p_{\text{eff},a} = \frac{1}{\sum\limits_{b \in \mathcal{M}} V_b w_{ab}} \left(\sum_{b \in \mathcal{M}} V_b \left(p_{\text{eff},b} + \Delta\rho_{\text{eq}} \underline{g} \cdot (\underline{r}_a - \underline{r}_b) \right) w_{ab} \right) \tag{4.86}$$

with $(\mathcal{V} \cup \mathcal{S})$ the set of boundary elements and vertex particles. Besides, a particular attention must be paid to the Dirichlet condition imposed to soil particles located at the soil-water interface (second line of (4.64)). Indeed, the pressure due to their own weight must be taken into account, otherwise the yield stress (4.54) is always zero at interface particles:

$$\forall a \in (\mathcal{M} \cap \mathcal{I}) \quad p_{\text{eff},a} = g \delta r \, \Delta\rho_{\text{eq}} \tag{4.87}$$

with $(\mathcal{M} \cap \mathcal{I})$ the set of SPH particles of mixture located at the interface, and δr the initial particle spacing (2.26) (*i.e.* the particle size). Finally, (4.85) is solved using a Jacobi solver initialized with the previous time step solution, thus ensuring low computational cost.

4.6.2 Shear forces

4.6.2.1 Elastic solid force density

To compute elastic forces, we first need to compute the strain rate tensor $\underline{\underline{\dot{\gamma}}}$ and the rotation rate tensor $\underline{\underline{\dot{\omega}}}$:

$$\underline{\underline{\dot{\gamma}}}_a = \frac{1}{2}\left(\underline{\underline{G}}_a\{\underline{u}_b\} + \left(\underline{\underline{G}}_a\{\underline{u}_b\}\right)^T\right) - \frac{1}{3}\mathrm{Tr}\left(\underline{\underline{G}}_a\{\underline{u}_b\}\right)\underline{\underline{I}} \tag{4.88}$$

$$\underline{\underline{\dot{\omega}}}_a = \frac{1}{2}\left(\underline{\underline{G}}_a\{\underline{u}_b\} + \left(\underline{\underline{G}}_a\{\underline{u}_b\}\right)^T\right) \tag{4.89}$$

where the multi-phase anti-symmetric gradient based on (3.26) is used here:

$$\underline{\underline{G}}_a\{\underline{u}_b\} = -\frac{\overline{V}_a}{\Gamma_a}\sum_{b\in(\mathcal{F}\cup\mathcal{V})}\theta_b\left(\underline{u}_a - \underline{u}_b\right)\otimes\underline{\nabla}w_{ab} + \frac{\overline{V}_a}{\Gamma_a}\sum_{s\in\mathcal{S}}\frac{1}{\overline{V}_s}\left(\underline{u}_a - \underline{u}_s\right)\otimes\underline{\nabla}\Gamma_{as} \tag{4.90}$$

with $\otimes$ denoting the tensor product. Note that the anti-symmetric gradient (4.90) is used instead of (3.25) for more accuracy. It should also be reminded that the trace of the velocity gradient should be zero for an incompressible fluid. But within the scope of WCSPH, we have to remove the trace from the strain rate tensor in (4.88), to ensure that the deviatoric stress tensor $\underline{\underline{\tau}}$ is really traceless. The shear stress tensor then follows from an explicit time-integration of the Jaumann rate of shear stress (4.71):

$$\underline{\underline{\tau}}_{\mathrm{g}}^{\mathrm{s}} = \overline{2\,\mathcal{G}\,\underline{\underline{\dot{\gamma}}} + \underline{\underline{\tau}}\,\underline{\underline{\dot{\omega}}} - \underline{\underline{\dot{\omega}}}\,\underline{\underline{\tau}}} \tag{4.91}$$

where the overbar indicates explicit time integration. Then, the elastic solid force density could be simply computed from the divergence of the deviatoric stress tensor:

$$\underline{\mathrm{div}}\,\underline{\underline{\tau}}_{\mathrm{g}}^{\mathrm{s}} = \underline{\mathrm{div}}\left(2\,\mathcal{G}\,\underline{\underline{\gamma}}\right) + \underline{\mathrm{div}}\,\underline{\underline{J}} \tag{4.92}$$

Numerically, this implies two iterative use of first order SPH derivative operators. Indeed, (4.91) requires computing the strain rate tensor $\underline{\underline{\dot{\gamma}}}$ using the SPH gradient of velocity. Then, (4.92) requires to take the SPH divergence of the shear stress tensor [48, 114]. Thus, focusing on the first term in (4.92) yields:

$$\left(\underline{\mathrm{div}}\left(2\,\mathcal{G}\,\underline{\underline{\gamma}}\right)\right)_a \approx \mathcal{G}\,\underline{D}_a\left\{\overline{\left(\underline{\underline{G}}_b\{\underline{u}_c\} + \left(\underline{\underline{G}}_b\{\underline{u}_c\}\right)^T\right)}\right\} \tag{4.93}$$

But due to the collocated nature of SPH, applying iteratively first order derivative operators to get higher order derivatives leads to significant inaccuracy (see Section 2.6).

This can be avoided observing that the shear strain tensor $\underline{\underline{\gamma}}$ can be calculated from the displacement $\underline{X}$ instead of the time-integration of the strain rate tensor:

$$\underline{\underline{\gamma}} = \frac{1}{2}\left(\underline{\underline{\text{grad}}}\ \underline{X} + \left(\underline{\underline{\text{grad}}}\ \underline{X}\right)^T\right) \tag{4.94}$$

This definition of shear strain tensor (4.94) is particularly adapted to SPH whose Lagrangian characteristic gives a direct access to particle displacement:

$$\underline{X}\,(t) = \underline{r}\,(t) - \underline{r}\,(0) \tag{4.95}$$

Then the shear strain divergence can be obtained using Espanol and Revenga's [33] second order derivative operator $\underline{L}^{\,E}$ defined in (2.78). Contrary to (3.12) and (3.29), Espanol and Revenga's [33] formula (2.46) is not an approximation of the Laplacian (see Section 2.3.3):

$$\underline{L}_a^{\,E}\{B_b, \underline{A}_b\} \approx \left(\underline{\text{div}}\left(B\left[\underline{\underline{\text{grad}}}\ \underline{A} + (\underline{\underline{\text{grad}}}\ \underline{A})^T\right]\right)\right)_a \tag{4.96}$$

Now, applying (2.46) to shear modulus $\mathcal{G}$ and displacement $\underline{X}$ we get:

$$\left(\underline{\text{div}}\left(2\,\mathcal{G}\,\underline{\underline{\gamma}}\right)\right)_a \approx \mathcal{G}\,\underline{L}_a^{\,E}\{1, \underline{X}_b\} \tag{4.97}$$

A similar treatment of the Jaumann term does not seem to be possible, so the shear force density f finally reads:

$$\left(\underline{f}_{\,\mathrm{g}}^{\,\mathrm{s}}\right)_a = \mathcal{G}\,\underline{L}_a^{\,E}\{1, \underline{X}_b\} + \underline{D}_a\{\underline{J}_b\} \approx \left(\underline{\text{div}}\ \underline{\underline{\tau}}_{\,\mathrm{g}}^{\,\mathrm{l}}\right)_a \tag{4.98}$$

where the tensor $\underline{\underline{J}}$ follows from an explicit time-integration of the Jaumann rate tensor (4.72):

$$\underline{\underline{J}}^{\,(n+1)} = \underline{\underline{J}}^{\,(n)} + \Delta t\left(\underline{\underline{\tau}}_{\,\mathrm{g}}^{\,\mathrm{s}}\,\underline{\underline{\dot{\omega}}} - \underline{\underline{\dot{\omega}}}\,\underline{\underline{\tau}}_{\,\mathrm{g}}^{\,\mathrm{s}}\right)^{(n)} \tag{4.99}$$

The force density $\underline{f}_{\,\mathrm{g}}^{\,\mathrm{s}}$ is rescaled afterwards according to (4.74) (here we omit the SPH particle labels for the sake of clarity):

$$\begin{cases} \underline{f}_{\,\mathrm{g}}^{\,\mathrm{ss}} = \underline{f}_{\,\mathrm{g}}^{\,\mathrm{s}} & \text{if} \quad \tau_{\mathrm{g}}^{\mathrm{s}} \le \tau_{\mathrm{y}} \\ \underline{f}_{\,\mathrm{g}}^{\,\mathrm{ss}} = \dfrac{\tau_{\mathrm{y}}}{\tau_{\mathrm{g}}^{\mathrm{s}}}\,\underline{f}_{\,\mathrm{g}}^{\,\mathrm{s}} & \text{if} \quad \tau_{\mathrm{g}}^{\mathrm{s}} > \tau_{\mathrm{y}} \end{cases} \tag{4.100}$$

Note that the latter rescaling is not tantamount to (4.74). Indeed, here we rescale forces

instead of stresses, which means that the following approximation is done:

$$\operatorname{div}\left(\frac{\tau_{\mathrm{y}}}{\tau_{\mathrm{g}}^{\mathrm{s}}}\,\underline{\underline{\tau}}_{\mathrm{g}}^{\mathrm{s}}\right) \approx \frac{\tau_{\mathrm{y}}}{\tau_{\mathrm{g}}^{\mathrm{s}}}\operatorname{div}\left(\underline{\underline{\tau}}_{\mathrm{g}}^{\mathrm{s}}\right) \tag{4.101}$$

This is mandatory when using (4.97) instead of (4.93) because the stress tensor $\underline{\underline{\tau}}_{\mathrm{g}}^{\mathrm{s}}$ is not directly used to compute the forces. Although it will be seen that using (4.97) improves the computation of elastic forces (see Section 5.3.1), it would be necessary to evaluate the effect of the latter approximation on the model accuracy to ascertain whether (4.97) is globally better. Unfortunately, such an investigation has not been carried out in the scope of this work.

4.6.2.2 Viscous force density

When the material is in the viscoplastic liquid state, the force density is given by:

$$\left(\underline{\operatorname{div}}\ \underline{\underline{\tau}}_{\mathrm{g}}^{\mathrm{l}}\right)_a = \left(\operatorname{div}\left(2\,\eta_{\mathrm{eff}}\,\underline{\underline{\dot{\gamma}}}\right)\right)_a \tag{4.102}$$

Thus, it is computed applying (2.46) to the effective viscosity η_{eff} and the velocity $\underline{u}$:

$$\left(\underline{f}_{\mathrm{g}}^{\mathrm{l}}\right)_a = \underline{L}_a^E\{\eta_{\mathrm{eff},b}, \underline{u}_b\} \approx \left(\operatorname{div}\left(2\,\eta_{\mathrm{eff}}\,\underline{\underline{\dot{\gamma}}}\right)\right)_a \tag{4.103}$$

Here again, Espanol and Revenga's [33] operator is used instead of Morris' viscous term. This is due to the fact that the transposed velocity gradient in (1.16) cannot be neglected when modelling non-Newtonian fluids. The effective viscosity is computed according to (4.76) that depends on the yield stress (4.54) and the mean scalar rate of strain $\dot{\gamma}$ (4.6).

4.6.2.3 Blending of shear forces

The continuous transition between solid and liquid state is ensured by the blending function ζ (4.83) defined in Section 4.5.3 (here again we omit the SPH particle labels):

$$\underline{f}_{\mathrm{g}} = \zeta\,\underline{f}_{\mathrm{g}}^{\mathrm{l}} + (1-\zeta)\underline{f}_{\mathrm{g}}^{\mathrm{s}} \tag{4.104}$$

where $\underline{f}_{\mathrm{g}}^{\mathrm{s}}$ and $\underline{f}_{\mathrm{g}}^{\mathrm{l}}$ are computed respectively through (4.98) and (4.102). Note that, here the blending applies to the forces instead of the stresses, even though (4.104) is not tantamount to (4.83) since ζ in not constant in space. However, the blending being a numerical trick to ensure a continuous transition, (4.104) can be used too. A simple way of getting (4.83) back would be to to use:

$$\left(\underline{f}_{\mathrm{g}}\right)_a = \underline{L}_a^E\{\zeta_b\,\eta_{\mathrm{eff},b},\,\underline{u}_b\} + \mathcal{G}\,\underline{L}_a^E\{(1-\zeta_b),\,\underline{X}_b\} + \underline{D}_a\{(1-\zeta_b)\,\underline{\underline{J}}_b\} \tag{4.105}$$

However, the differences between (4.104) and (4.105) were not investigated in this work.

4.6.3 Boundary conditions

4.6.3.1 Conditions at water–granular-material interface

In the frame of the multi-phase formulation presented in Section 3.2, the density and the pressure fields do not require any special treatment for the interaction of SPH particles of water $\mathcal{W}$ and of granular material $\mathcal{M}$. The density is computed according to (3.24) from all the neighbouring particles, irrespective of the fluid/phase ($\mathcal{W}$ or $\mathcal{M}$) they belong to. Besides that, both phases have a pressure field, so the pressure gradient is simply computed with the multi-phase gradient (3.25).

In regard to the shear forces, the two phases only interact though viscous effects for which Espanol and Revenga's [33] viscous term (3.31) is used in the two phases. In water, the granular material neighbours are seen as fluid particles having a viscosity η_{eff}. Thus the force density exerted by a particle b of granular material $\mathcal{M}$ on a particle a of water $\mathcal{W}$ reads:

$$\forall a \in \mathcal{W}, b \in \mathcal{M},$$
$$\left(\underline{f}_{\mathrm{w}}\right)_{b\to a} = \theta_b \overline{V}_b \frac{\eta_{\mathrm{w},a}\,\eta_{\mathrm{eff},b}}{\eta_{\mathrm{w},a}+\eta_{\mathrm{eff},b}}\Big[(d+2)\left((\underline{u}_a-\underline{u}_b)\cdot\underline{e}_{ab}\right)\underline{e}_{ab} + (\underline{u}_a-\underline{u}_b)\Big]\frac{\underline{\nabla} w_{ab}\cdot\underline{r}_{ab}}{r_{ab}^2} \tag{4.106}$$

where the subscript $_{\mathrm{w}}$ refers to the water and d is the space dimension. On the other hand, the viscous force density exerted by the water particle on the granular material contribute to the viscoplastic term in (4.104) through:

$$\forall a \in \mathcal{M}, b \in \mathcal{W},$$
$$\left(\underline{f}_{\mathrm{g}}^{\mathrm{l}}\right)_{a\to b} = \zeta\left[\theta_b \overline{V}_b \frac{\eta_{\mathrm{w},a}\,\eta_{\mathrm{eff},b}}{\eta_{\mathrm{w},a}+\eta_{\mathrm{eff},b}}\Big[(d+2)\left((\underline{u}_a-\underline{u}_b)\cdot\underline{e}_{ab}\right)(-\underline{e}_{ab}) - (\underline{u}_a-\underline{u}_b)\Big]\frac{\underline{\nabla} w_{ab}\cdot\underline{r}_{ab}}{r_{ab}^2}\right] \tag{4.107}$$

It should be noted that, since there is no contribution of the water neighbour the elastic-solid term in (4.104), the action-reaction principle is not respected when $\zeta < 1$. Indeed,

from the two latter equations, we can see that we only have:

$$\forall a \in \mathcal{M}, b \in \mathcal{W} \qquad \left(\underline{f}_{\mathrm{w}}\right)_{b\to a} = -\frac{1}{\zeta}\left(\underline{f}^{\mathrm{l}}_{\mathrm{g}}\right)_{a\to b} \tag{4.108}$$

Nevertheless, the strain rate of granular material particles close to the interface is usually high, due to the water particles velocity that contribute (4.88). Therefore, for particles in $\mathcal{M}$ having neighbours in $\mathcal{W}$, we usually have $\zeta \to 1$ so the action-reaction principle is respected most of the time. Despite that, (4.108) remains a weakness of the present model, and further investigation should be carried out to improve this aspect.

4.6.3.2 Conditions at wall–granular-material interface

Here two situations must be distinguished:

- The wall represents the boundary of the numerical domain, *i.e.* the wall is a virtual surface beyond which the material extends (physically): the elastic-viscoplastic constitutive equation and the failure criterion should be verified at the wall so we need boundary conditions for the elastic and viscoplastic forces.
- The wall represents a solid surface on which the granular material lies and slides: solid contact and friction laws must be used to represent the grain-wall interaction.

Elastic-viscoplastic wall boundary conditions Wall boundary conditions must enforced on both the viscoplastic term (4.103) and the elastic solid term (4.98). With regard to the former, the method presented in Section 2.5.2.3 for the viscous wall condition is simply applied. As regards the elastic solid term, the displacement of vertex $\mathcal{V}$ and boundary elements $\mathcal{S}$ et imposed to zero. We recall Espanol and Revenga's [33] boundary term:

$$\underline{L}_a^{E,\mathrm{bound}}\{1, \underline{X}_b\} = -\frac{1}{\Gamma_a}\sum_{s\in\mathcal{S}}\left(\underline{\underline{\nabla}}\,\underline{X}_a + \underline{\underline{\nabla}}\,\underline{X}_s\right)\cdot\underline{\nabla}\Gamma_{as} \tag{4.109}$$

As shown in Section 2.3.3 with (2.41), we can write:

$$\begin{aligned}\left(\underline{\underline{\nabla}}\,\underline{X}\right)_a\cdot\underline{e}_{as} &\approx \frac{\underline{X}_a - \underline{X}_s}{r_{as}}\\ \left(\underline{\underline{\nabla}}\,\underline{X}\right)_s\cdot\underline{e}_{as} &\approx \frac{\underline{X}_a - \underline{X}_s}{r_{as}}\end{aligned} \tag{4.110}$$

Thus, imposing $\underline{X}_s = \underline{0}$, Espanol and Revenga's [33] boundary term (4.109) can be approximated as:

$$\underline{L}_a^{E,\text{bound}}\{1, \underline{X}_b\} \approx -\frac{2}{\Gamma_a} \sum_{s\in\mathcal{S}} \underline{X}_a \frac{\underline{r}_{as} \cdot \underline{\nabla}\Gamma_{as}}{r_{as}^2} \tag{4.111}$$

The latter approximation is not exact because $\underline{\nabla}\Gamma_{as}$ is a vector oriented along the inward wall normal vector, not along $\underline{r}_{as}$.

Then, we assume a locally uniform distribution of $\underline{\underline{J}}$ at the walls (recall J is the time anti-derivative of the Jaumann tensor, as defined in Section 4.5.1). The corresponding boundary term reads:

$$\underline{D}_a^{\text{bound}}\{\underline{\underline{J}}_b\} = \frac{\overline{V}_a}{\Gamma_a} \sum_{s\in\mathcal{S}} \frac{1}{\overline{V}_s} \left(\underline{\underline{J}}_a - \underline{\underline{J}}_s\right) \cdot \underline{\nabla}\Gamma_{as} \tag{4.112}$$

The present assumption yields $\underline{\underline{J}}_s = \underline{\underline{J}}_a$, hence:

$$\underline{D}_a^{\text{bound}}\{\underline{\underline{J}}_b\} = \underline{0} \tag{4.113}$$

Similarly, we assume $\underline{\underline{J}}_b = \underline{\underline{J}}_a$ for vertex particles ($b \in \mathcal{V}$), thus the contribution of vertex particles to the volumic term also vanishes. The divergence of Jaumann rate finally simplifies to:

$$\underline{D}_a\{\underline{\underline{J}}_b\} = -\frac{\overline{V}_a}{\Gamma_a} \sum_{b\in\mathcal{F}} \theta_b \left(\underline{\underline{J}}_a - \underline{\underline{J}}_b\right) \cdot \underline{\nabla} w_{ab} \tag{4.114}$$

where the boundary terms vanished and the sum now only extends to free particles $\mathcal{F}$. Note that these boundary conditions will be used by default in Chapter 5, for cases involving granular materials.

Coulomb's friction wall boundary conditions If the wall represents a solid surface on which the granular material lies and slides, the previous boundary conditions may be unsuitable. No viscous nor elastic forces exert between the wall and the material. Instead, a repulsive contact force ensures the impermeability of the wall, and solid friction occurs between the grains and the wall. The contact forces is normal to the wall and corresponds the pressure forces that, within the scope of USAW boundary conditions, are already taken into account through the boundary term of the pressure gradient (3.25). Thus we do not need any additional force to represent the normal contact interaction.

The friction force can be derived adopting a similar approach. Following Violeau [119, p. 431] (see also [14, 63]) the contact force density can be written as:

$$\underline{f}_{\text{g},a}^{\text{cont}} = \frac{p_a}{\Gamma_a} \underline{\nabla}\Gamma_a \tag{4.115}$$

This force is oriented along $\underline{\nabla}\Gamma_a$ (*i.e.* it is normal to the wall as expected), and it depends on the particle pressure p_a. On the contrary, Coulomb's friction force should be tangential to the wall, and oriented backwards the slide direction. The velocity component tangential to the wall is oriented along the following vector:

$$\underline{t}_{as} = \frac{(\underline{u}_a - \underline{u}_w) - [(\underline{u}_a - \underline{u}_w) \cdot \underline{n}_s]\,\underline{n}_s}{|\,(\underline{u}_a - \underline{u}_w) - [(\underline{u}_a - \underline{u}_w) \cdot \underline{n}_s]\,\underline{n}_s|} \tag{4.116}$$

whith $\underline{u}_w$ the wall imposed velocity. Besides that, the friction force is proportional to the normal force exerted between the wall and the particle. We assume that the normal force is solely due the effective pressure acting on the contact surface. Thus we can write the friction force density as:

$$\underline{f}_{\mathrm{g},a}^{\mathrm{fric}} = -\frac{\mu\, p_{\mathrm{eff},a}}{\Gamma_a}\,|\underline{\nabla}\Gamma_a|\,\underline{t}_{as} \tag{4.117}$$

where μ the coefficient of kinematic friction. Using the definition of $\underline{\nabla}\Gamma_a$ (2.70) yields:

$$\underline{f}_{\mathrm{g},a}^{\mathrm{fric}} = -\frac{\mu\, p_{\mathrm{eff},a}}{\Gamma_a}\,|\sum_{s\in\mathcal{S}} \underline{\nabla}\Gamma_{as}|\,\underline{t}_{as} \tag{4.118}$$

To use this boundary condition, we enforce no elastic-viscoplastic interactions between the wall and granular material particles. Regarding the boundary terms, there are no more contributions from the boundary elements ($\mathcal{S}$):

$$\begin{aligned} \underline{D}_a^{\mathrm{bound}}\{\underline{\underline{J}}_b\} &= \underline{0} \\ \underline{L}_a^{E,\mathrm{bound}}\{1, \underline{X}_b\} &= \underline{0} \\ \underline{L}_a^{E,\mathrm{bound}}\{\eta_b, \underline{u}_b\} &= \underline{0} \end{aligned} \tag{4.119}$$

As regards the volumic terms, vertex particles should not contribute to elastic and viscoplastic forces. For elastic forces, Espanol and Revenga's [33] term thus reads:

$$\underline{L}_a^E\{1, \underline{X}_b\} = \frac{1}{\Gamma_a}\sum_{b\in\mathcal{F}} \theta_b \overline{V}_b \big[\,(d+2)\,((\underline{X}_a - \underline{X}_b)\cdot\underline{e}_{ab})\,\underline{e}_{ab} + (\underline{X}_a - \underline{X}_b)\,\big]\frac{\underline{\nabla} w_{ab}\cdot\underline{r}_{ab}}{r_{ab}^2} \tag{4.120}$$

and the divergence of Jaumann rate simplifies as:

$$\underline{D}_a\{\underline{\underline{J}}_b\} = -\frac{\overline{V}_a}{\Gamma_a}\sum_{b\in\mathcal{F}} \theta_b \left(\underline{\underline{J}}_a - \underline{\underline{J}}_b\right)\cdot\underline{\nabla} w_{ab} \tag{4.121}$$

Similarly, the viscoplastic plastic Espanol and Revenga's [33] term now reads:

$$\underline{L}_a^E\{\eta_b,\underline{u}_b\} = \frac{1}{\Gamma_a}\sum_{b\in\mathcal{F}}\frac{2\eta_a\eta_b}{\eta_a+\eta_b}\theta_b\overline{V}_b\big[\,(d+2)\,((\underline{u}_a-\underline{u}_b)\cdot\underline{e}_{ab})\,\underline{e}_{ab} + (\underline{u}_a-\underline{u}_b)\,\big]\frac{\underline{\nabla}w_{ab}\cdot\underline{r}_{ab}}{r_{ab}^2} \quad (4.122)$$

In the three previous equations where the sums only extend to free particles $\mathcal{F}$. Finally, the friction force density (4.118) is added to the grain shear force density (4.104):

$$\underline{f}_{\mathrm{g}} = \zeta\,\underline{f}_{\mathrm{g}}^{\mathrm{l}} + (1-\zeta)\underline{f}_{\mathrm{g}}^{\mathrm{s}} + \underline{f}_{\mathrm{g}}^{\mathrm{fric}} \quad (4.123)$$

Note that, from (4.118) we see vertex particles ($\mathcal{V}$) do not contribute to Coulomb's friction.

4.6.4 Algorithm and time-integration

The shear forces in the granular material are computed according to the following procedure:

1. p_{eff} is computed solving (4.64) with (4.85), (4.86) and (4.87)
2. $\underline{\underline{\dot{\gamma}}}$ and $\underline{\underline{\omega}}$ are computed from the previous velocity field using (4.88) and (4.89)
3. τ_{y} is computed from p_{eff} and $\dot{\gamma}$ using (4.54)
4. $\underline{\underline{\tau}}$ and $\underline{\underline{J}}$ both follow from the explicit time-integrations (4.91) and (4.99)
5. $\underline{f}_{\mathrm{g}}^{\mathrm{s}}$ is computed from $\underline{X}$ and $\underline{\underline{J}}$ with (4.98)
6. $\underline{f}_{\mathrm{g}}^{\mathrm{ss}}$ is computed from $\underline{f}_{\mathrm{g}}^{\mathrm{s}}$, $\tau_{\mathrm{g}}^{\mathrm{s}}$ and τ_{y} with (4.100)
7. η_{eff} is computed from τ_{y} and $\dot{\gamma}$ using (4.76)
8. $\underline{f}_{\mathrm{g}}^{\mathrm{l}}$ is computed from η_{eff} and the previous velocity field using (4.103)
9. ζ is computed from τ_{y} and $\dot{\gamma}$ using (4.83) and (4.78)
10. $\underline{f}_{\mathrm{g}}$ is computed from $\underline{f}_{\mathrm{g}}^{\mathrm{l}}$, $\underline{f}_{\mathrm{g}}^{\mathrm{ss}}$ and ζ with (4.104)

Time integration is done with a unique fully explicit symplectic method [37] for both the water and the granular material particles. That leads to the following time-integration scheme:

$$\begin{cases} \underline{u}_a^{(n+1)} = \underline{u}_a^{(n)} - \dfrac{\Delta t}{\rho_a^{(n)}} \underline{G}_a \left\{ p_b^{(n)} \right\} + \Delta t\, \underline{g} + \dfrac{\Delta t}{\rho_a^{(n)}} \underline{f}_a^{(n)} + \dfrac{\Delta t}{\rho_a^{(n)}} \Xi_a \left\{ p_b^{(n)} \right\} \\ \underline{r}_a^{(n+1)} = \underline{r}_a^{(n)} + \Delta t\, \underline{u}_a^{(n+1)} \\ \Gamma_a^{(n+1)} = \Gamma_a^{(n)} + \Delta t \left[(\underline{\nabla} \Gamma_a)^{(n+1)} \cdot \left(\underline{u}_a^{(n+1)} - \underline{u}_w^{(n+1)} \right) \right] \\ \rho_a^{(n+1)} = \Gamma^{(n+1)} \left[\Gamma^{(n)} \rho_a^{(n)} + \sum\limits_{b \in (\mathcal{F} \cup \mathcal{V})} m_b \left(w_{ab}^{(n+1)} - w_{ab}^{(n)} \right) \right] + \Lambda\Delta^{(n)} \end{cases} \tag{4.124}$$

Where, in the first equation, $\underline{f}$ refers to the shear forces. For granular material SPH particles $\underline{f} = \underline{f}_{\mathrm{g}}$, while for SPH particles of water $\underline{f} = \underline{f}_{\mathrm{w}}$, with:

$$\underline{f}_{\mathrm{w}} = \underline{L}_a^E \{ \eta_b, \underline{u}_b \} \tag{4.125}$$

where $\underline{L}_a^E$ is Espanol and Revenga's [33] second order operator (3.31):

$$\begin{aligned} \underline{L}_a^E \{ \eta_b, \underline{u}_b \} = \frac{1}{\Gamma_a} \sum_{b \in (\mathcal{F} \cup \mathcal{V})} \frac{2\eta_a \eta_b}{\eta_a + \eta_b} \theta_b \overline{V}_b \big[& (d+2) \left((\underline{u}_a - \underline{u}_b) \cdot \underline{e}_{ab} \right) \underline{e}_{ab} \\ & + (\underline{u}_a - \underline{u}_b) \big] \frac{\underline{\nabla} w_{ab} \cdot \underline{r}_{ab}}{r_{ab}^2} \\ & - \frac{1}{\Gamma_a} \sum_{s \in \mathcal{S}} \left(\eta_a \underline{\underline{\nabla}}\, \underline{u}_a + \eta_s \underline{\underline{\nabla}}\, \underline{u}_s \right) \cdot \underline{\nabla} \Gamma_{as} \end{aligned} \tag{4.126}$$

The pressure gradient $\underline{G}_a \{ p_b \}$ is computed using (3.25):

$$\begin{aligned} \underline{G}_a \{ p_b \} = \frac{1}{\Gamma_a \overline{V}_a} \sum_{b \in (\mathcal{F} \cup \mathcal{V})} \theta_b \left(p_a \overline{V}_a^2 + p_b \overline{V}_b^2 \right) \underline{\nabla} w_{ab} \\ - \frac{1}{\Gamma_a \overline{V}_a} \sum_{s \in \mathcal{S}} \frac{1}{\overline{V}_s} \left(p_a \overline{V}_a^2 + p_s \overline{V}_s^2 \right) \underline{\nabla} \Gamma_{as} \end{aligned} \tag{4.127}$$

The term $\Xi_a \{ p_b \}$ refers to the additional force used to avoid micro-mixing (3.32) presented in Section 3.2.3. Finally, the term $\Lambda\Delta$ in the last equation corresponds to the chequerboard effect correction presented in Section 2.6.

Chapter 5

Numerical results

Ce chapitre rassemble les résultats obtenus pour un ensemble de cas-tests visant à valider les développements présentés dans les chapitres précédents. Le modèle multiphasique de Hu and Adams [58] est d'abord validé sur un cas 2D d'écoulement de Poiseuille bi-fluide. Les résultats sont comparés à la solution théorique et un bon accord est trouvé. Le schéma d'intégration des forces visqueuses implicite est également validé avec succès sur ce cas. Le modèle multiphasique est ensuite appliqué à un cas expérimental de rupture de barrage où l'eau et l'air sont tous deux représentés. Les résultats de simulations sont également en très bon accord avec l'expérience. Le schéma implicite est testé avec succès sur un cas d'écoulement de Poiseuille pour un fluide de Bingham. Enfin, le modèle élastique-viscoplastique est appliqué à divers cas d'écoulements granulaires, dans le cas d'un matériaux sec ou saturé, ainsi qu'à des cas d'érosion et d'affouillement. À nouveau, les résultats sont globalement en bon accord avec l'expérience.

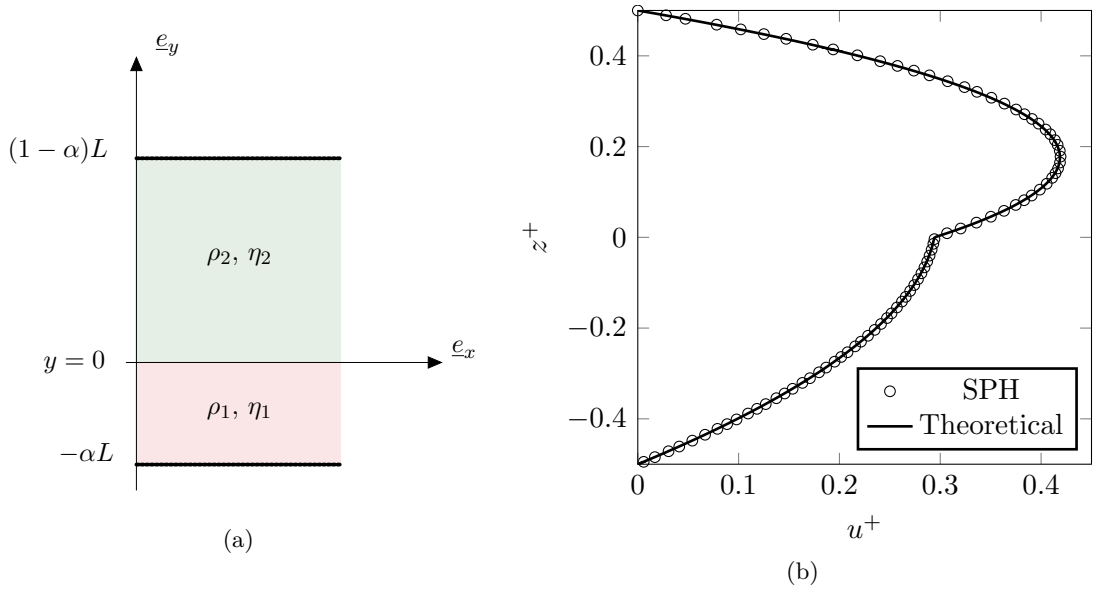

Figure 5.1: Bi-fluid Poiseuille flow – (a) Physical set-up. The coefficient α refers to the fraction of the channel width L occupied by the fluid 1 in the $z \leq 0$ region. (b) Horizontal velocity profile at the steady state for a Reynolds number of $Re_1 = 1.25$, with density and viscosity ratio of $\lambda = \omega = 4$ ($y^+ \leq 0 \Leftrightarrow$ fluid 1) and $\alpha = 0.5$. Morris et al.'s [86] viscous term is used and $L/\delta r = 384$. The black dots represent the SPH numerical result, while the solid line corresponds to the analytical solution (5.4).

In this chapter, the developments presented in the previous chapters are validated and applied to a number of cases. We first validate the multi-phase model presented in Chapter 3 on two cases that involve several Newtonian fluids. We then apply the model to a case of viscoplastic flow in order to ascertain the capability of the model to handle non-Newtonian flows. A case of dry granular flows is then studied so as to validate the elastic-viscoplastic model presented in Chapter 4. Finally, three cases involving interactions between water and granular material are studied.

5.1 Multi-phase flows

5.1.1 2D bi-fluid Poiseuille flow

The multi-phase formulation (3.33) presented in Section 3.2 is validated on a bi-fluid laminar plane Poiseuille flow in a closed channel, involving two fluids of different dynamic viscosities (η_1, η_2) and densities (ρ_1, ρ_2). The 2D flow is driven by a gravity force $\rho\underline{g}$ oriented in the direction of the flow along the x-axis. Periodic open boundaries are used and the height of the channel is $L = 1$ m. The interface between the two fluids is at $y = 0$,

the top wall is at $y = (1-\alpha)\,L$ and the bottom wall is at $y = -\alpha L$, where $\underline{e}_y$ denotes the transverse direction and α is the fraction of the channel width occupied by the fluid 1 (see Figure 5.1a). In the present work, the subscript 1 refers to the fluid in the bottom part ($y \leq 0$).

Our results are compared with the analytical solution that depends on the ratio between densities and kinematic viscosities, respectively denoted λ and ω:

$$\lambda = \frac{\rho_1}{\rho_2}, \quad \omega = \frac{\eta_1/\rho 1}{\eta_2/\rho_2} \tag{5.1}$$

We also define $\widetilde{u}_1$ a characteristic velocity of the flow and Re_1 the corresponding Reynolds number:

$$\widetilde{u}_1 = \frac{gL^2}{2\nu_1}, \quad Re_1 = \frac{\widetilde{u}_1 L}{\nu_1} = \frac{gL^3}{2\nu_1^2} \tag{5.2}$$

Finally, we define the following dimensionless variables:

$$y^+ = \frac{y}{L}, \quad u^+ = \frac{u_x}{\widetilde{u}_1}, \tag{5.3}$$

where $u_x = \underline{u} \cdot \underline{e}_x$. With these notations, the analytical solution u^+_{th} reads:

$$u^+_{\text{th}}(y^+) = \begin{cases} \alpha^2 - (y^+)^2 + \mathcal{A}(\alpha + y^+) & \text{if } \; y^+ \in [-\alpha; 0] \\ \omega\left((1-\alpha)^2 - (y^+)^2\right) + \lambda\omega\mathcal{A}\left(y^+ - (1-\alpha)\right) & \text{if } \; y^+ \in [0; 1-\alpha] \end{cases} \tag{5.4}$$

where $\mathcal{A}$ is a constant that depends on the geometric configuration and the physical parameters:

$$\mathcal{A} = \frac{(1-\alpha)^2\omega - \alpha^2}{(1-\alpha)\lambda\omega + \alpha} \tag{5.5}$$

Two configurations are studied here, with $Re_1 = 1.25$ and $Re_1 = 0.125$ respectively. The corresponding parameters are summarized in Table 5.1. We first compare the order of convergence obtained for the three viscous terms introduced in Section 2.3.3 ($Re_1 = 1.25$). Then we validate the implicit scheme (see Section 2.7.2) developed for Morris et al.'s [86] operator (3.29) choosing the lowest Reynolds number $Re = 0.125$. For the two cases, Brezzi and Pitkäranta's [15] chequerboard correction (2.99) was applied with a coefficient $\Lambda_{\text{BP}} = 0.1$, and no background pressure was used.

Comparison of viscous terms ($Re_1 = 1.25$) – Figure 5.1b shows the longitudinal velocity profile obtained using Morris et al.'s [86] viscous term (3.29), with $L/\delta r = 385$

SPH particles on the channel width. Numerical results are in excellent agreement with the analytical solution (5.4) represented by the solid line. Results obtained with Hu and Adam's [58] viscous term (3.27) and Espanol and Revenga's [33] one (3.31) also give such good qualitative results, thus demonstrating that the shear stresses at the wall and at the interface are correctly calculated by the present multi-phase model.

In order to validate further the multi-phase model, and to quantitatively compare the three viscous terms (3.29), (3.27) and (3.31), we performed a convergence study with the parameters summarized in Table 5.1a. For each simulation, velocity field is initialized to zero, the numerical solution converges to a steady-state (see Figure 5.2a) that is compared to the analytical solution (5.4) through the velocity instantaneous L_2 relative error E defined as follows:

$$E(t) = \sqrt{\frac{\left(\sum\limits_{b\in\mathcal{F}} \underline{u}_b(t) - \underline{u}_{\text{th}}(y_b,t)\right)^2}{\sum\limits_{b\in\mathcal{F}} \left(\underline{u}_{\text{th}}(y_b,t)\right)^2}} \tag{5.6}$$

where $\underline{u}_b$ is the particle velocity, $\underline{u}_{\text{th}}(y_b)$ the theoretical velocity at the position of particle b. The steady state is assumed to be achieved when the profile is fully developed. The characteristic time of the viscous effects propagation through the channel width L can be evaluated as $t_1 = L^2\rho_1/\eta_1$, from which we defined the dimensionless time $t^+ = t/t_1$. Figure 5.2a shows the instantaneous error with respect to the dimensionless time. We can see that the steady state is achieved at $t^+ \approx 1$, and that the solution remains stable afterwards. In order to have an objective measure of the error, independent from the small oscillations of the instantaneous error, we define the time-averaged error $\overline{E}$, computed from (5.6) as:

$$\overline{E} = \frac{1}{N_t}\sum_{i=1}^{N_t} E(t_i) \tag{5.7}$$

where $(t_i)_{i\in\{1..N_t\}}$ corresponds to the N_t iterations in the time interval $t^+ \in [1.5, 3.5]$ (grey region in Figure 5.2a).

Figure 5.2b shows the time-average error $\overline{E}$ with respect to the dimensionless particle size $\delta r/L$ (*i.e.* the inverse of the number of particles along the channel height). We see that the convergence slope of the present method using the three viscous terms is approximately of order 2 as long as $\delta r/L \leq 5\cdot 10^{-2}$. Afterwards, the convergence slope decreases for Morris et al.'s [86] and Hu and Adams' operators, while the error stabilized for Espanol and Revenga's [33] viscous term. These results are consistent with those obtained by [37] for one fluid SPH formulation with USAW boundary conditions, thus validating the present multi-phase model.

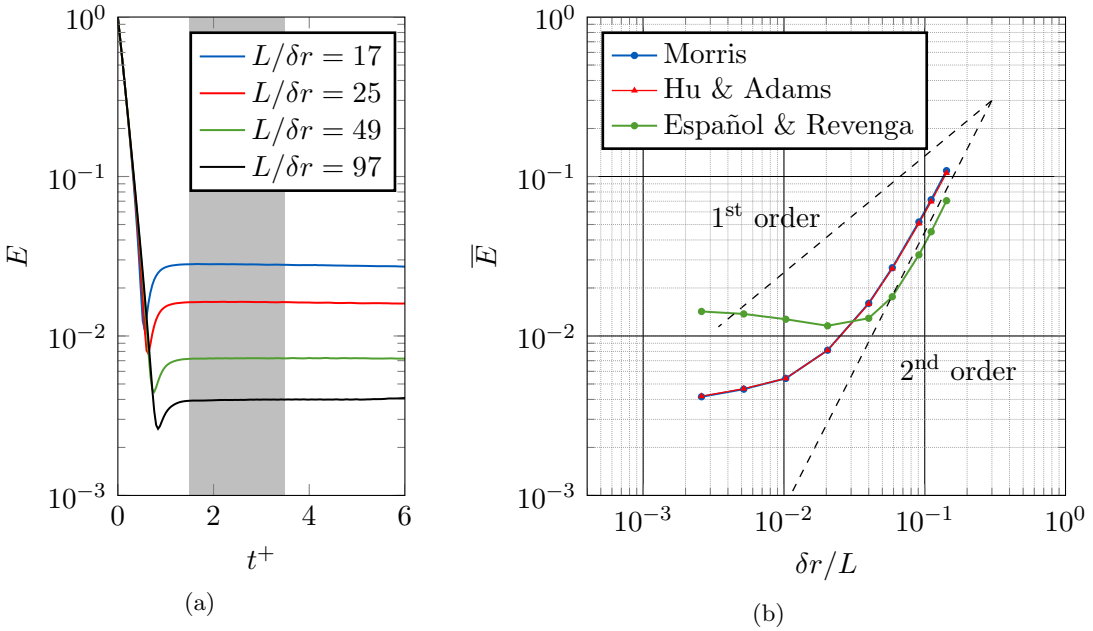

Figure 5.2: Bi-fluid Poiseuille flow $Re_1 = 1.25$ – (a) Evolution of the instantaneous L_2 relative error E with respect to the dimensionless time t^+. (b) Convergence graph of the present method comparing Morris et al.'s [86] (3.29), Hu and Adams' (3.27) and Español and Revenga's (3.31) viscous terms, for nine values of $\delta r/L$.

			$Re_1 = 1.25$		$Re_1 = 0.125$	
			Fluid 1	Fluid 2	Fluid 1	Fluid 2
Phys.	g	$[\text{m} \cdot \text{s}^{-2}]$	$4.0 \cdot 10^{-7}$	$4.0 \cdot 10^{-7}$	4	4
	ρ_0	$[\text{kg} \cdot \text{m}^{-3}]$	4000	1000	4	1
	η	$[\text{Pa} \cdot \text{s}]$	1.6	0.1	16	1
Num.	c_0	$[\text{m} \cdot \text{s}^{-1}]$	0.02	0.02	20	20
	P_{bg}	[Pa]	0	0	0	0
	ξ	-	7	7	7	7
	Λ_{BP}	-	0.1	0.1	0.1	0.1

Table 5.1: Bi-fluid Poiseuille flow – Physical and numerical parameters for both values of the Reynolds number, with $\omega = \lambda = 4$ and $\alpha = 0.5$.

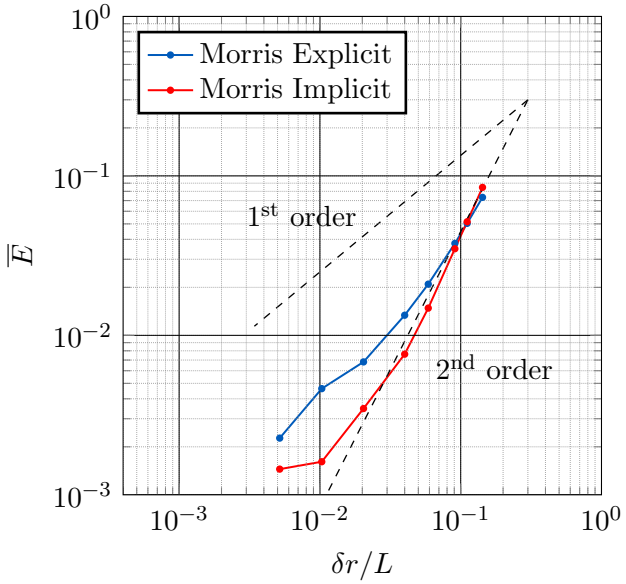

Figure 5.3: Bi-fluid Poiseuille flow $Re_1 = 0.125$ – Convergence graph of the present method comparing explicit and implicit viscous forces integration schemes, using Morris et al.'s [86] second order operator (3.29).

L/δ	Nbr. of particles	Scheme	Time	Speed-up
193	19000	Explicit	24500s	×6.125
		Implicit	4000s	
97	4900	Explicit	4330s	×2.9
		Implicit	1500s	

Table 5.2: Bi-fluid Poiseuille flow $Re_1 = 0.125$ – Comparison of simulation times for 2 s of physical time, for explicit and implicit viscous forces integration schemes.

Implicit Morris et al.'s [86] viscous term – Another convergence study is carried out with the Reynolds number $Re_1 = 0.125$ to validate the implicit integration scheme of Morris et al.'s [86] viscous term presented in Section 2.7.2. Parameters used for this configuration are summarized in Table 5.1b. Figure 5.3 also shows a second order convergence slope for both the explicit and implicit integration schemes, thus validating the implicit viscous term integration. Furthermore, from Table 5.2 we can see that the implicit scheme improves the code performance: for the most refined simulation ($L/\delta r = 193$), the implicit viscous forces integration scheme is more than six times faster than the explicit scheme for this Reynolds number.

5.1.2 2D air-water dam-break

The second test case is a 2D air-water dam-break flow impacting a vertical wall. The configuration corresponds to the experiment carried out by Lobovskỳ et al. [72] whose

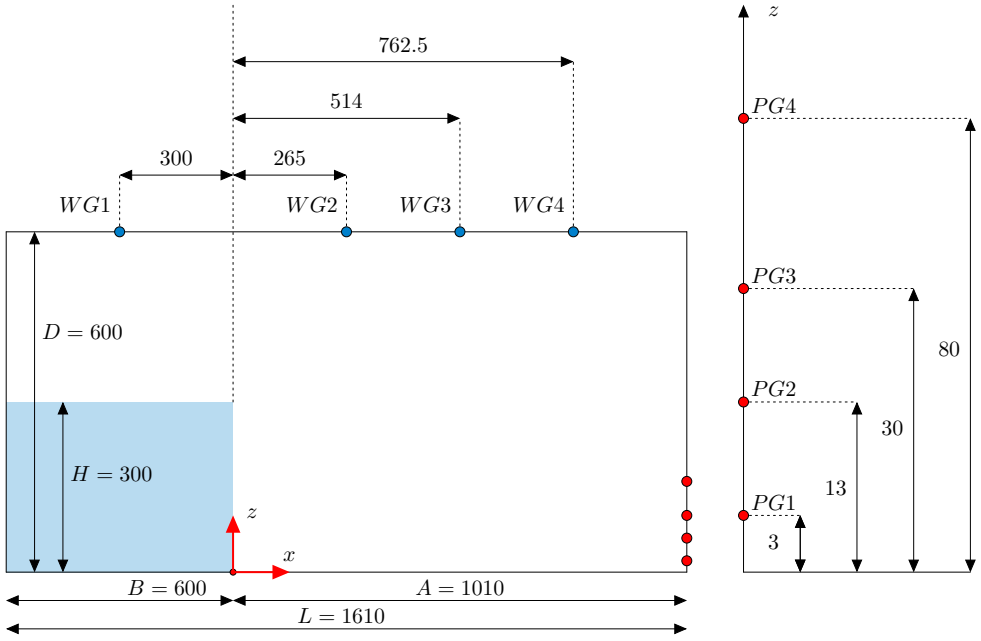

Figure 5.4: Air-water dam-break – Experimental set-up with dimensions in millimetres. Wave gauges (WG) measures the evolution of the water level at four horizontal locations. Four pressures gauges (PG) measures the pressure evolution on the impacted wall.

experimental set-up is illustrated in Figure 5.4. The physical and numerical parameters used for the simulations are summarized in Table 5.3. Results are presented in terms of dimensionless time t^+, water height h^+, water front horizontal position x_{F}^+, pressure p^+ and velocity u^+ defined by:

$$t^+ = \frac{t}{\sqrt{H/g}}, \quad h^+ = \frac{h}{H}, \quad x_{\mathrm{F}}^+ = \frac{x_{\mathrm{F}}}{H}, \quad p^+ = \frac{p}{\rho_{\mathrm{w}} g H}, \quad u^+ = \frac{u}{\sqrt{g\,H}} \tag{5.8}$$

where H is the initial water height, h is the current water height at a given x position, and x_{F} is the water front position. Simulations were carried out for two spatial discretizations $H/\delta r = 60$ and $H/\delta r = 120$.

Here too, Brezzi and Pitkäranta's [15] chequerboard correction (2.99) was applied (see Section 2.6.1). A coefficient of $\Lambda_{\mathrm{BP}} = 1$ was used in order to have a smooth pressure field despite the violent impact of the dam-break wave on the vertical wall. The $k-\epsilon$ turbulence model was also used here [65]. Note that the model was not adapted to the multi-phase framework. Thus the turbulent effects at air-water interface are probably not properly taken into account. However, the $k-\epsilon$ model is able to prevent numerical instabilities that are likely to occur within the air phase, and it leads to smoother pressure fields within the water. More details on this model can also be found in [67]. Finally, a

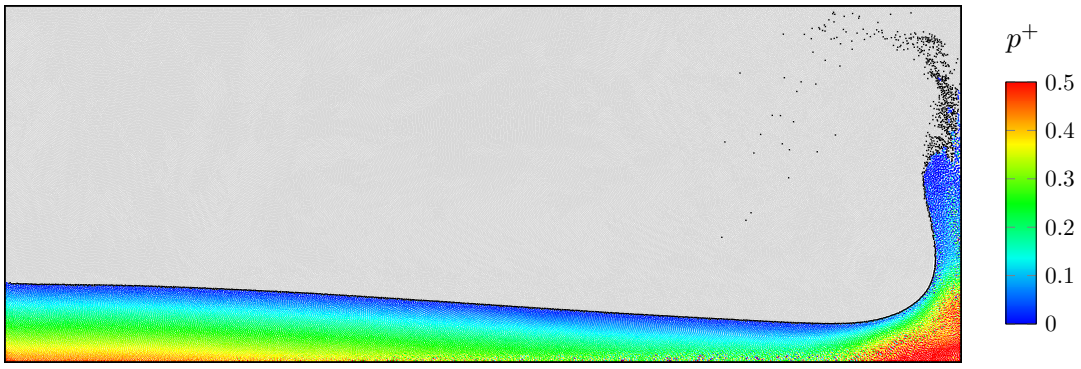

Figure 5.5: Air-water dam-break – Dimensionless pressure field p^+ in water at dimensionless time $t^+ = 4.5$ for $H/\delta r = 120$. The black particles corresponds to the air-water interface, the air SPH particles are represented in grey.

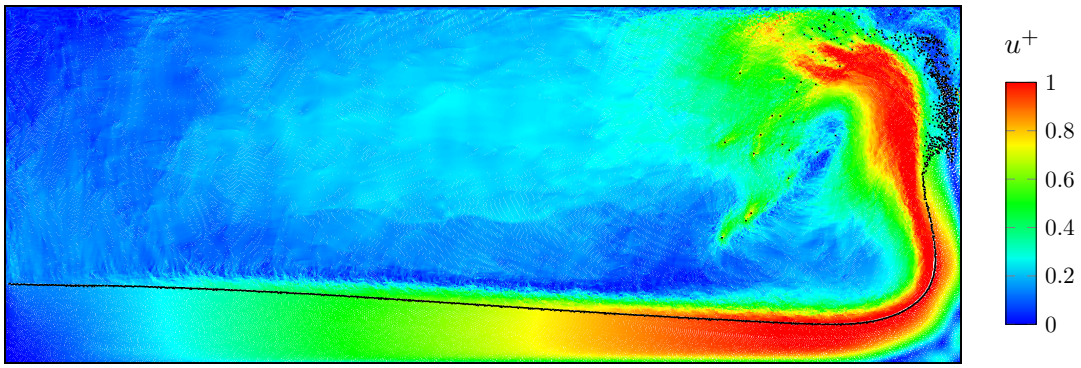

Figure 5.6: Air-water dam-break – Dimensionless norm of the velocity field u^+ in air and water at dimensionless time $t^+ = 4.5$ for $H/\delta r = 120$. The black particles corresponds to the air-water interface.

background pressure of 200 Pa was necessary to limit the unphysical void forming between air and water particles. A shifting algorithm has recently been proposed by [80] to prevent unphysical void formation and instability in the lighter phase when modelling high density ratio multi-phase flows with SPH. Although no shifting has been used here, Figures 5.5 and 5.6 show that, with the present model, a small background pressure is sufficient to prevent the unphysical void formation. Besides that, we can see in Figure 5.6 that the model ensures the continuity of velocity across the interface. On the other hand, Figure 5.5 shows that the pressure field is smooth and qualitatively satisfactory.

Wave gauges are used to measure the evolution of water level at four different locations. Figure 5.7 shows a comparison between the numerical results and the experimental measurements obtained for two experimental runs denoted $E01$ and $E02$. Some discrepancies can be noticed between the two experimental runs, especially after the breaking of the reflected wave ($t^+ > 7$) which makes Lobovskỳ et al. [72] question the repeatability of this part of the flow. Nevertheless, the water height predicted by the numerical model is in a very good agreement with the experiment for the four wave gauges, for the two tested

			Air	Water
Phys.	ρ_0	$[\mathrm{kg} \cdot \mathrm{m}^{-3}]$	1.184	997
	η	$[\mathrm{Pa} \cdot \mathrm{s}]$	$1.66 \cdot 10^{-5}$	$8.87 \cdot 10^{-4}$
Num.	c_0	$[\mathrm{m} \cdot \mathrm{s}^{-1}]$	34.3	147.5
	P_{bg}	[Pa]	200	200
	ξ	-	1.4	7
	Δ_{BP}	-	1	1
	$H/\delta r$	-	120	120

Table 5.3: Air-water dam-break – Physical and numerical parameters.

spatial discretizations. Some differences can also be noted after $t^+ > 7$ but the results are still satisfactory given the low repeatability mentioned above.

As regards the water front evolution, Figure 5.8 shows a comparison between the numerical results and two experimental data sets. The black solid line represent the current experimental data [72], while the black dashed line corresponds to a similar experiment carried out by Dressler [31] for a water height of 0.11 m. Again, some discrepancies can be noted between the two experiments, especially for $t^+ < 1$. According to Lobovskỳ et al. [72], these are probably due to the gate removal technique. Regarding the numerical simulation results, this argument must be borne in mind since the gate is not modelled at all here. Despite that, a satisfactory agreement with the experiment is found for the two tested spatial discretizations.

Finally, Figure 5.9 shows a comparison between the numerical results and Lobovskỳ et al.'s [72] experimental data for pressure gauges. The dashed black lines represent the experimental 2.5% and 97.5% percentile levels, estimated from 100 tests. The solid black line corresponds to an experimental representative impact event pressure while the solid red line corresponds to the numerical result obtained with the present multi-phase SPH model. We can see that, as regards the pressure, a refined simulation is necessary to obtain satisfactory results. For $H/\delta r = 60$, the pressure is globally overestimated is very noisy. For $H/\delta = 120$, a general good agreement is found except for the second pressure gauge $PG2$ for which the pressure peak is overestimated. Thus, the multi-phase model leads to satisfactory results, for the wave propagation as well as the pressure exerted on the impacted wall.

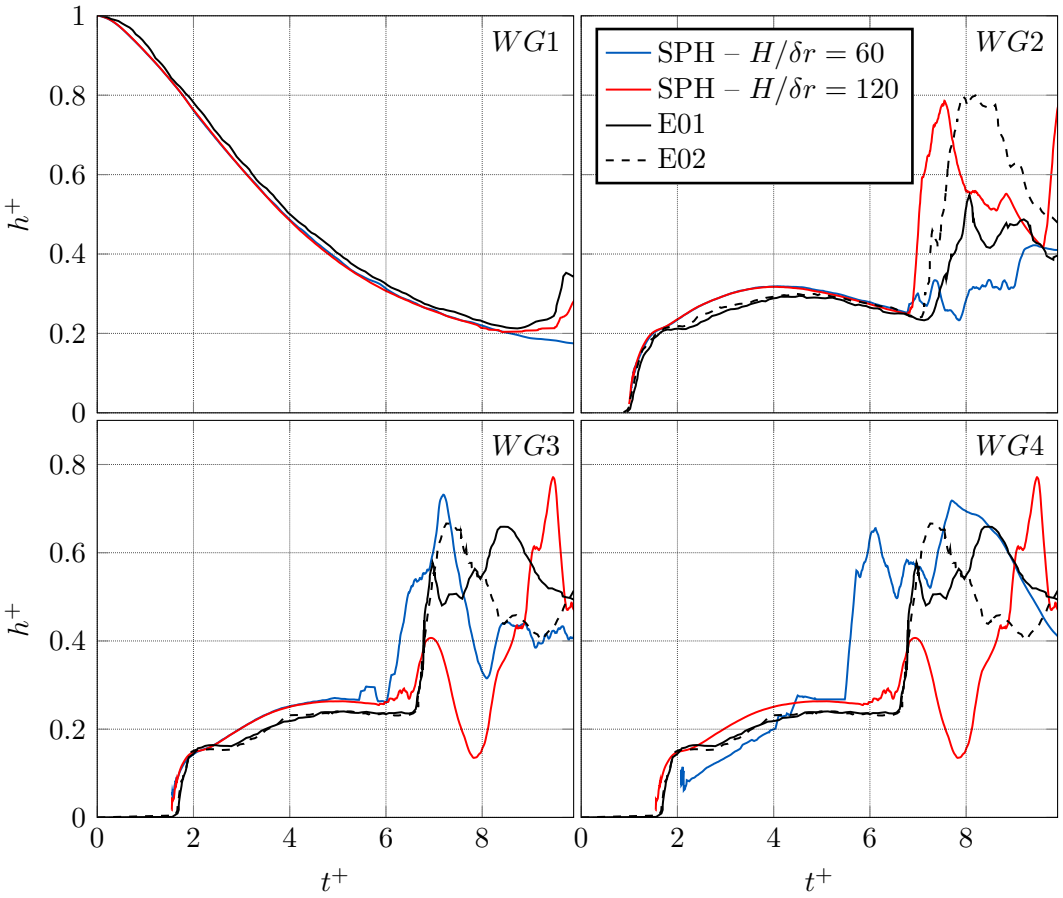

Figure 5.7: Air-water dam-break – Comparison of Lobovskỳ et al.'s [72] experimental water height measurements for two runs ($E01$ and $E02$) with the present numerical results.

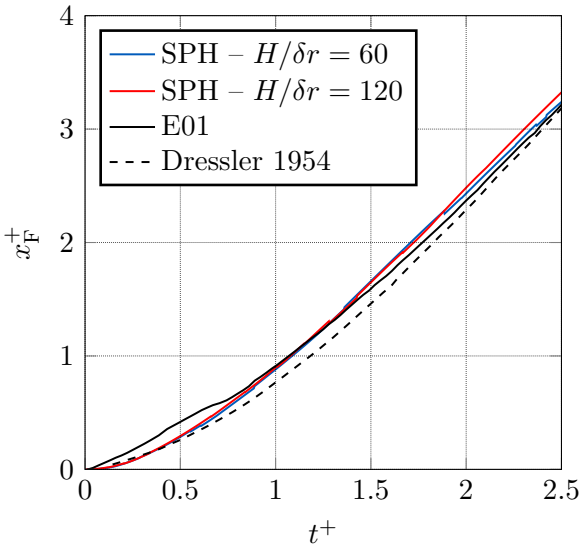

Figure 5.8: Air-water dam-break – Propagation of the water front predicted by the present multi-phase SPH model (red solid line) compared to Lobovskỳ et al.'s [72] (black solid line) and Dressler's [31] (black dashed line) experimental measurements.

5.2 Viscoplastic flows

5.2.1 2D Bingham Poiseuille flow

Our model is now applied to a Poiseuille flow involving a Bingham viscoplastic fluid. The 2D flow is driven by a gravity force $\rho \underline{g}$ oriented in the direction of the flow $\underline{e}_x$. Periodic open boundaries are used and the height of the channel is $L = 1$ m. A theoretical solution, referred to as (BN), can be found for the ideal Bingham model (4.5), but the SPH simulations are carried out using Papanastasiou's [94] regularized formula (4.13). The SPH solution is referred to as (SPH). The physical and numerical parameters used for this case are summarized in Table 5.4. From the physical properties of the fluid, we define the following dimensionless quantities:

$$y^+ = \frac{y}{L}, \quad u^+ = \frac{u_x \eta_\infty}{\rho_0 g L^2}, \quad Bn = \frac{\tau_y}{\rho_0 g L} \tag{5.9}$$

where Bn is the Bingham number that compares the yield stress τ_y to the stress resulting from the gravity force. With the above notations, the analytical solution u_{th}^+ reads:

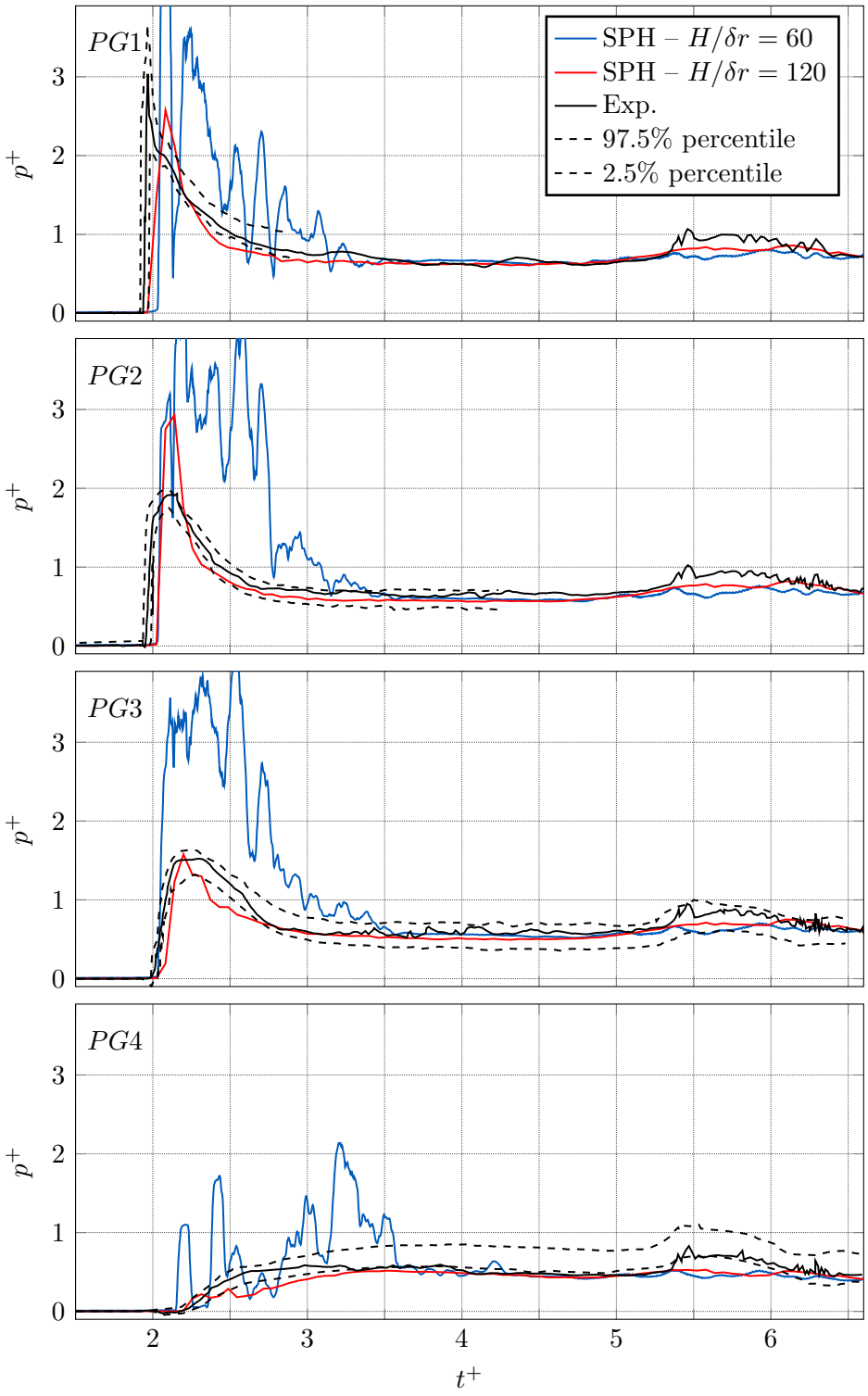

Figure 5.9: Air-water dam-break – Comparison of Lobovskỳ et al.'s [72] a representative experimental pressure measurements with the present numerical results. The lower and upper additional dashed lines represent the experimental estimated 2.5% and 97.5% percentile levels respectively.

$$\begin{cases} u^+_{\text{th}} &= \dfrac{1}{2}\left(\dfrac{1}{4} - (y^+)^2\right) - Bn\left(\dfrac{1}{2} + y^+\right) & y^+ \in \left[-\dfrac{1}{2}; -Bn\right] \\ u^+_{\text{th}} &= \dfrac{1}{8}(1-2Bn)^2 = u^+_{\text{PL}} & y^+ \in [-Bn; Bn] \\ u^+_{\text{th}} &= \dfrac{1}{2}\left(\dfrac{1}{4} - (y^+)^2\right) - Bn\left(\dfrac{1}{2} - y^+\right) & y^+ \in \left[Bn, \dfrac{1}{2}\right] \end{cases} \tag{5.10}$$

where u^+_{PL} is the dimensionless plug velocity, *i.e.* the dimensionless velocity of the rigid motion region located in $y^+ \in [-Bn; Bn]$. Note that if $Bn > 1/2$, the plug region reaches the solid boundaries of the channel, no flow can occur and the previous solution is not valid anymore. On the other hand, if $Bn = 0$, we simply get the one-fluid Poiseuille flow solution.

Comparing the simulation result to (5.10) may be irrelevant. Indeed Papanastasiou's [94] formula is only an approximation of Bingham's model, so we cannot expect to match exactly the theoretical solution. Thus we first use the computer algebra system Mathematica [59] to compute the profile corresponding to Papanastasiou's [94] formula, referred to as (PA), with the parameters summarized in Table 5.4. We can reasonably assume that the Mathematica solution (PA) is the best solution we can expect to approach with the SPH model, thus we use it as a reference solution.

To verify that Papanastasiou's formula is able to mimic the ideal Bingham behaviour, we first compare the Mathematica solution (PA) to the Bingham theoretical solution (BN). To so do, we define the relative error profile for any test T and reference R solutions as:

$$E_{\text{p}}(y^+) = \sqrt{\frac{\left(u^+_{\text{T}}(y^+) - u^+_{\text{R}}(y^+)\right)^2}{(u^+_{\text{PL}})^2}} \tag{5.11}$$

The solid black line in Figure 5.10b shows the error profile of the numerical Mathematica Papanastasiou's solution (PA) with respect to the theoretical Bingham solution (BN). As expected, most of the error is due to the plug region where (PA) leads to a highly viscous behaviour instead of a true rigid body motion.

The SPH solution can now be compared to the (PA) profile. Figure 5.10a shows a comparison of the two solutions and very good agreement is found. Though, we can see that the plug velocity is slightly overestimated by the SPH model. This can be clearly observed looking at the error profile of the SPH solution (dashed line) with respect to the Mathematica Papanastasiou's solution in Figure 5.10b: a sudden increase of error occurs in the plug region.

In order to characterize this error, we perform a convergence study for $Bn = 0.1$, with the parameters summarized in Table 5.1a. The implicit viscous forces integration scheme (see

Phys.	g	$[\mathrm{m}\cdot\mathrm{s}^{-2}]$	10
	ρ_0	$[\mathrm{kg}\cdot\mathrm{m}^{-3}]$	1
	η_∞	$[\mathrm{Pa}\cdot\mathrm{s}]$	1
	τ_y	[Pa]	1
	L	[m]	1
Num.	c_0	$[\mathrm{m}\cdot\mathrm{s}^{-1}]$	1
	P_bg	[Pa]	0
	m^P	s	10
	ξ	-	7
	Δ_BP	-	0.1

Table 5.4: Bingham Poiseuille flow – Physical and numerical parameters for $Bn = 0.1$.

Section 2.7.2) is used to deal with the large viscosity involved in this case. Similarly to the work done in Section 5.1.1, the velocity is initialized to zero. The converged numerical solution is then compared to the numerical (PA) solution, calculating the error according to (5.6) and (5.7). Figure 5.11 shows a convergence slope of order 3 which is unexpected and questionable. As a reminder, we previously found a second order convergence slope for the bi-fluid Poiseuille flow of Section 5.1.1 (Figures 5.2b and 5.3). Moreover, several authors also found a second order convergence slope within the USAW framework [37, 65]. This surprising result thus remains an open question. Despite that, the present model gives satisfactory results that demonstrates its ability to handle non-Newtonian flows.

5.3 Granular materials

5.3.1 Validation of elastic forces computation

This test case is a simple numerical experiment that aims at testing the improvement resulting from the computation of solid forces from the displacement field, *i.e.* using (4.97) instead of (4.93) (see Section 4.6.2.1 for a detailed description of the method). The quantity of interest is thus:

$$\underline{f} = \underline{\mathrm{div}}\left(\underline{\underline{\mathrm{grad}}}\ \underline{X} + \left(\underline{\underline{\mathrm{grad}}}\ \underline{X}\right)^T\right) \tag{5.12}$$

This is usually computed from the velocity field, integrating the strain rate tensor $\underline{\underline{\dot{\gamma}}}$ and using (4.93):

$$\underline{f}^U{}_a = \underline{D}_a\left\{2\,\underline{\underline{\dot{\gamma}}}^n + \Delta t\left(\underline{\underline{G}}_b\{\underline{u}_c\} + \left(\underline{\underline{G}}_b\{\underline{u}_c\}\right)^T\right)^n\right\} \tag{5.13}$$

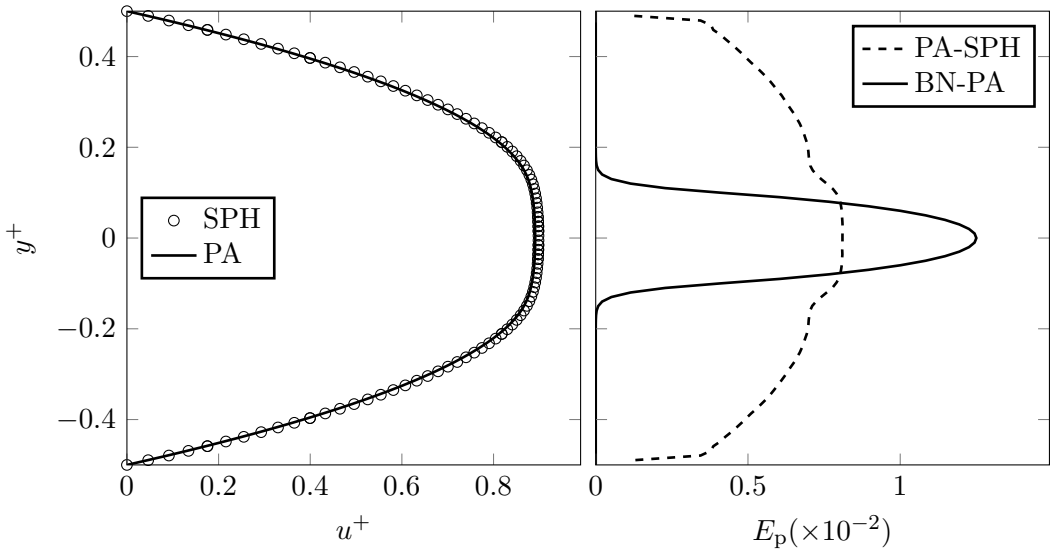

(a) (b)

Figure 5.10: Bingham Poiseuille flow – (a) Comparison of SPH (with $L/\delta r = 97$) and Mathematica velocity profiles for a Poiseuille flow involving a Bingham-like fluid modelled with Papanastasiou's [94] formula, for $Bn = 0.1$. (b) Profile of the error between the Mathematica solution profile obtained with Papanastasiou's [94] formula, and the theoretical ideal Bingham fluid solution (solid line); profile of the error between the Mathematica and SPH (with $L/\delta r = 97$) profiles obtained with Papanastasiou's [94] formula (dashed line).

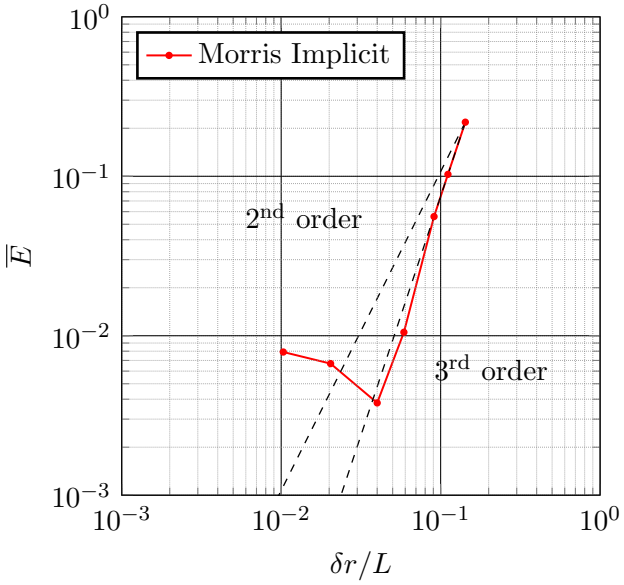

Figure 5.11: Bingham Poiseuille flow – Convergence graph of the present method. The error is calculated from the Mathematica reference solution.

The proposed alternative consists in calculating $\underline{f}$ from the displacement field $\underline{X}$ using Espanol and Revenga's [33] second order differential operator (2.78):

$$\underline{f}^{X}{}_{a} = \underline{L}^{E}_{a}\{1; \underline{X}_{b}\} \tag{5.14}$$

In order to compare the two approaches accuracy, we consider the periodic case of 2D Taylor–Green vortices for which the analytical velocity field is known:

$$\underline{u}\,(x,y,t) = \begin{pmatrix} -\cos\left(\frac{2\pi x}{L}\right)\sin\left(\frac{2\pi y}{L}\right) \\ \sin\left(\frac{2\pi x}{L}\right)\cos\left(\frac{2\pi y}{L}\right) \end{pmatrix} \exp\left(\frac{-2\eta t}{\rho}\right) \tag{5.15}$$

In order to quantify the error due to the SPH operators only, we consider a Cartesian grid of fixed SPH particles. Their velocity and corresponding theoretical displacement are imposed according to (5.15). The simulation is carried out for $L = 1$, $\eta/\rho = 0.1$ m^2·s^{-2} and $L/\delta r = 100$. After 10 s of physical time, expressions (5.13) and (5.14) are evaluated and compared to the exact value (5.12) obtained with Mathematica [59]. The comparison is performed calculating the error defined by:

$$E_a = \sqrt{\frac{(\underline{f}^{SPH}_{a} - f(x_a, y_a))^2}{\frac{1}{N}\sum\limits_{a\in\mathcal{F}} f(x_a, y_a))^2}} \tag{5.16}$$

where $\underline{f}^{SPH}{}_{a}$ is the quantity $\underline{f}$ calculated at particle a with SPH using either (5.13) or (5.14), $f(x_a, y_a)$ is the theoretical values calculated with Mathematica at the particle a position (x_a, y_a), and N is the total number of SPH particles. Results are plotted in Figure 5.12 that shows the error we got for both approaches. We clearly see that the error is much larger using (4.93), with a maximum error twice the one obtained using (4.97). This demonstrates the accuracy gain due to the use of a proper second order operator instead of two iterative uses of a first order operator within the scope of collocated methods.

5.3.2 2D soil collapse

To validate the elastic-viscoplastic present model, a simulation of an experimental 2-D collapse of dry soil is first carried out. The experiment was conducted by Bui et al. [16] and the experimental set-up is illustrated in Figure 5.13. The material is composed of aluminium bars of diameter 1 mm and 1.5 mm, length 50 mm and density 2650 kg·m^{-3}. The material porosity is not specified by the authors so we approximate it using the highest compact binary circle packing, leading to $\phi \approx 0.1$. Other physical parameters

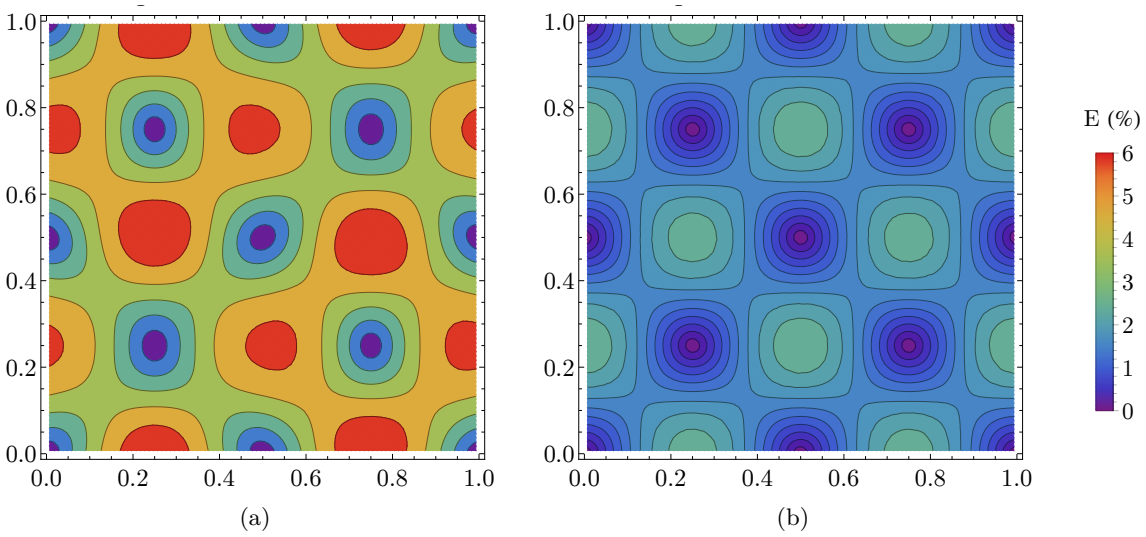

Figure 5.12: Taylor-Green vortices – Error on second order derivative of the displacement field in (a) calculated from strain rate tensor integration with (4.93) and in (b) calculated from displacement with (4.97). Results obtained for $L/\delta r = 100$ m and $\eta/\rho = 0.1$ m^2·s^{-2} after 10 s of physical time.

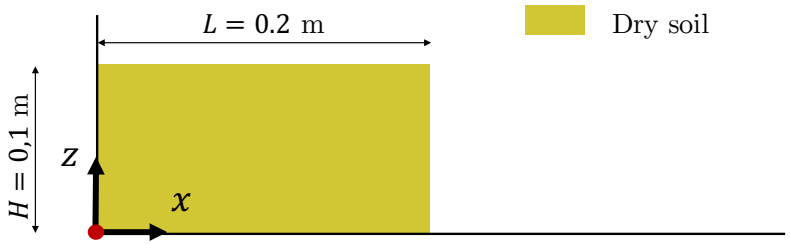

Figure 5.13: 2D Soil Collapse – Experimental set-up of Bui et al.'s [16] experiments.

were determined experimentally by Bui et al. [16] and are summarized in Table 5.5 (d_g being the diameter of the aluminium bars).

The simulations were performed using approximately 20,000 particles of soil and 1,400 vertex and boundary elements, with an initial particle spacing of $\delta r = 0.001$ m. In all simulations, the ratio between δr and the smoothing length h is $h/\delta r = 2$. The numerical speed of sound was set to 10 m·s^{-1}. Rhie and Chow's [101] chequerboard correction (2.99) was applied with a coefficient of $\Lambda_{RC} = 1.0$, and no background pressure was used.

Figure 5.14 shows the simulation result at four physical times. We see that (4.63) leads to a proper calculation of the yield stress, free of the typical SPH numerical oscillations of pressure. Besides, almost no deformation occurs between $t = 1.5$ s and $t = 2.0$ s, thus demonstrating that the model is able to represent the solid state even after a large time compared to the characteristic time of the experiment $\sqrt{H/g} = 0.1$ s. In Figure 5.15, the

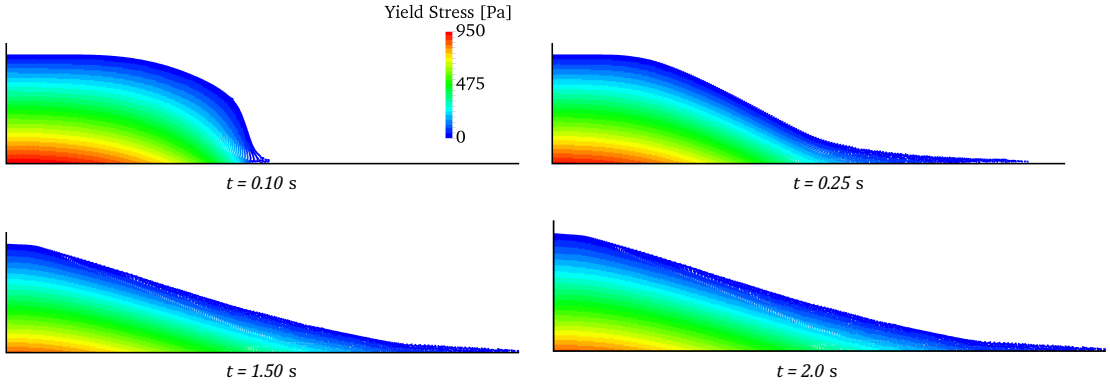

Figure 5.14: 2D Soil Collapse – Simulation results at $t = 0.1$s, $t = 0.25$s, $t = 1.5$s and 2.0 s.

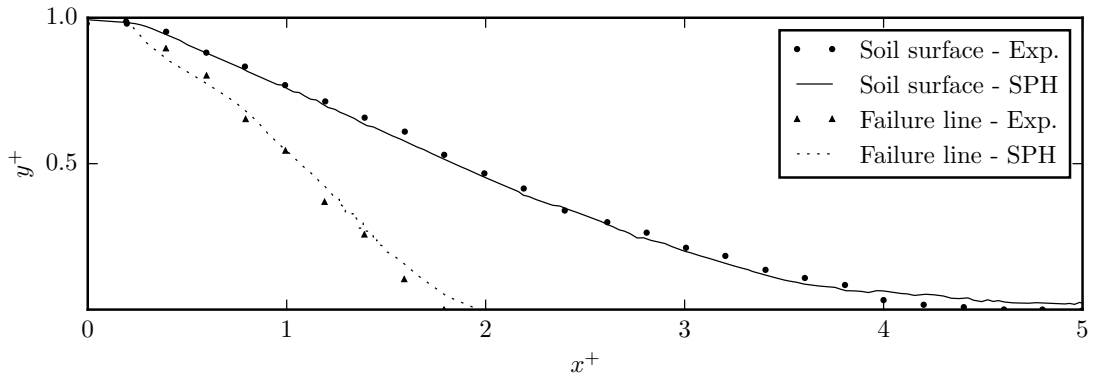

Figure 5.15: 2D Soil Collapse – Surface configuration and failure line at $t = 1.5$ s. Comparison of the present model to Bui et al.'s [16] experiments.

	ρ_g [kg/m^3]	d_g [mm]	ϕ [1]	E [Pa]	ν [1]	ψ [^{o}]
Al.	2650	$1.0 - 1.5$	0.10	$8.4 \cdot 10^5$	0.3	19.6

Table 5.5: 2D Soil Collapse – Physical parameters of the granular materials (aluminium bars).

	ρ_g [kg/m^3]	d_g [mm]	ϕ [1]	E [Pa]	ν [1]	ψ [^{o}]
Sand	2683	1.89	0.47	$8.0 \cdot 10^5$	0.3	30
PVC	1580	3.90	0.42	$8.0 \cdot 10^5$	0.3	38

Table 5.6: Dam-break wave on movable beds – Physical parameters of the granular materials.

surface configuration at the end of the experiment, as well as the failure line, are compared with numerical results obtained at 1.5 s. Experimentally, the failure line is defined as the line delimiting the non-deformed region. Numerically, we define the non-deformed region as the area where the displacement magnitude is less than the grain size, *i.e.* 1.5 mm. Both surface configuration and failure line are well predicted by the model.

5.4 Water-granular material interaction

5.4.1 2D dam-break wave on movable beds

The present model was also assessed to a case of dam-break wave propagating over a saturated granular bed. This study is based on the small-scale experiments carried out by Spinewine and Zech [104]. The experiments were performed in a flume being 25 cm wide and 6 m long. The initial configuration of the experiment is illustrated in Figure 5.16. The dam-break is initiated by the sudden lowering of a gate that is not taken into account in the simulation. Two materials (sand and PVC) are tested to investigate the capability of the model to exhibit different behaviours with respect to different materials. The physical

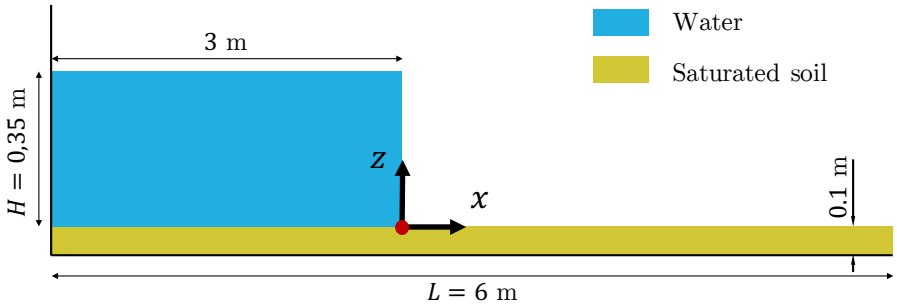

Figure 5.16: Dam-break wave on movable beds – Experimental set-up of Spinewine and Zech's [104] experiments.

parameters of the materials are summarized in Table 5.6. Note that experimental Young's modulus and Poisson's coefficient were available for these materials. Consequently, we used generic values from Ulrich [114] for similar cases. The first simulations were carried out setting a particle spacing of $\delta r = 0.002$ m, resulting in $525,000$ particles of water, $150,000$ particles of saturated soil and $13,000$ particles vertex and boundary particles. The numerical speed of sound and isentropic coefficient are set identically for the saturated granular material and the water, that is $c_0 = 37$ m·s^{-1} and $\xi = 7$. Rhie and Chow's [101] chequerboard correction (2.99) was applied with a coefficient of $\Lambda_{\text{RC}} = 1.0$, and no background pressure was used.

Figure 5.17 shows a comparison of the experiment and the SPH simulation carried out for the sand for $\delta r = d_{\text{g}}/2$. We can see that the dynamics of the flow is qualitatively well reproduced by the model. The free-surface and the sand-water interface seem to be more deformed in the SPH simulation though.

Total eroded mass of soil – First, let us focus on the total mass of sediments that reaches the downstream flume outlet. To do so, we define the relative error on the total eroded mass with respect to the experimental value:

$$Er = \frac{m_{\text{SPH}} - m_{\text{exp}}}{m_{\text{exp}}} \tag{5.17}$$

Figure 5.18 shows the error Er as a function of the ratio $\delta r/d_{\text{g}}$ (particle size/grain diameter). We can see that sand and PVC simulations exhibit similar behaviours although they have different grain sizes:

$$d_{\text{g}}^{\text{PVC}} \approx 2\, d_{\text{g}}^{\text{Sand}} \tag{5.18}$$

For the two materials, decreasing the SPH particle size improves the result until the critical value $\delta r = d_{\text{g}}$. Below this threshold, the soil model is no more valid and erosion is dramatically overestimated. This discretization limitation may be due to the fact that SPH particles are supposed to represent a macroscopic volume of the saturated soil. In other words, it is assumed that an SPH particle contains some grains and water. Therefore, an SPH particle should not be smaller than the grain size, otherwise the model would lead to deformations that do not occur in the real material, and overestimated strain rates. This is because the macroscopic elastic properties (*e.g.* Young's modulus) of the granular materials are very different from elastic properties of individual grains they are composed of [51]. Consequently, a particular attention must be paid to the discretization limitations when modelling granular materials with SPH. This might be avoided using alternative rheological laws or different elastic properties when $\delta r << d_{\text{g}}$. On the other hand, Figure 5.18 clearly shows that a sub-particle model would be necessary to correctly predict erosion when $\delta r >> d_{\text{g}}$. Within the scope of the present elastic-viscoplastic model,

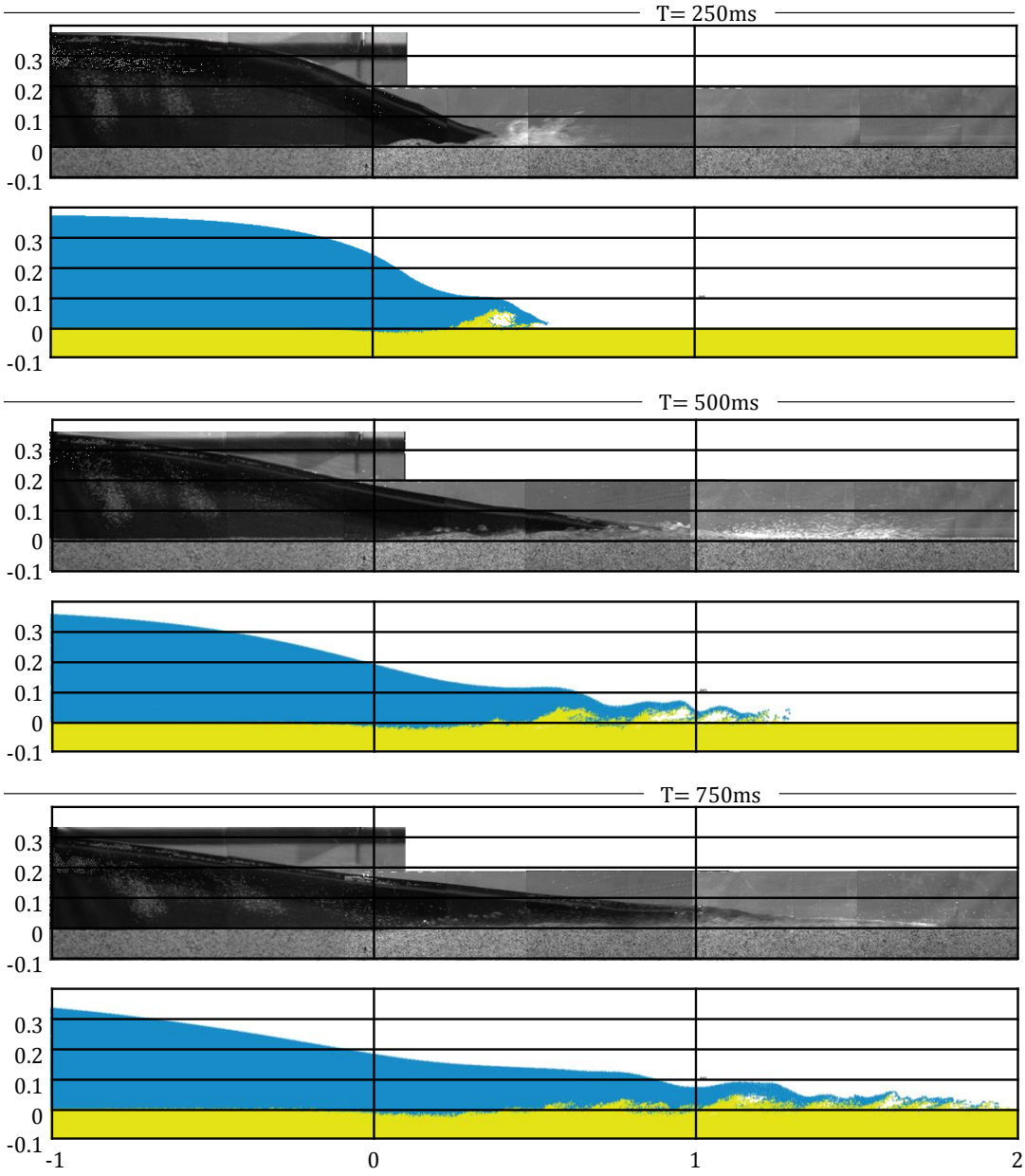

Figure 5.17: Dam-break wave on movable beds – Comparison of experimental and numerical results, with sand at time $t = 250$ ms, $t = 500$ ms and 750 ms, for $\delta r = d_g/2$.

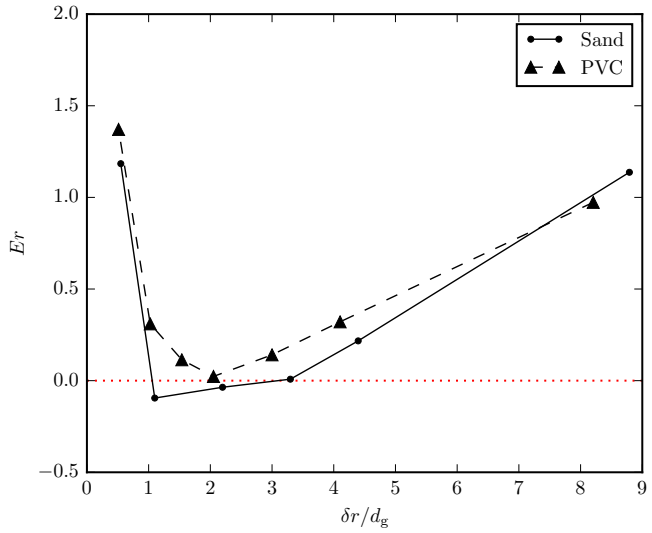

Figure 5.18: Dam-break wave on movable beds – Error on eroded mass as a function of the particle size/grain diameter ratio.

the problem depends on 10 physical parameters: the density ρ_w and dynamic viscosity of water η_w, the grain density ρ_g, the granular material porosity ϕ, the internal friction angle ψ, the Young's modulus E, the Poisson's coefficient, the grain size d_g, the gravity $\underline{g}$ and a characteristic length of the problem L. Applying the Buckingham π theorem, we obtain 7 dimensionless parameters that characterize this problem:

$$\phi, \quad \frac{\rho_g}{\rho_w}, \quad \psi, \quad \nu, \quad Re = \frac{g^{1/2} L^{3/2} \rho_w}{\eta_w}, \frac{d_g}{L}, \quad \frac{E}{d_g \left(\rho_g - \rho_w\right) g} \tag{5.19}$$

In a way, using $\delta r < d_g$ amounts to setting $d'_g \approx \delta r$. We would then have SPH particles being solid matter while other are viscoplastic. The latter two dimensionless numbers are thus modified as:

$$\frac{\delta r}{L}, \quad \frac{E}{\delta r \left(\rho_g - \rho_w\right) g} \tag{5.20}$$

Regarding the first one, the decrease of the grain size has probably no influence on the results since we have $\delta r/L << 1$ as well as $d_g/L << 1$. However we see that the second dimensionless number is significantly changed. Recovering its physical value can be done by changing Young's modulus: when $\delta r = \alpha d_g$ with $\alpha < 1$, we would set the Young's modulus to αE. However, this was not tested in the scope of this thesis.

In Figure 5.18 we see that an optimum seems to be achieved for $\delta r \in [d_g; 3d_g]$ for both sand and PVC. However, it must be pointed out that $\delta r > 3d_g$ is a coarse spatial discretization for this problem (≈ 22 particles on the water height). Thus, the error due to the hydrodynamics solver is also probably partly responsible on the erosion overestimation. Note that

erosion is overestimated for almost all configurations. Thus, at worst, simulations give a superior limit of the real erosion.

In the following, results are presented for $\delta r \approx 2d_{\mathrm{g}}$, *e.g.* for the sand, simulations were carried out setting a particle spacing of $\delta r = 0.004$ m, resulting in $130,000$ particles of water, $38,000$ particles of saturated soil and $3,000$ particles vertex and boundary particles.

Flows interfaces – Figure 5.19 shows the interface between moving and motionless sediment (black), the water-sediment interface (blue) and the water free-surface (red) for the sand. The interface between the motionless and the moving sediment is defined in line with the experimental detection method. In the experiment, a camera set to 200 images per second (*i.e.* one image every $\Delta t = 5$ ms) was used to acquire image sequences of the flow. Every image was then subtracted to the preceding image. The black region in the resulting image was defined as the motionless region. Given that the spatial resolution for one pixel is approximately $\Delta x = 1$ mm [104], we define a threshold velocity below which the sediment SPH particle is considered as motionless:

$$u_{\mathrm{motion}} = \frac{\Delta x}{\Delta t} \tag{5.21}$$

Continuous lines represent the numerical results while experimental data are represented as dotted lines. A general good agreement is obtained for the sand bed. Interfaces as well as free-surface and water front are well predicted for the five considered times. Figure 5.21 shows a comparison of flow interfaces for $\delta r = 2d_{\mathrm{g}}$ (solid lines) and $\delta r = d_{\mathrm{g}}/2$ (dashed lines). We clearly see that having SPH particles smaller that the grain size (dashed lines) leads to overestimated bed deformations while the results obtained for $\delta r = 2d_{\mathrm{g}}$ (Figures 5.19 and 5.21) match the experimental data.

For the PVC bed, Figure 5.20 shows that the initial liquefaction is slightly underestimated. In particular, the experimental bed profile (*i.e.* the black dotted line) at $t = 250$ ms is deeper than the numerical one. This may be due to the fact that the lowering of a gate is not taken into account in the simulation. Moreover, there is a large uncertainty on PVC beds elastic properties. Indeed, elastic properties of sand are widely used in soil mechanics and a lot of experimental data is available. We did not find such data for PVC soils, hence the differences between numerical and experimental results. Nevertheless, simulations give good results for the PVC too. In addition, they exhibit very different behaviours for sand and PVC, demonstrating the capability of the model to account for different material properties.

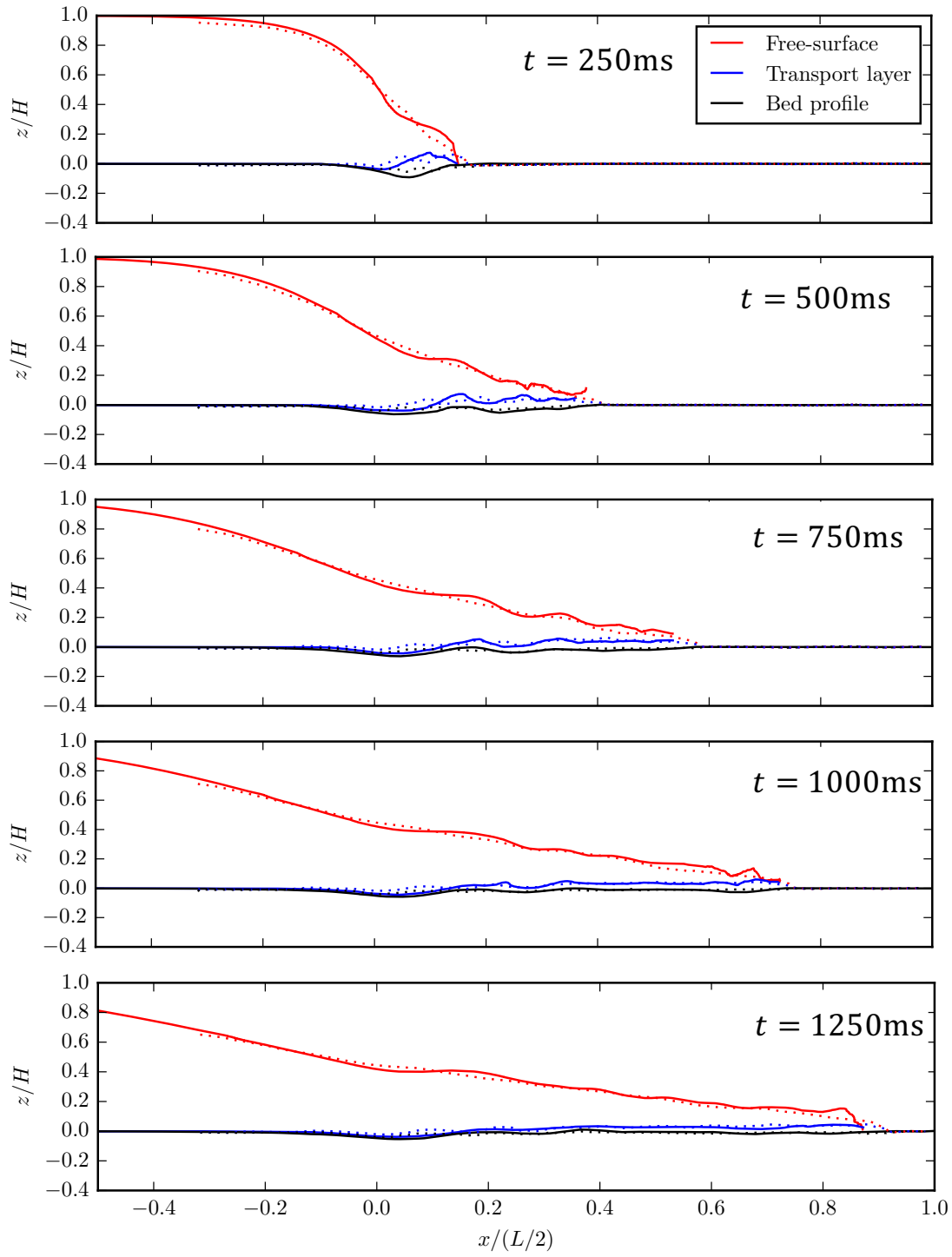

Figure 5.19: Dam-break wave on movable beds – Comparison of experimental (dotted lines) and numerical results (solid lines), with sand at time $t = 250$ ms, $t = 500$ ms, $t = 750$ ms, $t = 1000$ ms and $t = 1250$ ms, for $\delta r = 2d_g$.

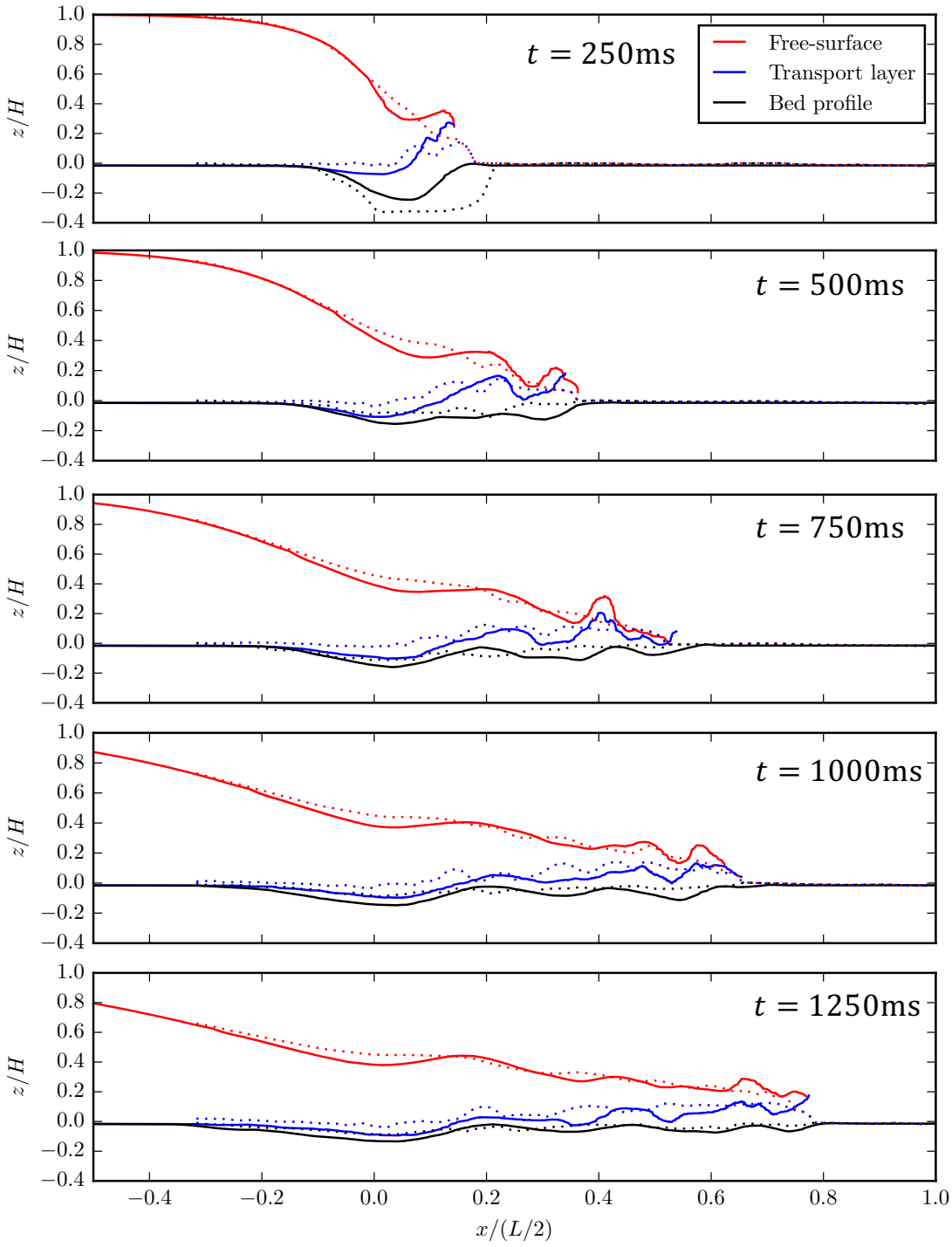

Figure 5.20: Dam-break wave on movable beds – Comparison of experimental (dotted lines) and numerical results (solid lines), with PVC at time $t = 250$ ms, $t = 500$ ms, $t = 750$ ms, $t = 1000$ ms and $t = 1250$ ms, for $\delta r = 2d_g$.

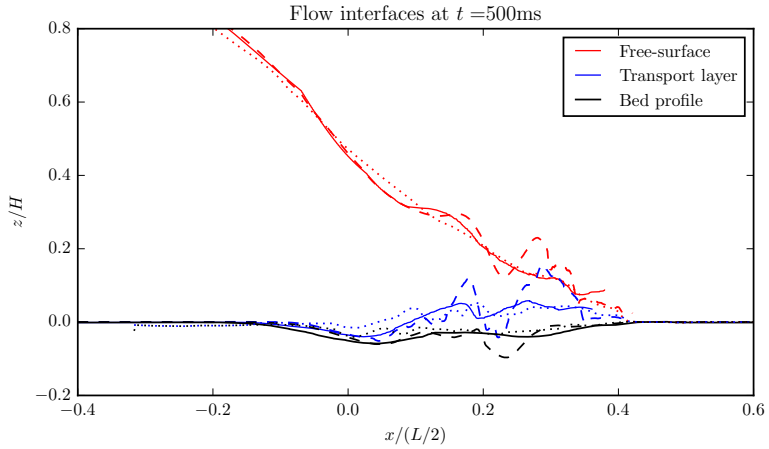

Figure 5.21: Dam-break wave on movable beds – Comparison of experimental (dotted lines) and numerical results, with sand at time $t = 500$ ms, for $\delta r = d_g/2$ (dashed lines) and $\delta r = 2d_g$ (solid lines).

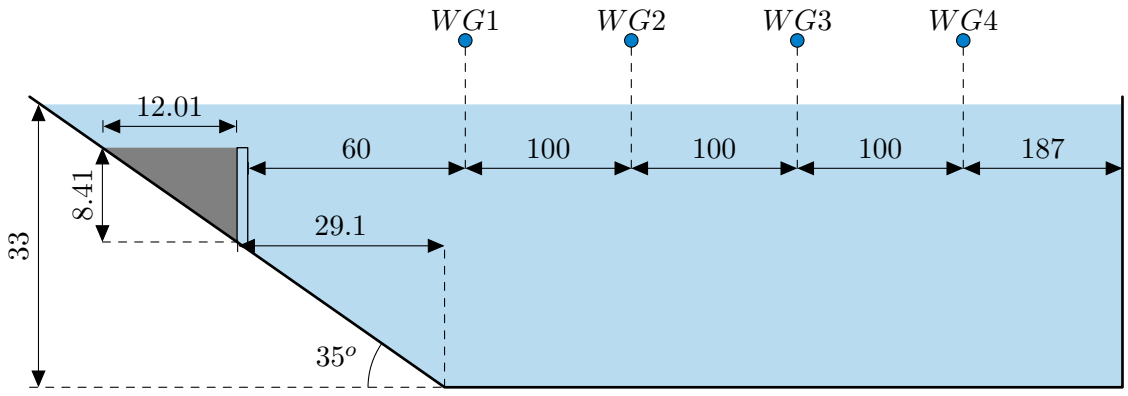

Figure 5.22: 2D Soil Collapse – Experimental set-up of Grilli et al.'s [50] experiments.

	ρ_g [kg/m^3]	d_g [mm]	ϕ [1]	E [Pa]	ν [1]	ψ [^{o}]
Glass beads	2500	4	0.366	$8.0 \cdot 10^5$	0.3	24

Table 5.7: Submarine Landslide – Physical parameters of the granular material.

5.4.2 2D submarine landslide

The present model is now applied to the simulation of a submarine landslide induced wave problem. This study is based on the experiment carried out by Grilli et al. [50]. A $W = 2$ kg mass of glass beads is initially placed in a triangular reservoir under water, on an 35^o inclined slope, fronted by a sluice gate. The experimental set-up is illustrated in Figure 5.22. At initial time, the gate is withdrawn into a bottom cavity within the slope. Wave gauges are used to measure the evolution of water level at four different locations.

The physical parameters of the materials are summarized in Table 5.7. In this case as well as the previous one, experimental Young's modulus and Poisson's coefficient were not available for the glass beads. Thus, similarly to the dam break over mobile bed case (Section 5.4.1), generic values were used. The experimental internal friction angle ψ value was not given neither, so we chose it by a trial and error approach. The simulations were carried out setting a particle spacing of $\delta r = 0.002$ m, resulting in $42,000$ particles of water, $1,200$ particles of saturated soil and $6,000$ particles vertex and boundary particles. The numerical speed of sound and isentropic coefficient are set identically for the saturated granular material and the water, that is $c_0 = 20$ m$\cdot$s^{-1} and $\xi = 7$. Rhie and Chow's [101] chequerboard correction (2.99) was applied with a coefficient of $\Lambda_{RC} = 1.0$, and no background pressure was used (as in all free-surface simulations).

The first simulations were carried out with the default elastic-viscoplastic boundary condition (EV-BC) presented in Section 4.6.3.2. Figure 5.23 shows a comparison of experimental surface elevation at the four wave gauges, with two SPH simulations. The green line corresponds to the case in which the gate withdrawing is not taken into account. In that case, the wave amplitude is largely underestimated at every gauges. Moreover, the simulation does not reproduce the second peak on gauge $WG1$. Apart from the amplitude, the overall shape of the generated wave is satisfactory until $t = 6$ s. Afterwards, we observe a significant phase change in the numerical results. The red line in Figure 5.23 is obtained modelling the withdrawing of the gate, assuming a constant opening velocity. We can see that the gate has a significant effect on the wave amplitude. This result is not too surprising since the gate is 1 cm wide, while the slide submergence is only of 4.22 cm. As a consequence, the volume of water displaced by the sudden gate withdrawing necessarily impacts the water height locally, and accentuates the wave resulting from the slide motion. Thus, from now on, the gate is always taken into account. Nevertheless, the wave amplitude obtained modelling the gate removal is still underestimated.

It should be observed, in this case, the wall represents a solid surface on which the granular material lies and slides. Thus, no viscous nor elastic forces exert between the wall and the material and the default elastic-viscoplastic boundary conditions (EV-BC) are inadequate. Indeed, the region of the slide that is close to the wall is also the region where the deformations are the slowest, *i.e.* the strain rate is very small in this region. As a consequence, either the blending function (see (4.83), Section 4.5.3) tends to 0 and elastic forces exert between the slide and the wall, or the effective viscosity is very large and the slide base flows very slowly. In both cases, the slide sticks to the wall, and the mass of granular material that effectively falls is artificially decreased. This phenomenon can be observed in Figure 5.24a. Therefore, the Coulomb's friction wall boundary condition (CF-BC, Section 4.6.3.2) must be tested here.

With this model, the wall-slide interaction is modelled through a dynamic solid friction law. The friction coefficient μ must also be determined by a trial and error approach since no experimental value is available. Thus, we choose to calibrate μ so that the simulation falling time (*e.g.* the time necessary for the slide to reach the flat bed) matches the experimental one. Unfortunately, the simulation falling time is always overestimated by the model. As an illustration, Figures 5.24b and 5.24c show the slide cross section at $t = 0.47$ s for $\mu = 0.5$ and $\mu = 0$ (*i.e.* a free-slip condition), and both simulations exhibit an important delay. That means that even with no friction between the slide and the bed, the granular material moves too slowly.

With $\mu = 0$, the only remaining slowing down factor is the drag exerted by the water. Thus in that case, the model overestimates either the viscous drag or the pressure drag (or both). Figure 5.24d shows the slide cross section at $t = 0.47$ s, for $\mu = 0$ and no viscous forces exerted between the slide and the water. An important delay is still observed, which demonstrated that the viscous drag is not responsible for the slide slowing down. Therefore, we can conclude that the model overestimates the pressure drag. This is confirmed by Figure 5.24e showing a simulation with no water within the tank. The only remaining difference between Figures 5.24d et 5.24e are the pressure forces exerted by the slide and the water on each other, pointing out that the pressure drag is responsible for the slide slowing down.

Another argument corroborates this conclusion. The viscous drag has a dominant effect at low Reynolds numbers, *i.e.* when the relative velocity between the slide and the water is small. Thus overestimating the viscous drag should slow down the slide when it starts to collapse, and still has a small velocity. Figure 5.26 shows the slide cross section evolution for the simulation with water-slide viscous forces and $\mu = 0.5$. We can see that the delay is almost not noticeable until $t = 0.32$ s while it is very important at $t = 0.47$ s. Therefore, as long as the viscous drag is dominant (*i.e.* the slide-water relative velocity remains low), the slide collapse is well represented by the model. When the slide velocity increases, the pressure drag becomes dominant, the model overestimates it and the slide is non-physically

slowed down.

This pressure drag overestimation is probably due to the fact that the present model is not able to represent the water flow through the granular material, nor the grain concentration variations. Thus, in the simulation the slide behaves as a impermeable volume that water has to bypass, while the physical slide is in reality a porous media whose porosity is not constant in time, and that allows seepage.

In Figure 5.25, the experimental surface elevation is compared to the simulation results obtained with the elastic-viscoplastic boundary condition (EV-BC) and the Coulomb's friction boundary condition with $\mu = 0.5$ (CF-BC). We see that using (CF-BC) globally increases the predicted wave amplitude. The first wave is overestimated at all gauges, while the next ones are satisfactorily predicted (except at $WG1$) until $t = 6$ s. The observed discrepancies at $WG1$ suggests that the acceleration of the slide in the very first moments of the collapse might be inaccurately reproduced by the model [53, 55].

In conclusion, the model is able to qualitatively reproduce the submarine landslide and the induced wave. However, several numerical parameter calibrations were necessary, *i.e.* the internal friction angle ψ and the friction coefficient μ. The constant grain concentration hypothesis and the absence of porous flow within the slide seem to lead to an an overestimation of the pressure drag, which is responsible for the non-physical slow down of the slide after $t \approx 0.32$ s. That delay might explain the poor surface elevation results obtained after $t = 6$ s. Finally, it should be pointed out that Lo and Liu [71] recently showed that "the area enclosed by the landslide has stronger lasting effects on the generated water waves than the exact landslide shape; in experiments and numerical simulations it is therefore more important to match the enclosed area and the characteristic landslide scales than the exact shape". Waves generated by landslides are thus not the most relevant cases to validate granular material constitutive equations. The water-slide and wall-slide friction seem to be the most important parameters to correctly reproduce the generated waves. Surface elevation obtained by Grilli et al. [50], modelling the slide as a heavy Newtonian fluid, are much better than those we obtain here. On the contrary, the slide shape evolution predicted by the elastic-viscoplastic model (Figure 5.26) is more realistic than the one obtained with Grilli et al.'s [50] heavy Newtonian fluid model.

5.4.3 3D Tsunami scour around a square structure

We finally apply the model to a 3D case of tsunami-induced local scour around a structure with a square cross-section. This study is based on the experiment carried out by Nakamura et al. [88]. The experimental set-up is illustrated in Figure 5.27. A solitary wave is generated in a 0.7 m wide channel, propagate on 6.9 m (5 m of flat bed, 1.9 m of 1/10 slope) and impacts the square cross-section structure. The structure relies on a sand foundation that is contained in a rigid reservoir. The reservoir is filled with $h_s = 15$ cm of

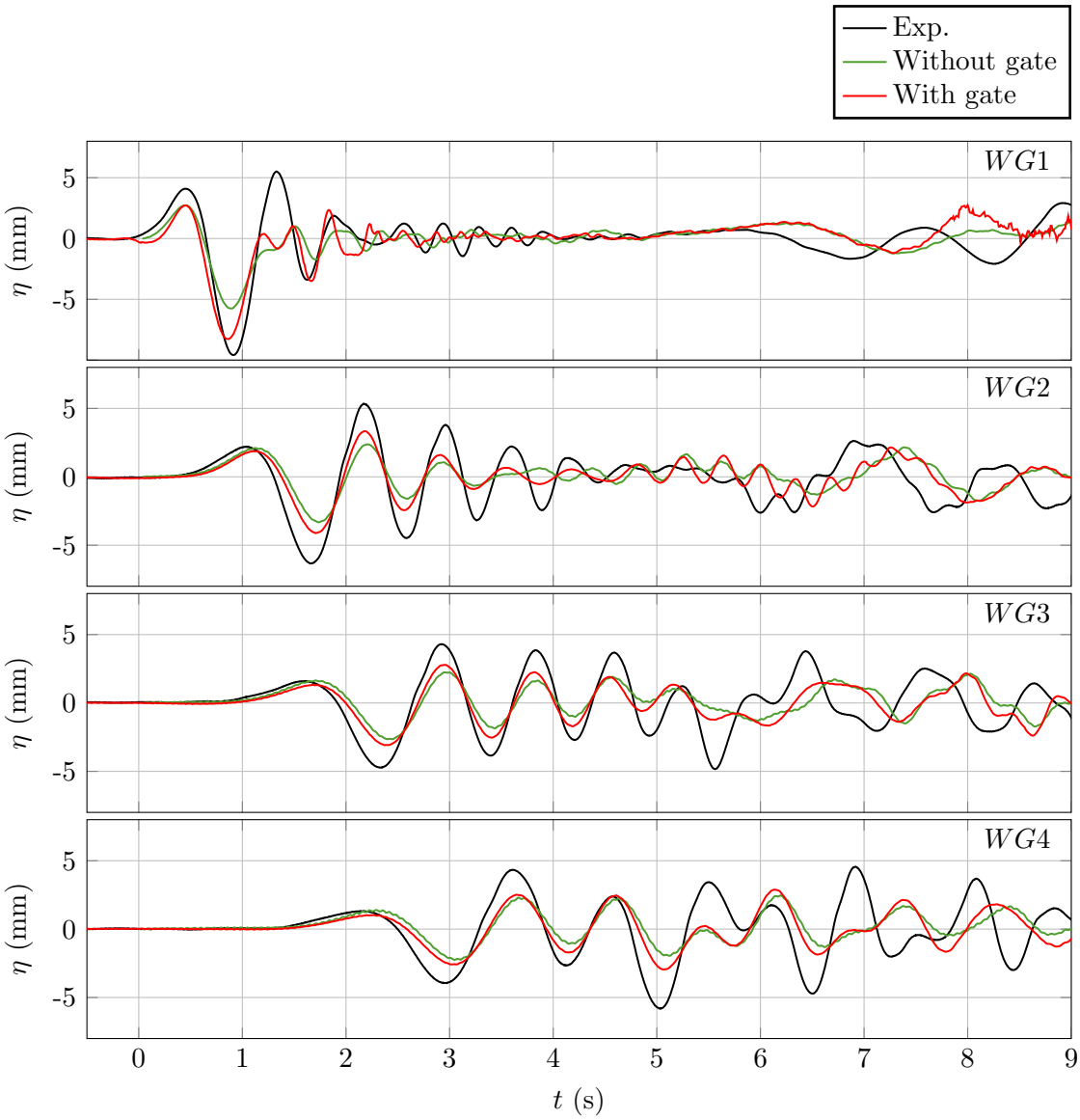

Figure 5.23: 2D Soil Collapse – Investigation of the gate withdrawing effect on the surface elevation at wave gauges $WG1$ to $WG4$. The black line represents experimental data, the red and green lines correspond to simulation results, respectively with and without the gate withdrawing modelling. In both cases, the granular-wall friction is modelled through elastic-viscoplastic boundary condition (see Section 4.6.3.2 for more details). The time origin corresponds to the moment the gate has withdrawn in the simulation. The first peak on $WG1$ is used to synchronized experimental and numerical data.

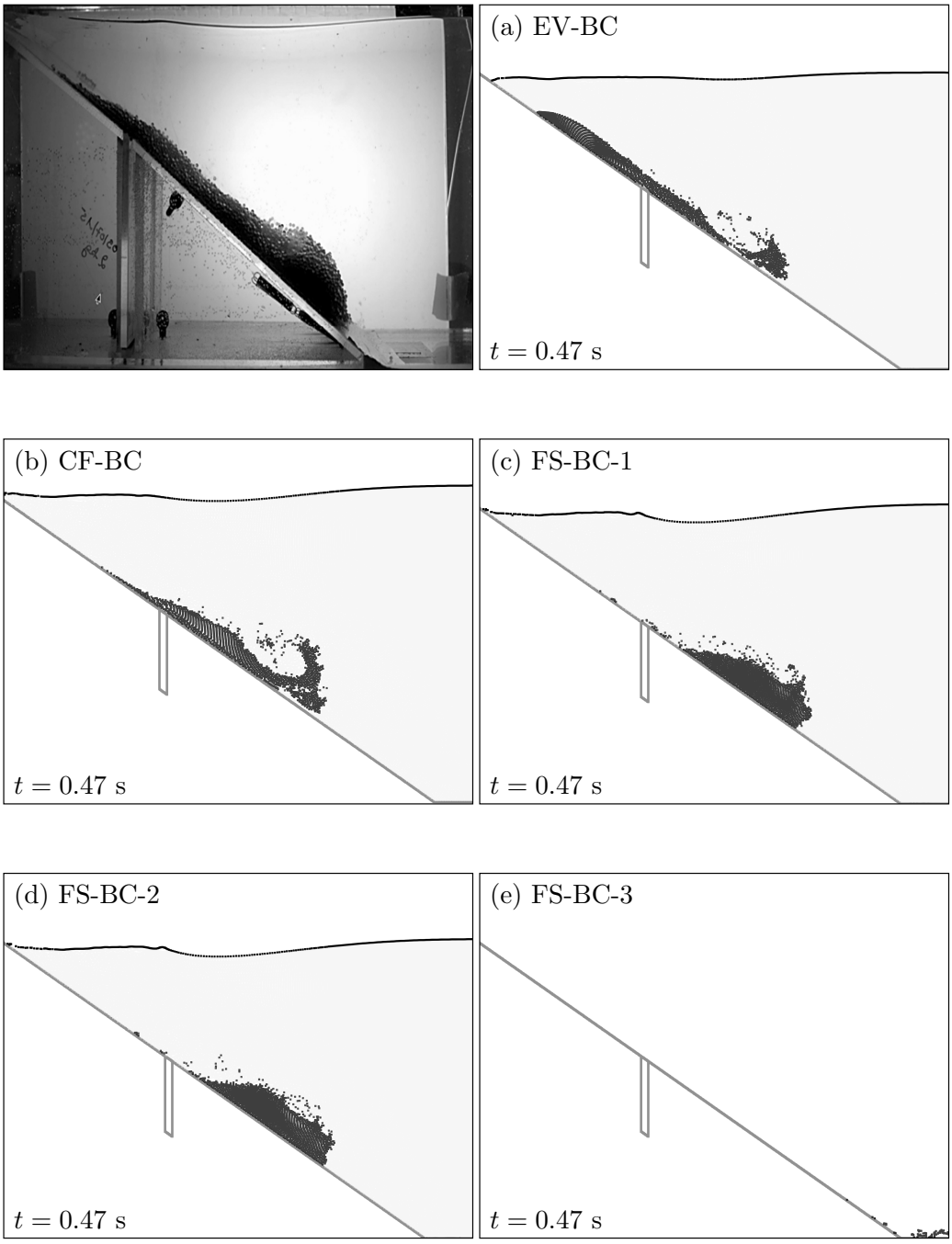

Figure 5.24: 2D Soil Collapse – Investigation of the wall and water effect on the falling time. Comparison of experimental (top left) and numerical (other panels) slide cross section at $t = 0.47$ s. The following numerical configurations are tested: elastic-viscoplastic boundary condition (EV-BC, top right), Coulomb's friction boundary condition (CF-BC, middle left), free-slip boundary condition (FS-BC-1, middle right), free-slip boundary condition without slide-water viscous friction (FS-BC-2, bottom left) and free-slip boundary condition without water (FS-BC-3, bottom right). The time origin corresponds to the moment the gate has withdrawn.

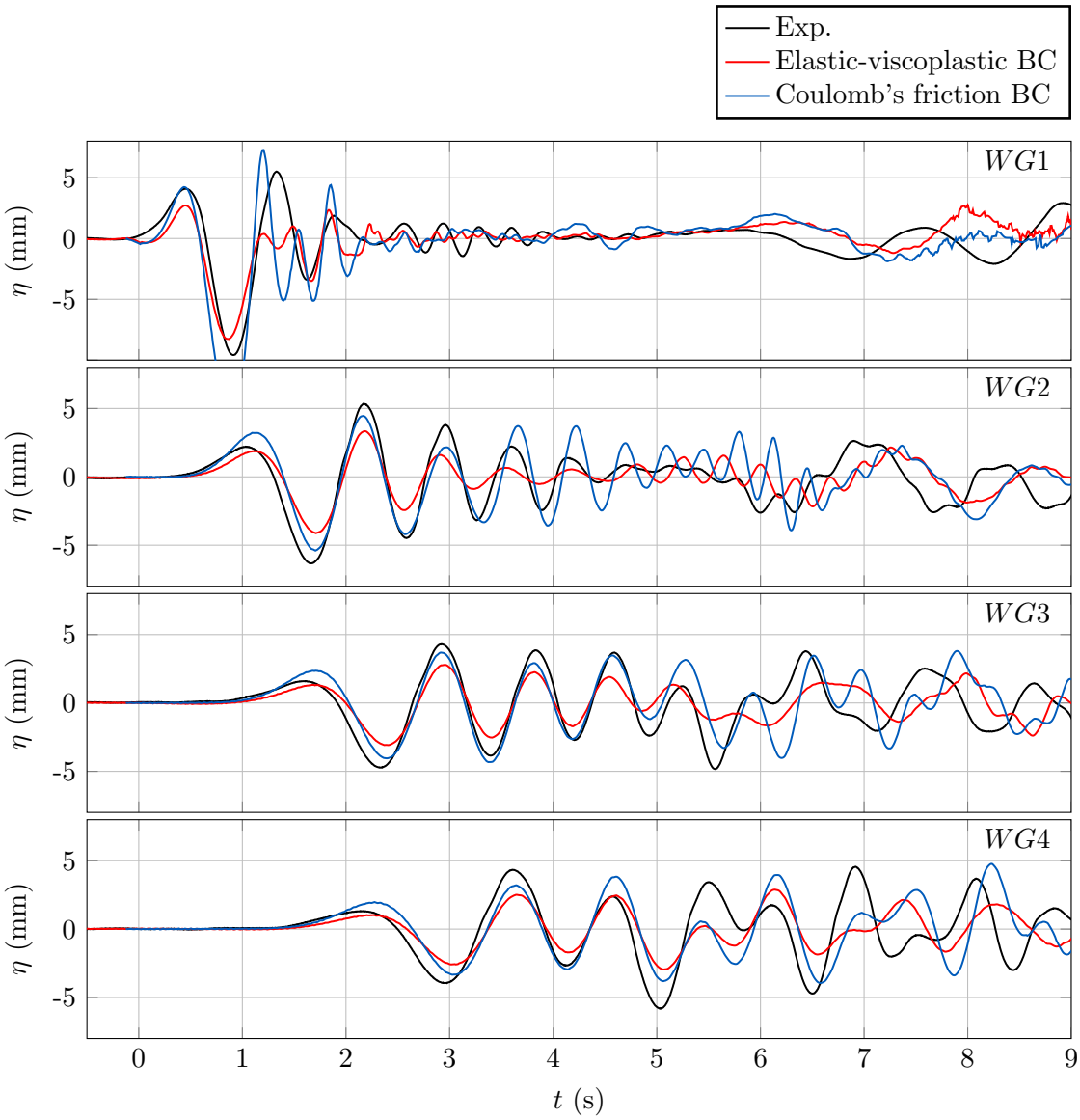

Figure 5.25: 2D Soil Collapse – Investigation of the wall-granular boundary condition effect on the surface elevation at wave gauges $WG1$ to $WG4$. The black line represents experimental data, the red line corresponds to the elastic-viscoplastic wall boundary condition simulation, and the blue line corresponds to the Coulomb's friction wall boundary condition simulation with $\mu = 0.5$. In both cases, the gate withdrawing is modelled. The time origin corresponds to the moment the gate has withdrawn in the simulation. The first peak on $WG1$ is used to synchronized experimental and numerical data.

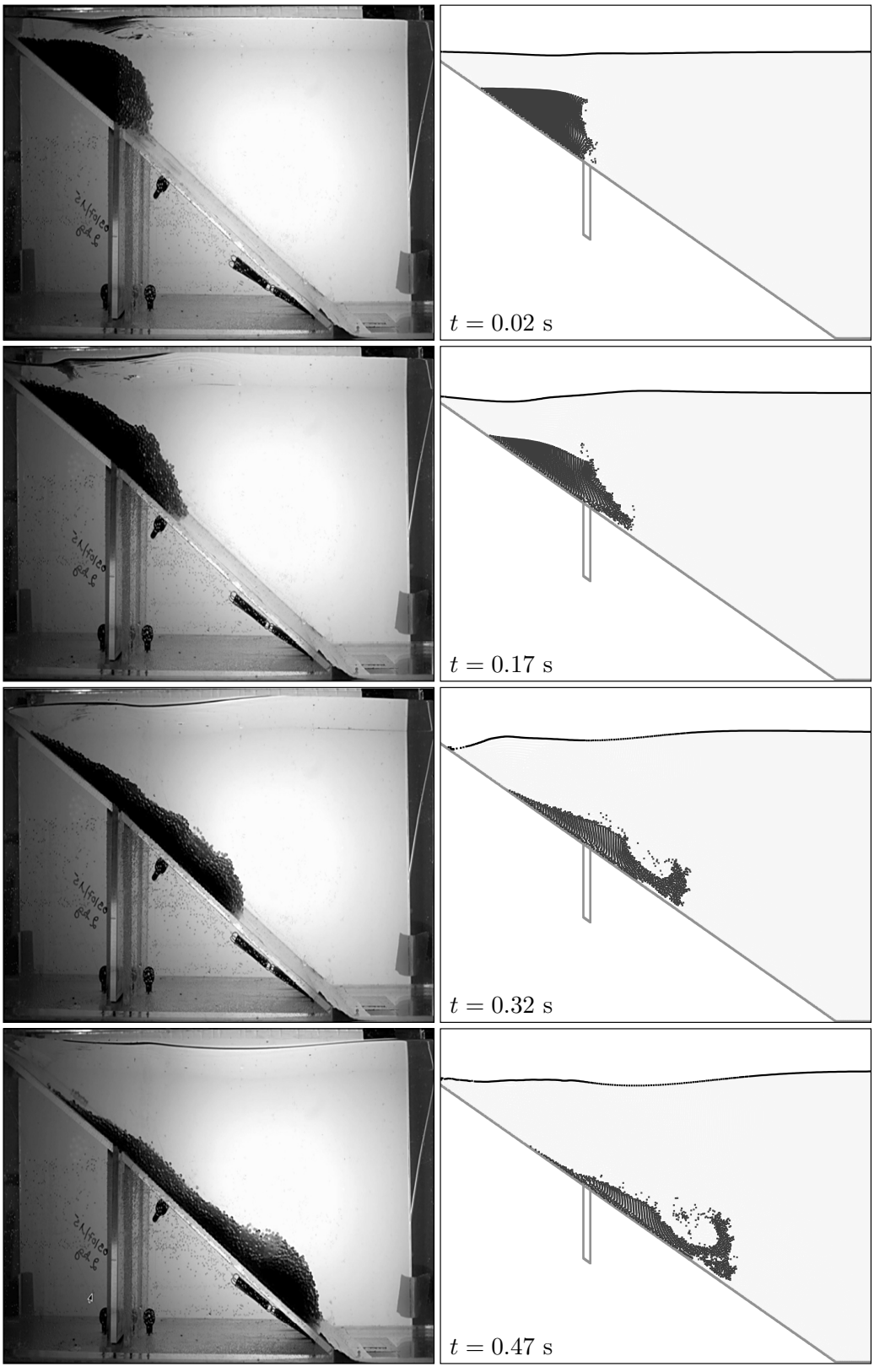

Figure 5.26: 2D Soil Collapse – Comparison of experimental (left) and numerical (right) slide cross section at times $t = 0.02$ s, $t = 0.17$ s, 0.32 s and 0.47 s. The time origin corresponds to the moment the gate has withdrawn. Coulomb's friction wall boundary condition is used.

fine sand ($d_g = 0.2$ mm). The generated solitary wave is defined by the following surface elevation profile:

$$\Delta h(x,t) = H_0 \operatorname{sech}^2 \left[k \left(x - ct - x_0 \right) \right] \tag{5.22}$$

where $\Delta h(x,t) = h(x,t) - h_0$ is the free-surface elevation, with $h(x,t)$ the water height at position x and h_0 the initial water height, H_0 is the wave amplitude, x_0 is the initial position of the wave peak, k and c are the wave number and the wave celerity defined by:

$$k = \sqrt{\frac{3H_0}{4h_0^3}}, \quad c = \sqrt{g\left(h_0 + H_0\right)} \tag{5.23}$$

A hydrostatic profile is used to initialize pressure, while the free-surface elevation and the velocity field are initialized using:

$$\begin{cases} h(x, t=0) & = h_0 + \Delta h(x,0) \\ u_x(x,y,t=0) & = c \dfrac{\Delta h(x,0)}{h(x,0)} \\ u_y(x,y,t=0) & = \dfrac{y}{h(x,0)} \dfrac{\partial \Delta h}{\partial t}(x,0) \end{cases} \tag{5.24}$$

Note that this solitary wave is a solution to the Korteweg-de Vries equation [28], but not to the Navier-Stokes equations. Thus, the wave is expected to deform while propagating both in the experiment in the SPH simulation. Many configurations were tested in Nakamura et al.'s [88] paper, but only one is studied here: $h_0 = 0.315$ m and $H_0 = 0.1231$ m.

The physical parameters of the materials are summarized in Table 5.8. In that case, the physical elastic properties of the granular material were available [88]. However, the internal friction was not given, so we set it at $\psi = 30^o$ which is the usual value taken for the sand. The tank is not entirely modelled in the simulation in order to reduce the computational cost. Only 2.5 m of flat bed is represented and the wave peak is initially equidistant from the downstream wall and the upstream slope, *i.e.* $x_0 = -3.21$ m.

The simulation was carried out setting a particle spacing of $\delta r \approx 0.009$ m, resulting in $1.3 \cdot 10^6$ particles of water, $140,000$ particles of saturated soil and $370,000$ particles vertex and boundary particles. The numerical speed of sound and isentropic coefficient are set identically for the saturated granular material and the water, that is $c_0 = 20$ m·s^{-1} and $\xi = 7$. Rhie and Chow's [101] chequerboard correction (2.99) was applied with a coefficient of $\Lambda_{\mathrm{RC}} = 1.0$, and no background pressure was used.

Results are presented in terms of dimensionless time t^+, surface-elevation Δh^+, pore water

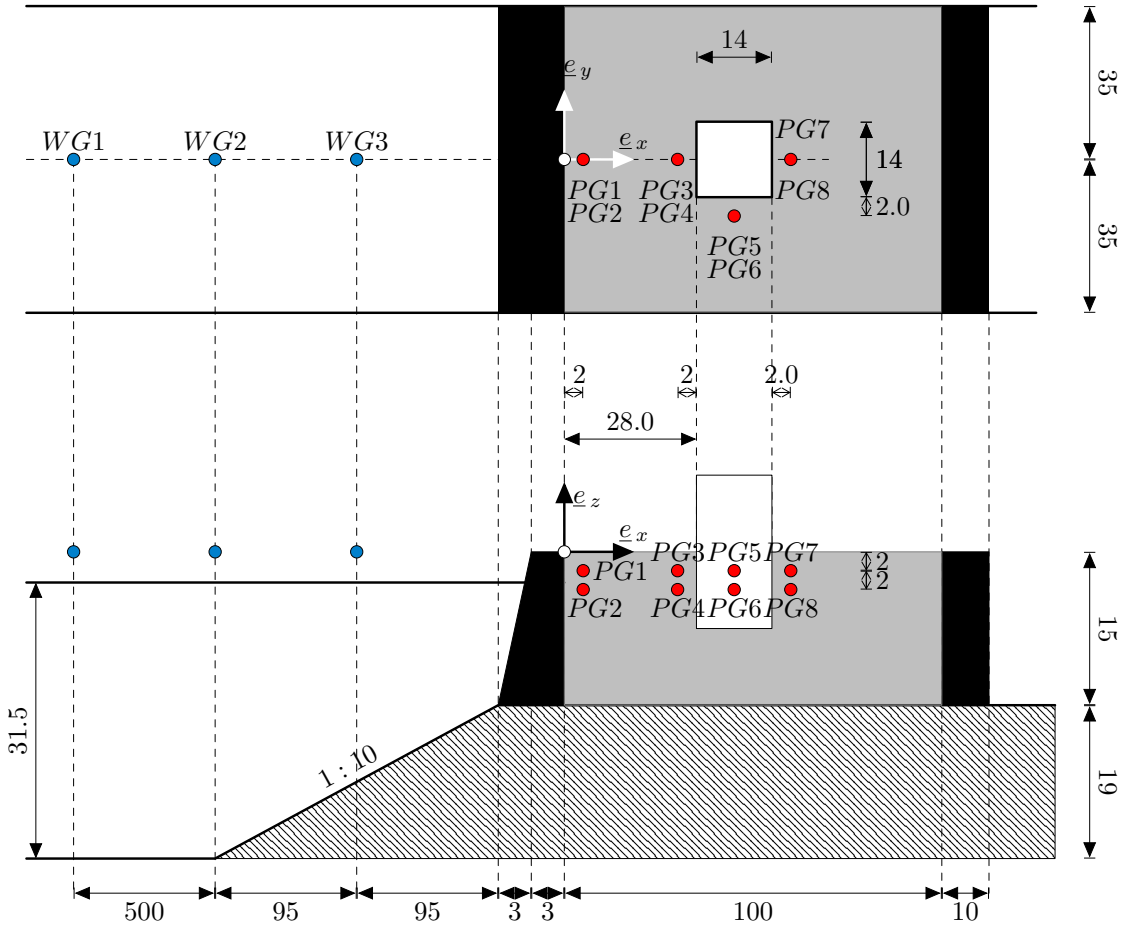

Figure 5.27: 3D Tsunami Scour – Experimental set-up of Nakamura et al.'s [88] experiments.

	ρ_g [kg/m^3]	d_g [mm]	ϕ [1]	E [Pa]	ν [1]	ψ [^{o}]
Sand	2650	0.2	0.4	$2.6 \cdot 10^8$	0.33	30

Table 5.8: Tsunami-induced scour – Physical parameters of the granular materials.

pressure excess $\Delta p_{\mathrm{pw}}^{+}$ and velocity u^{+}:

$$t^{+} = \frac{t}{\sqrt{h_0/g}}, \quad \Delta h^{+} = \frac{h - h_0}{h}, \quad \Delta p_{\mathrm{pw}}^{+} = \frac{p_{\mathrm{pw}} - p_{\mathrm{pw},0}}{\rho_{\mathrm{w}}\, g\, h_0}, \quad u^{+} = \frac{u}{c} \tag{5.25}$$

with $p_{\mathrm{pw},0}$ the initial pore water pressure, h_{s}, and $h_{\mathrm{s},0}$ the current and initial sand height in the reservoir. Figure 5.28 shows that the simulated wave is in good agreement with the experiment, though our model underestimates the reflected wave. In Figure 5.29, we can see a comparison of measured and simulated pore water excess at pressure gauges $PG1$ to $PG8$. The pore water pressure excess variations are due to the water pressure variations on the one hand, and on the lithostatic pressure variation (*i.e.* the sediment surface evolution) on the other hand. Thus this excess of pore water pressure is computed as:

$$p_{\mathrm{pw}} = p - p_{\mathrm{eff}} \tag{5.26}$$

where p_{eff} is obtained from (4.64) and p is the SPH pressure field calculated from the state equation (1.25). An overall satisfactory agreement is found. We can see some lack of data in the numerical results, in particular for gauges 1, 3, 4, 5 and 7. This occurs when no sediment SPH particles can be found at the pressure gauge location.

Figure 5.31 shows a 3D view of the wave impacting the structure at $t^{+} = 10$, while Figure 5.32 shows a cross section ($y^{+} = 0$) view at the same time. We can already see here that almost half of the initial sand height has been eroded. Figure 5.30 shows the sediment surface elevation at $t^{+} = 10.6$, *i.e.* the time when maximal scour depth in detected in the simulation. Results are plotted in terms of dimensionless coordinates (x^{+}, y^{+}) and sediment surface elevation $\Delta h_{\mathrm{s}}^{+}$ defined by:

$$x^{+} = \frac{x}{L_s}, \quad y^{+} = \frac{y}{L_s}, \quad \Delta h_{\mathrm{s}}^{+} = \frac{h_{\mathrm{s}} - h_{\mathrm{s},0}}{h_{\mathrm{s},0}} \tag{5.27}$$

The experimental maximal scour depth is about $\Delta h_{\mathrm{s}}^{+} \approx 0.25$ while we can see in Figure 5.30 that the simulation predicts $\Delta h_{\mathrm{s}}^{+} \approx 0.75$. However, it should be reminded that the particle size is large (≈ 9 mm) compared to the maximal scour depth (≈ 38 mm). Moreover, given that the physical grain size (0.2 mm), an SPH particle represents a volume that contains almost $50,000$ grains of sand. Therefore a more refined simulation would provide a chance to correctly predict the scouring process. Such a simulation was not carried because of the GPU memory limitation. A multi-GPU implementation of the present model would make this kind of simulation possible though.

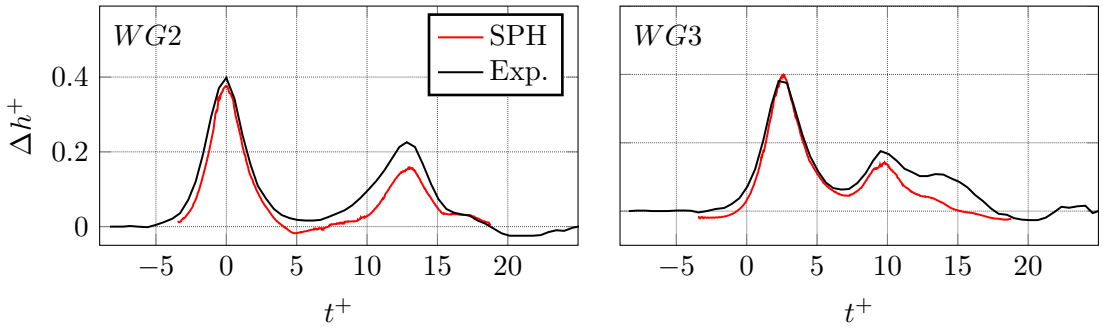

Figure 5.28: Tsunami-induced scour – Time evolution of the water height predicted by the present multi-phase SPH model (red) compared to Nakamura et al.'s [88] (black) experimental measurements.

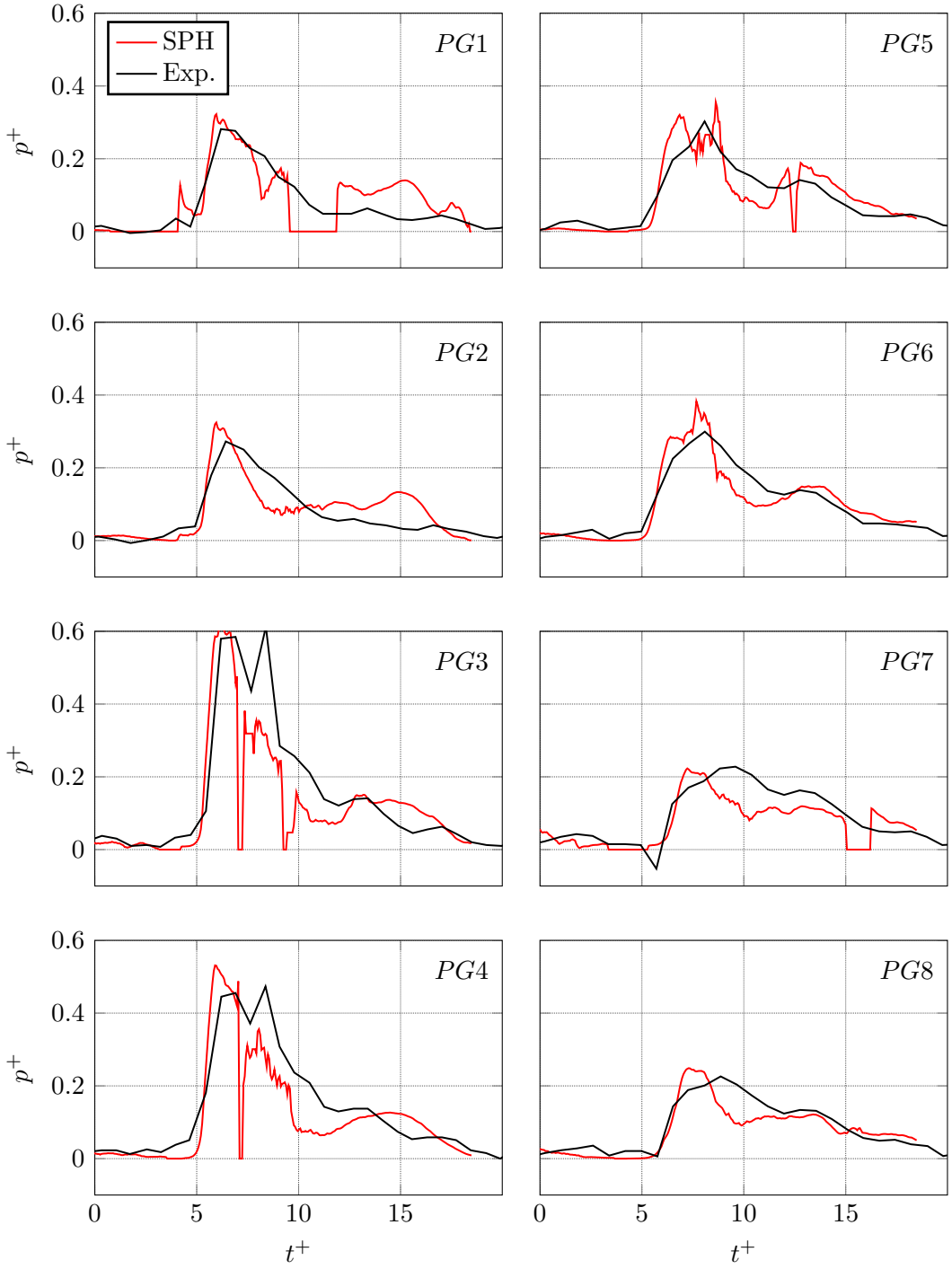

Figure 5.29: Tsunami-induced scour – Comparison of Nakamura et al.'s [88] experimental pressure measurements (black) with the present numerical results (red).

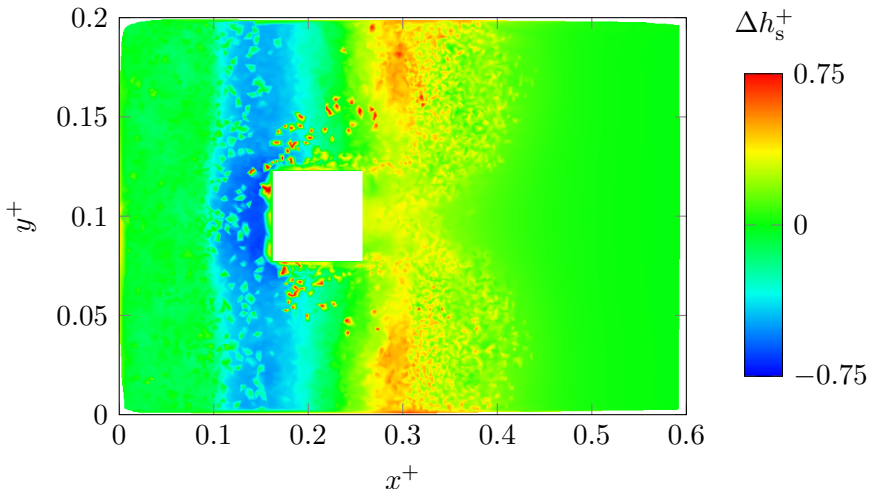

Figure 5.30: Tsunami-induced scour – Numerical results for the sediment surface elevation at $t^+ = 10.6$.

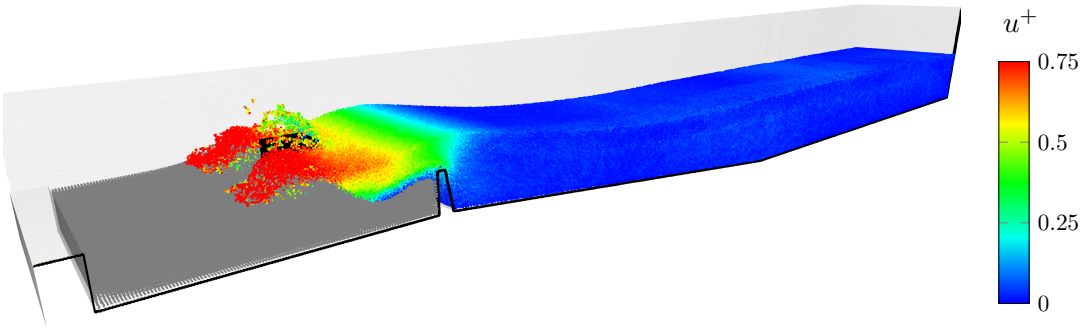

Figure 5.31: Tsunami-induced scour – 3D view at $t^+ = 10$. Water particles are coloured according to the dimensionless velocity field. Grey particles represents the saturated sand.

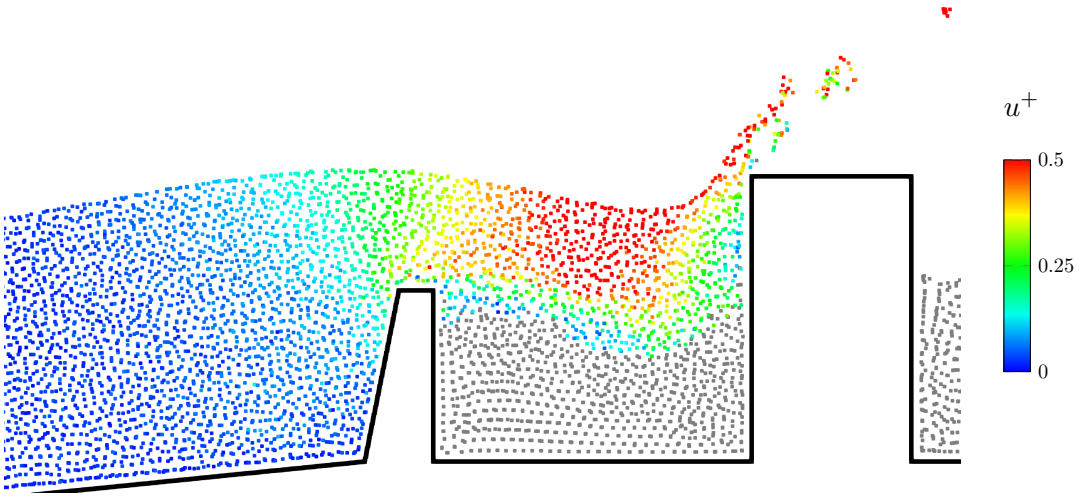

Figure 5.32: Tsunami-induced scour – Cross-section in the plane $y = 0$ at $t^+ = 10$. Water particles are coloured according to the dimensionless velocity field. Grey particles represents the saturated sand.

Conclusions and future work

Cette thèse porte sur le développement d'un modèle de transport sédimentaire par charriage pour la méthode SPH (Smoothed Particle Hydrodynamics). *Si les modèles couramment proposés dans la littérature reposent un solveur hydrodynamique couplé à des lois semi-empiriques pour la prise en compte du transport sédimentaire, une approche différente est proposée ici. Le modèle développé dans ce travail inclut la résolution de la dynamique du sédiment. Celui-ci est assimilé à un milieu continu dont la loi de comportement rend compte de la nature granulaire. Pour ce faire, le modèle élastique-viscoplastique d'Ulrich [114] a été implémenté dans un code SPH pré-existant programmé en langage Cuda, et amélioré du point de vue physico-numérique. Le comportement mécanique du sédiment dépend d'une contrainte de rupture déterminée conformément au critère de Drucker-Prager. Dans les zones du matériau où la rupture n'a pas eu lieu, les contraintes de cisaillement sont calculées selon la loi de Hooke généralisée. Dans les zones où la contrainte de rupture a été dépassée, le matériau est assimilé à un fluide rhéofluidifiant. Numériquement, la transition entre les deux états est opérée à l'aide d'une fonction de raccord qui dépend notamment du l'amplitude du taux de déformation et des propriétés granulaires du sédiment.*

Trois améliorations principales ont été apportées au modèle d'Ulrich [114]. Premièrement, une méthode fiable de calcul de la pression effective au sein du matériau a été développée pour la méthode SPH. Une technique de calcul numérique des forces élastiques fondée sur un opérateur SPH du deuxième ordre a également été proposée. Son utilisation semble conduire à une amélioration notable de la précision des forces calculées. Enfin, on propose un critère de transition entre les états liquide et solide, basé uniquement sur les propriétés physiques du matériau granulaire. Contrairement au modèle original d'Ulrich [114], le comportement mécanique du matériau ne dépend donc d'aucun paramètre numérique.

L'eau et le sédiment sont modélisées comme deux phases immiscibles, dans le cadre d'une formulation SPH multiphasique. Pour ce faire, le modèle de Hu et Adams [58] a été adapté au modèle de conditions limites semi-analytiques pour les parois [36]. Enfin, un schéma d'intégration implicite des forces visqueuses a été développé dans ce contexte, afin d'améliorer les performances du solveur lors de la modélisation d'écoulements à bas Reynolds.

Plusieurs cas-tests sont proposés pour valider le modèle multiphasique, le schéma implicite et le modèle élastique-viscoplastique. De manière générale, les résultats sont en bon accord avec les données expérimentales et analytiques. Le modèle permet de représenter des écoulements multiphasiques avec une bonne précision, même en présence d'un grand rapport de densité entre les phases. Il en va de même pour les écoulements de fluides non-newtoniens et les écoulements à bas Reynolds, pour lesquels le schéma implicite conduit à des résultats très satisfaisants, et à une amélioration significative des performances du code. Enfin, le modèle élastique-viscoplastique a été appliqué à divers cas d'écoulements granulaires, dans le cas d'un matériau sec et saturé, ainsi qu'à des cas d'érosion et d'affouillement. Là encore, les résultats sont globalement en bon accord avec l'expérience. Les limitations du modèle actuel sont toutefois clairement identifiées. Afin d'y remédier, plusieurs modifications de la formulation SPH utilisées semblent indispensables pour l'avenir. Les résultats relatifs au niveau d'érosion montrent que la possibilité d'utiliser des particules SPH de tailles variables présenterait un avantage considérable. Pour le transport sédimentaire comme pour beaucoup d'autres applications de la méthode SPH, ce verrou technique constitue un défi majeur pour la communauté SPH. D'autre part, certaines applications semblent requérir le développement d'un modèle de mélange, dans lequel les particules SPH contiendraient plusieurs phases à la fois, et échangeraient de la masse entre elles. Les situations dans lesquelles l'infiltration d'eau modifie les conditions de contraintes dans le matériau sont notamment concernées, mais le cas du glissement de terrain présenté dans ce travail témoigne aussi de la nécessité d'un tel modèle. Pour finir, ce modèle devrait être implémenté dans le logiciel GPUSPH dans le futur, en incluant le traitement des frontières ouvertes et le multi-parallélisme. Cela permettrait d'appliquer le modèle à des cas d'étude 3D avec une résolution suffisamment fine grâce au multi-GPU.

This thesis presents the development and application of a Smoothed Particle Hydrodynamics (SPH) model to bed-load transport. While state-of-the-art simulation methods commonly rely on a fluid dynamics solver coupled to semi-empirical relationships to model the sediment transport, a completely different approach was investigated in this work. The sediment is treated as a continuum whose constitutive equation takes account for its granular nature. Ulrich's [114] elastic-viscoplastic model was thus implemented in an in-house code based on the Cuda language, and improved on physical and numerical aspects. In this model, the sediment behaviour depends on a yield stress determined according to Drucker-Prager's criterion. In unyielded regions, the shear stresses are calculated in line with the linear elastic theory. In yielded regions, a shear thinning rheological law is used and the transitions between solid and liquid states are ensured by a blending function driven by the strain rate magnitude and sediment granular properties.

Three main improvements of Ulrich's model [114] were presented; namely a simple and reliable method to compute the effective pressure within the material, which is essential to correctly capture the failure process and the regime transitions, an improvement of solid forces calculation using a SPH second order derivative operator [33], and a physical threshold for the liquid-solid transition. Therefore, contrary to Ulrich's [114] original model, the mechanical behaviour of the soil does not depend on any numerical parameter in the present model.

The granular and water phases are treated in the frame of Hu and Adams's [58] SPH multi-phase formulation. The multi-phase model was adapted to semi-analytical wall boundary conditions [37] in order to model multi-phase flows that both require an accurate pressure and shear stress treatment at the wall, and present complex boundary geometries. An implicit viscous forces integration scheme was developed in this scope, improving the code performance when simulating low-Reynolds flow.

The multi-phase model, as well as the implicit viscous forces integration scheme, were validated on analytical test cases and good agreement was obtained. The multi-phase formulation has also proven its capability to handle flows involving high density ratio, while the implicit viscous forces integration scheme was successfully applied to the simulation of a non-Newtonian flow. The elastic-viscoplastic model was tested on dry and submerged granular flow problems. The model was able to correctly capture the liquid and solid states of the granular material, as well as the failure and the regime transitions. It was also applied to bed-load transport problems for which a good agreement with the experiment was generally found.

Some limits of the elastic-viscoplastic model were identified. First, the erosion seems to strongly depend on the SPH particle size and the grain size ratio. Although more investigations would be necessary, the model leads to important erosion overestimation when the SPH particle size is smaller than the grain size. In general, the model always

overestimates erosion so it provides a superior limit of the real erosion. In any case, this highlights the necessity of developing a variable spatial discretization SPH formulation, to be able to use different resolutions in the different phases.

Besides that, the main weakness of the model is probably its inability to handle variable grain concentration while it is a crucial parameter in the description of granular flows. Unfortunately, this was not treated in this work because it requires mass transfer between SPH particles, and therefore the development of a whole new SPH formulation. For the same reason, the present model does not account for the seepage flow. The lack of variable grain concentration and seepage flow modelling was particularly noticeable in the submarine landslide study: the mass of granular material behaves like an impermeable and incompressible deformable body, instead of an expensing volume of porous material. In that case, this implies an overestimation of the pressure drag, but more generally, the mechanical behaviour of the material is also strongly related to these phenomena [7, 78].

The seepage modelling would also be compulsory in many industrial applications, for example, the failure of a dyke resulting from the change of effective stress within the material requires to model the propagation of interstitial water. Ulrich [114] proposed a simplified model of partly saturated soil, solving the flow in the porous material and transporting a water concentration field. However, the mass of water is not conserved with his a model, and proper seepage modelling definitely requires a variable mass SPH formulation.

As regards erosion, the water-sediment interaction could be improved taking account for turbulence. In the present model, the shear stress at the water-sediment interface depends on the shear rate, the dynamic viscosity of water, and the local viscoplastic viscosity of the sediment. Physically, erosion results from the viscous and turbulent shear stresses exerted by water on the solid grains of sediment. Thus, it may be possible to use $k-\epsilon$ model in the water phase [65], treating the water-sediment interface as a solid wall. The stress exerted on the sediment SPH particles would then be deduced from the action-reaction principle. That way, the bottom shear stress would not depend on the rheological law used within the granular material.

Concerning the granular constitutive equation, the numerical solid-liquid transition technique could also be improved. When the material velocity tends to zero, it should reach a steady motionless state and behave like a pure elastic solid. In the present model, we thus expect the shear forces to be solely calculated from the elastic solid model, *i.e.* the blending function should be homogeneously equal to zero within the material. However, because of numerical noise, some strain rate may be artificially produced. Consequently, the sediment is in an unstable equilibrium, continuously oscillating between a solid state and a highly viscous liquid state. To circumvent this issue, the artificial stress method [48] could be implemented. This technique was developed to remove the tensile instability that

may be partly responsible for the above mentioned numerical noise; ISPH (Incompressible SPH, see *e.g.* [65]) is another alternative.

Finally, the validation on 3D cases should be pushed further. This will require to including the present model in a multi-GPU capable code. Therefore, the developments presented in this thesis are meant to be implemented in future versions of the open-source GPUSPH code [1], accounting for open boundary conditions and multi-parallelism.

Bibliography

[1] GPUSPH official website. www.gpusph.org. Accessed: 2017-03-31.

[2] PIXNOO official website. https://pixnio.com. Accessed: 2017-09-11.

[3] open telemac-mascaret officiel website. http://www.opentelemac.org. Accessed: 2017-09-11.

[4] U.s. geological survey official website. https://www.usgs.gov/media/images/scour-hole-around-bridge-pier. Accessed: 2017-09-11.

[5] AJ Abbo, AV Lyamin, SW Sloan, and JP Hambleton. A c2 continuous approximation to the mohr–coulomb yield surface. *International Journal of solids and Structures*, 48(21):3001–3010, 2011.

[6] M. Antuono, A. Colagrossi, S. Marrone, and D. Molteni. Free-surface flows solved by means of SPH schemes with numerical diffusive terms. *Computer Physics Communications*, 181(3):532–549, 2010.

[7] A. Armanini, H. Capart, L. Fraccarollo, and M. Larcher. Rheological stratification in experimental free-surface flows of granular–liquid mixtures. *Journal of Fluid Mechanics*, 532:269–319, 2005.

[8] N.J. Balmforth, I.A. Frigaard, and G. Ovarlez. Yielding to stress: recent developments in viscoplastic fluid mechanics. *Annual Review of Fluid Mechanics*, 46: 121–146, 2014.

[9] T. Belytschko, Y. Krongauz, J. Dolbow, and C. Gerlach. On the completeness of meshfree particle methods. *International Journal for Numerical Methods in Engineering*, 43(5):785–819, 1998.

[10] C.R. Beverly and R.I. Tanner. Numerical analysis of three-dimensional bingham plastic flow. *Journal of non-newtonian fluid mechanics*, 42(1):85–115, 1992.

[11] E.C. Bingham. *An investigation of the laws of plastic flow*, volume 13. Govt. Print. Off., 1917.

[12] A.W. Bishop and G. Eldin. Undrained triaxial tests on saturated sands and their significance in the general theory of shear strength. *Geotechnique*, 2(1):13–32, 1950.

[13] J. Bonet and T-S.L. Lok. Variational and momentum preservation aspects of smooth particle hydrodynamic formulations. *Computer Methods in applied mechanics and engineering*, 180(1):97–115, 1999.

[14] J. Bonet and M.X. Rodríguez-Paz. Hamiltonian formulation of the variable-h SPH equations. *Journal of Computational Physics*, 209(2):541–558, 2005.

[15] F. Brezzi and J. Pitkäranta. On the stabilization of finite element approximations of the stokes equations. In *Efficient solutions of elliptic systems*, pages 11–19. Springer, 1984.

[16] H.H. Bui, R. Fukagawa, K. Sako, and S. Ohno. Lagrangian meshfree particles method (SPH) for large deformation and failure flows of geomaterial using elastic–plastic soil constitutive model. *International Journal for Numerical and Analytical Methods in Geomechanics*, 32(12):1537–1570, 2008.

[17] C.S. Campbell. Rapid granular flows. *Annual Review of Fluid Mechanics*, 22(1): 57–90, 1990.

[18] J. Campbell, R. Vignjevic, and L. Libersky. A contact algorithm for smoothed particle hydrodynamics. *Computer methods in applied mechanics and engineering*, 184(1):49–65, 2000.

[19] T. Capone, A. Panizzo, and J.J. Monaghan. SPH modelling of water waves generated by submarine landslides. *Journal of Hydraulic Research*, 48(S1):80–84, 2010.

[20] J. Chauchat and M. Médale. A three-dimensional numerical model for incompressible two-phase flow of a granular bed submitted to a laminar shearing flow. *Computer Methods in Applied Mechanics and Engineering*, 199(9):439–449, 2010.

[21] L. Chiron. Couplage et améliorations de la méthode SPH pour traiter des écoulements à multi-échelles temporelles et spatiales, 2017.

[22] A. Colagrossi and M. Landrini. Numerical simulation of interfacial flows by smoothed particle hydrodynamics. *Journal of Computational Physics*, 191(2):448–475, 2003.

[23] A.N. Colagrossi, D. Durante, J.B. Avalos, and A. Souto-Iglesias. Discussion of stokes' hypothesis through the smoothed particle hydrodynamics model. *Physical Review E*, 96(2):023101, 2017.

[24] C.A. Couloumb. Essai sur une application des régles de maximis et minimis á quelques problémes de statique relatifs à 1âĂŹarchitecture. *Mémoires de la Mathématique et de physique, présentés à*, 1, 1776.

[25] P.A. Cundall. Computer simulations of dense sphere assemblies. *Micromechanics of granular materials*, 1988.

[26] R.A. Dalrymple and O. Knio. SPH modelling of water waves. In *Coastal Dynamics' 01*, pages 779–787, 2001.

[27] M. De Leffe, D. Le Touzé, and B. Alessandrini. Normal flux method at the boundary for SPH. In *4th Int. SPHERIC Workshop (SPHERIC 2009)*, 2009.

[28] R.G. Dean and R.A. Dalrymple. *Water wave mechanics for engineers and scientists*, volume 2. world scientific publishing Co Inc, 1991.

[29] W. Dehnen and H. Aly. Improving convergence in smoothed particle hydrodynamics simulations without pairing instability. *Monthly Notices of the Royal Astronomical Society*, 425(2):1068–1082, 2012.

[30] J.K. Dienes. On the analysis of rotation and stress rate in deforming bodies. *Acta mechanica*, 32(4):217–232, 1979.

[31] R.F. Dressler. Comparison of theories and experiments for the hydraulic dam-break wave. *Int. Assoc. Sci. Hydrology*, 3(38):319–328, 1954.

[32] S. Dutta, D. Wang, P. Tassi, and M.H. Garcia. Three-dimensional numerical modeling of the bulle-effect: the non-linear distribution of near-bed sediment at fluvial diversions. *Earth Surface Processes and Landforms*, 2017.

[33] P. Espanol and M. Revenga. Smoothed dissipative particle dynamics. *Physical Review E*, 67(2):026705, 2003.

[34] R. Fatehi and M.T. Manzari. A remedy for numerical oscillations in weakly compressible smoothed particle hydrodynamics. *International Journal for Numerical Methods in Fluids*, 67(9):1100–1114, 2011.

[35] J. Feldman and J. Bonet. Dynamic refinement and boundary contact forces in SPH with applications in fluid flow problems. *International Journal for Numerical Methods in Engineering*, 72(3):295–324, 2007.

[36] M. Ferrand, D.L. Laurence, B.D. Rogers, and D. Violeau. Improved time scheme integration approach for dealing with semi-analytical wall boundary conditions in SPARTACUS2D. In *Proc. 5th International SPHERIC Workshop*, pages 98–105, 2010.

[37] M. Ferrand, D.R. Laurence, B.D. Rogers, D. Violeau, and C. Kassiotis. Unified semi-analytical wall boundary conditions for inviscid, laminar or turbulent flows in the meshless SPH method. *International Journal for Numerical Methods in Fluids*, 71(4):446–472, 2013.

[38] M. Ferrand, A. Joly, C. Kassiotis, D. Violeau, A. Leroy, F.-X. Morel, and B.D. Rogers. Unsteady open boundaries for SPH using semi-analytical conditions and riemann solver in 2d. *Computer Physics Communications*, 210:29–44, 2017.

[39] A. Ferrari, M. Dumbser, E.F. Toro, and A. Armanini. A new 3d parallel SPH scheme for free surface flows. *Computers & Fluids*, 38(6):1203–1217, 2009.

[40] G. Fourtakas and B.D. Rogers. Modelling multi-phase liquid-sediment scour and resuspension induced by rapid flows using smoothed particle hydrodynamics (SPH) accelerated with a graphics processing unit (gpu). *Advances in Water Resources*, 92: 186–199, 2016.

[41] G. Fourtakas, B.D. Rogers, and D. Laurence. 3-D SPH modelling of sediment scouring induced by rapid flows. In *Proc. 9th International SPHERIC Workshop, Paris, France*, pages 9–16, 2014.

[42] A. Ghaitanellis, D. Violeau, A. Leroy, A. Joly, and M. Ferrand. Application of the unified semi-analytical wall boundary conditions to multi-phase SPH. In *Proc. 10th international SPHERIC workshop*, pages 333–340, 2015.

[43] R.A. Gingold and J.J. Monaghan. Smoothed particle hydrodynamics: theory and application to non-spherical stars. *Monthly notices of the royal astronomical society*, 181(3):375–389, 1977.

[44] I. Goldhirsch. Scales and kinetics of granular flows. *Chaos: An Interdisciplinary Journal of Nonlinear Science*, 9(3):659–672, 1999.

[45] I. Goldhirsch. Rapid granular flows. *Annual review of fluid mechanics*, 35(1):267–293, 2003.

[46] I. Goldhirsch and G. Zanetti. Clustering instability in dissipative gases. *Physical review letters*, 70(11):1619, 1993.

[47] L.M. Gonzalez, J.M. Sanchez, F. Macia, and A. Souto-Iglesias. Analysis of WCSPH laminar viscosity models. In *4th international SPHERIC workshop, Nantes, France*, 2009.

[48] J.P. Gray, J.J. Monaghan, and R.P. Swift. SPH elastic dynamics. *Computer methods in applied mechanics and engineering*, 190(49):6641–6662, 2001.

[49] N. Grenier, M. Antuono, A. Colagrossi, D. Le Touzé, and B. Alessandrini. An hamiltonian interface SPH formulation for multi-fluid and free surface flows. *Journal of Computational Physics*, 228(22):8380–8393, 2009.

[50] S.T. Grilli, M. Shelby, O. Kimmoun, G. Dupont, D. Nicolsky, G. Ma, J.T. Kirby, and F. Shi. Modeling coastal tsunami hazard from submarine mass failures: effect of slide rheology, experimental validation, and case studies off the us east coast. *Natural hazards*, 86(1):353–391, 2017.

[51] C.-Y. Guan, J.-F. Qi, N.-S. Qiu, G.-C. Zhao, Q. Yang, X.-D. Bai, and C. Wang. Macroscopic youngâĂŹs elastic modulus model of particle packing rock layers. *Open Journal of Geology*, 2(3):198–202, 2012.

[52] M.E. Gurtin. An introduction to continuum mechanics, volume 158 of mathematics in science and engineering, 1981.

[53] C.B. Harbitz, F. Løvholt, G. Pedersen, and D.G. Masson. Mechanisms of tsunami generation by submarine landslides: a short review. *Norwegian Journal of Geology/Norsk Geologisk Forening*, 86(3), 2006.

[54] M.R. Hashemi, M.T. Manzari, and R. Fatehi. Evaluation of a pressure splitting formulation for weakly compressible SPH: Fluid flow around periodic array of cylinders. *Computers & Mathematics with Applications*, 71(3):758–778, 2016.

[55] K.B. Haugen, F. Løvholt, and C.B. Harbitz. Fundamental mechanisms for tsunami generation by submarine mass flows in idealised geometries. *Marine and Petroleum Geology*, 22(1):209–217, 2005.

[56] D.J. Henkel. The relationships between the strength, pore-water pressure, and volume-change characteristics of saturated clays. *Geotechnique*, 9(3):119–135, 1959.

[57] D.J. Henkel. The relationships between the effective stresses and water content in saturated clays. *Geotechnique*, 10(2):41–54, 1960.

[58] X.Y. Hu and N.A. Adams. A multi-phase SPH method for macroscopic and mesoscopic flows. *Journal of Computational Physics*, 213(2):844–861, 2006.

[59] Wolfram Research, Inc. Mathematica, Version 10.4. Champaign, IL, 2017.

[60] H.M. Jaeger, S.R. Nagel, and R.P. Behringer. Granular solids, liquids, and gases. *Reviews of modern physics*, 68(4):1259, 1996.

[61] H. Jiang and Y. Xie. A note on the Mohr–Coulomb and Drucker–Prager strength criteria. *Mechanics Research Communications*, 38(4):309–314, 2011.

[62] P. Jop, Y. Forterre, and O. Pouliquen. A constitutive law for dense granular flows. *Nature*, 441(7094):727–730, 2006.

[63] S. Kulasegaram, J. Bonet, R.W. Lewis, and M. Profit. A variational formulation based contact algorithm for rigid boundaries in two-dimensional SPH applications. *Computational Mechanics*, 33(4):316–325, 2004.

[64] M.N. Landers. Bridge scour data management. *USGS Staff–Published Research*, page 141, 1992.

[65] A. Leroy. *Un nouveau modèle SPH incompressible: vers l'application à des cas industriels*. PhD thesis, Paris Est, 2014.

[66] A. Leroy, D. Violeau, M. Ferrand, and C. Kassiotis. Unified semi-analytical wall boundary conditions applied to 2-d incompressible SPH. *Journal of Computational Physics*, 261:106–129, 2014.

[67] A. Leroy, D. Violeau, M. Ferrand, and A. Joly. Buoyancy modelling with incompressible SPH for laminar and turbulent flows. *International Journal for Numerical Methods in Fluids*, 78(8):455–474, 2015.

[68] L.D. Libersky and A.G. Petschek. Smooth particle hydrodynamics with strength of materials. *Advances in the free-Lagrange method including contributions on adaptive gridding and the smooth particle hydrodynamics method*, pages 248–257, 1991.

[69] L.D. Libersky, A.G. Petschek, T.C. Carney, J.R. Hipp, and F.A. Allahdadi. High strain lagrangian hydrodynamics: a three-dimensional SPH code for dynamic material response. *Journal of computational physics*, 109(1):67–75, 1993.

[70] QQ Liu and JC Li. Effects of water seepage on the stability of soil-slopes. *Procedia IUTAM*, 17:29–39, 2015.

[71] H.-Y. Lo and P. L.-F. Liu. On the analytical solutions for water waves generated by a prescribed landslide. *Journal of Fluid Mechanics*, 821:85–116, 2017.

[72] L. Lobovskỳ, E. Botia-Vera, F. Castellana, J. Mas-Soler, and A. Souto-Iglesias. Experimental investigation of dynamic pressure loads during dam break. *Journal of Fluids and Structures*, 48:407–434, 2014.

[73] L.B. Lucy. A numerical approach to the testing of the fission hypothesis. *The astronomical journal*, 82:1013–1024, 1977.

[74] S. Manenti, S. Sibilla, M. Gallati, G. Agate, and R. Guandalini. SPH simulation of sediment flushing induced by a rapid water flow. *Journal of Hydraulic Engineering*, 138(3):272–284, 2011.

[75] S. Marrone, M. Antuono, A. Colagrossi, G. Colicchio, D. Le Touzé, and G. Graziani. δ-SPH model for simulating violent impact flows. *Computer Methods in Applied Mechanics and Engineering*, 200(13):1526–1542, 2011.

[76] A. Mayrhofer, M. Ferrand, C. Kassiotis, D. Violeau, and F.-X. Morel. Unified semi-analytical wall boundary conditions in SPH: analytical extension to 3-d. *Numerical Algorithms*, 68(1):15–34, 2015.

[77] A. Mendoza, J.D. Abad, E.J. Langendoen, D. Wang, P. Tassi, and K. Abderrezzak El Kadi. Effect of sediment transport boundary conditions on the numerical modeling of bed morphodynamics. *Journal of Hydraulic Engineering*, 143(4):04016099, 2016.

[78] GDR MiDi. On dense granular flows. *European Physical Journal E–Soft Matter*, 14 (4), 2004.

[79] E. Mitsoulis. Flows of viscoplastic materials: models and computations. *Rheology reviews*, 2007:135–178, 2007.

[80] A. Mokos, B.D. Rogers, and P.K. Stansby. A multi-phase particle shifting algorithm for SPH simulations of violent hydrodynamics with a large number of particles. *Journal of Hydraulic Research*, 55(2):143–162, 2017.

[81] J.J. Monaghan. Smoothed particle hydrodynamics. *Annual review of astronomy and astrophysics*, 30(1):543–574, 1992.

[82] J.J. Monaghan. Simulating free surface flows with SPH. *Journal of computational physics*, 110(2):399–406, 1994.

[83] J.J. Monaghan. Smoothed particle hydrodynamics. *Reports on progress in physics*, 68(8):1703, 2005.

[84] J.J. Monaghan and R.A. Gingold. Shock simulation by the particle method SPH. *Journal of computational physics*, 52(2):374–389, 1983.

[85] D. Morichon, J. Desombre, and B. Simian. VOF simulation of sediment transport under high velocity flow case of a dam break over a mobile bed. *Coastal Dynamics 2013*, pages 1241–1250, 2013.

[86] J.P. Morris, P.J. Fox, and Y. Zhu. Modeling low reynolds number incompressible flows using SPH. *Journal of computational physics*, 136(1):214–226, 1997.

[87] M.A. Nabian and L. Farhadi. Multiphase mesh-free particle method for simulating granular flows and sediment transport. *Journal of Hydraulic Engineering*, page 04016102, 2016.

[88] Tomoaki Nakamura, Yasuki Kuramitsu, and Norimi Mizutani. Tsunami scour around a square structure. *Coastal engineering journal*, 50(02):209–246, 2008.

[89] R.M. Nedderman. Statics and kinematics of granuular materials cambridge univ. *Press, Cambridge*, 1992.

[90] C.T. Nguyen, C.T. Nguyen, H.H. Bui, Giang D. Nguyen, and R. Fukagawa. A new SPH-based approach to simulation of granular flows using viscous damping and stress regularisation. *Landslides*, 14(1):69–81, 2017.

[91] M. Oda and K. Iwashita. Study on couple stress and shear band development in granular media based on numerical simulation analyses. *International journal of engineering science*, 38(15):1713–1740, 2000.

[92] E.J. O'Donovan and R.I. Tanner. Numerical study of the bingham squeeze film problem. *Journal of Non-Newtonian Fluid Mechanics*, 15(1):75–83, 1984.

[93] G. Oger, M. Doring, B. Alessandrini, and P. Ferrant. An improved SPH method: Towards higher order convergence. *Journal of Computational Physics*, 225(2):1472–1492, 2007.

[94] T.C. Papanastasiou. Flows of materials with yield. *Journal of Rheology (1978-present)*, 31(5):385–404, 1987.

[95] A. Peer, M. Ihmsen, J. Cornelis, and M. Teschner. An implicit viscosity formulation for SPH fluids. *ACM Transactions on Graphics (TOG)*, 34(4):114, 2015.

[96] M. Perić, R. Kessler, and G. Scheuerer. Comparison of finite-volume numerical methods with staggered and colocated grids. *Computers & Fluids*, 16(4):389–403, 1988.

[97] O. Pouliquen, C. Cassar, P. Jop, Y. Forterre, and M. Nicolas. Flow of dense granular material: towards simple constitutive laws. *Journal of Statistical Mechanics: Theory and Experiment*, 2006(07):P07020, 2006.

[98] N.J. Quinlan, M. Basa, and M. Lastiwka. Truncation error in mesh-free particle methods. *International Journal for Numerical Methods in Engineering*, 66(13):2064–2085, 2006.

[99] P.W. Randles and L.D. Libersky. Smoothed particle hydrodynamics: some recent improvements and applications. *Computer methods in applied mechanics and engineering*, 139(1-4):375–408, 1996.

[100] T. Revil-Baudard and J. Chauchat. A two-phase model for sheet flow regime based on dense granular flow rheology. *Journal of Geophysical Research: Oceans*, 118(2): 619–634, 2013.

[101] C.M. Rhie and W.L. Chow. Numerical study of the turbulent flow past an airfoil with trailing edge separation. *AIAA Journal*, 21(11):1525–1532, November 1983.

[102] A. Schofield and P. Wroth. *Critical state soil mechanics*, volume 310. McGraw-Hill London, 1968.

[103] D. Sherpard. A two dimensional function for irregualarly spaced data. In *ACM National Conference*, 1968.

[104] B. Spinewine and Y. Zech. Small-scale laboratory dam-break waves on movable beds. *Journal of Hydraulic Research*, 45(sup1):73–86, 2007.

[105] O.D.L. Strack and P.A. Cundall. *The distinct element method as a tool for research in granular media.* Department of Civil and Mineral Engineering, University of Minnesota, 1978.

[106] Q. Sun and G. Wang. *Mechanics of Granular Matter.* Tsinghua University, 2013.

[107] K. Szewc. *Développement d'une approche particulaire de type SPH pour la modélisation des écoulements multiphasiques avec interfaces variables.* PhD thesis, Université de Lorraine, 2013.

[108] P.G. Tait. *Report on some of the physical properties of fresh water and of sea water.* Johnson Reprint Corporation, 1965.

[109] H. Takeda, S.M. Miyama, and M. Sekiya. Numerical simulation of viscous flow by smoothed particle hydrodynamics. *Progress of Theoretical Physics*, 92(5):939–960, 1994.

[110] R.I. Tanner and J.F. Milthorpe. Numerical simulation of the flow of fluids with yield stress. *Numer Meth Lami Turb Flow Seattle*, pages 680–690, 1983.

[111] K.V. Terzaghi. The shearing resistance of saturated soils and the angle between the planes of shear. In *Proceedings of the 1st international conference on soil mechanics and foundation engineering*, volume 1, pages 54–56. Harvard University Press Cambridge, MA, 1936.

[112] V.D. Than, S. Khamseh, A.M. Tang, J.-M. Pereira, F. Chevoir, and J.-N. Roux. Basic mechanical properties of wet granular materials: A dem study. *Journal of Engineering Mechanics*, 143(1):C4016001, 2016.

[113] C. Thornton. Numerical simulations of deviatoric shear deformation of granular media. *Géotechnique*, 50(1):43–53, 2000.

[114] C. Ulrich. *Smoothed-particle-hydrodynamics simulation of port hydrodynamic problems.* PhD thesis, Technische Universitat Hamburg Harburg, 2013.

[115] H.A. Van der Vorst. Bi-cgstab: A fast and smoothly converging variant of bi-cg for the solution of nonsymmetric linear systems. *SIAM Journal on scientific and Statistical Computing*, 13(2):631–644, 1992.

[116] V. Vidyapati and S. Subramaniam. Granular rheology and phase transition: Dem simulations and order-parameter based constitutive model. *Chemical engineering science*, 72:20–34, 2012.

[117] J.P. Vila. On particle weighted methods and smooth particle hydrodynamics. *Mathematical models and methods in applied sciences*, 9(02):161–209, 1999.

[118] D. Violeau. Dissipative forces for lagrangian models in computational fluid dynamics and application to smoothed-particle hydrodynamics. *Physical Review E*, 80(3): 036705, 2009.

[119] D. Violeau. *Fluid mechanics and the SPH method: theory and applications*. Oxford University Press, 2012.

[120] D. Violeau and A. Leroy. On the maximum time step in weakly compressible SPH. *Journal of Computational Physics*, 256:388–415, 2014.

[121] D. Violeau, A. Leroy, and A. Mayrhofer. Exact computation of SPH wall renormalising integrals in 3-d. In *Proceedings of the 9th International SPHERIC Workshop*, pages 95–102, 2014.

[122] D. Violeau, S. Lind, and W. Dehnen. Convergence rate of the SPH poisson equation on a cartesian grid. In *Proc. 12th international SPHERIC workshop*, pages 54–58, 2017.

[123] D. Wang, P. Tassi, K. El Kadi Abderrezzak, AL Mendoza, J. Abad, and E. Langendoen. 2D and 3D numerical simulations of morphodynamics structures in large-amplitude meanders. In *Meeting Proceedings*, pages 3–5, 2014.

[124] H. Wendland. Piecewise polynomial, positive definite and compactly supported radial functions of minimal degree. *Advances in computational Mathematics*, 4(1): 389–396, 1995.

[125] D.M. Wood. *Geotechnical modelling*, volume 1. CRC Press, 2003.

[126] A.M. Xenakis, S.J. Lind, P.K. Stansby, and B.D. Rogers. An ISPH scheme with shifting for newtonian and non-newtonian multi-phase flows. In *Proc. 10th international SPHERIC workshop*, pages 84–91, 2015.

[127] V. Zago, A. Hérault, L. Fortuna, and R.A. Darymple. Implicit integration of the viscous term and gpu implementation in gpusph for lava flows. In *Proc. 12th international SPHERIC workshop*, pages 276–282, 2017.